

# **Modeling of Shock Wave Propagation and Attenuation in Viscoelastic Structures**

Razvan Rusovici

Dissertation submitted to the Faculty of the  
Virginia Polytechnic Institute and State University  
in partial fulfillment of the requirements for the degree of

Doctor of Philosophy  
in  
Mechanical Engineering

Dr. D.J. Inman and Dr. G.A. Lesieutre, Chairs

Dr. M. Ahmadian

Dr. H.H. Cudney

Dr. H.H. Robertshaw

Dr. W.R. Saunders

September 3rd, 1999

Blacksburg, VA

Keywords: Damping, Anelastic Displacement Fields, Finite Element, Shock, Mechanical  
Filter, Wave Propagation

Copyright 1999, Razvan Rusovici

# **Modeling of Shock Wave Propagation and Attenuation in Viscoelastic Structures**

**Razvan Rusovici**

## **(ABSTRACT)**

Protection from the potentially damaging effects of shock loading is a common design requirement for diverse mechanical structures ranging from shock accelerometers to spacecraft. High-damping viscoelastic materials are employed in the design of geometrically complex impact absorbent components. Since shock transients have a broadband frequency spectrum, it is imperative to properly model frequency dependence of material parameters. The Anelastic Displacement Fields (ADF) method is employed to develop new axisymmetric and plane stress finite elements that are capable of modeling frequency dependent material behavior of linear viscoelastic materials. The new finite elements are used to model and analyze behavior of viscoelastic structures subjected to shock loads. The development of such ADF-based finite element models offers an attractive analytical tool to aid in the design of shock absorbent mechanical filters. This work will also show that it is possible to determine material properties' frequency dependence by iteratively fitting ADF model predictions to experimental results.

A series of experiments designed to validate the axisymmetric and plane stress finite element models are performed. These experiments involve the propagation of longitudinal waves through elastic and viscoelastic rods, and behavior of elastomeric mechanical filters subjected to shock. Comparison of model predictions to theory and experiments confirm that ADF-based finite element models are capable of capturing phenomena such as geometric dispersion and viscoelastic attenuation of longitudinal waves in rods as well as modeling the behavior of mechanical filters subjected to shock.

## ACKNOWLEDGEMENTS

This thesis would not have been possible without the continuous support of my advisors: Dr. Daniel J. Inman and Dr. George A. Lesieutre. Dr. Inman took time from his extremely demanding schedule to visit, advise and encourage me at my new job location, in Buffalo, NY. His outstanding knowledge and kindness were always reliable resources in times of need. Dr. Lesieutre was always there when I needed his brilliant technical expertise and teaching abilities, from my Master to my Doctoral degree. He was always willing to sacrifice time to accommodate me. I was very fortunate and honored to have such prestigious scientists as advisors.

Dr. Eric Austin devoted some of his valuable time to participate as a committee member during my defense, and to review both my presentation and thesis. Thanks are due to Dr. Harry Robertshaw, Dr. Mehdi Ahmadian and Dr. William Saunders for their advice and careful thesis corrections. My gratitude also goes to Dr. Harley Cudney, for his sound technical advice and support, and to Dr. Victor Giurgiutiu for his support while he was at Virginia Tech.

I was lucky to work at PCB Piezotronics Inc. under the supervision of Dr. Jeffrey Dosch, whose ideas provided some of the initial motivation for this research. I am indebted to Mr. David Lally, Vice-President of Engineering, who was always supportive of my graduate studies. Mr. Jing Lin and Mr. Hu Chen provided technical expertise, and Mr. Dave Nocera provided encouragement when I needed them. Thanks go to Mr. Bill Hynd for encouragement, and for his well-designed charge amplifier.

I am thankful to Dr. Axinte Ionita, for his friendship and his pertinent suggestions on finite elements. Mr. Chris Brackbill, Ph.D. Candidate, has kindly provided help with my thesis.

I would like to thank the astronauts, aviators and scientists, the men and women who were not content to only walk this Earth, who dreamed of flying to the stars.

My parents, Gigi and Florin, are now long departed but never forgotten. There are no words to thank them enough for what they suffered and done for me, for their love. They taught me the joy of laughter and they showed me the New World. I remember my father trying to motivate me before my university entrance exam, trying to make me feel like a soccer player competing for the World Cup. I can still feel my mother's gentle hands and her warm eyes, the way she showed me the sparkle of a sun-touched raindrop caught on a leaf. My dear grandparents, Theodor and Elena, fired my imagination with wonderful stories, and patiently witnessed my often-fruitless fishing trips. I hope that God took good care of their gentle souls.

My father and mother in law, Paul and Veronica Cupen, were my support the last few years, in hard times, when friends really count. I am proud to call them now Mother and Father.

Finally, I dedicate this work to my beautiful wife, Daniela Rusovici, M.D. Without her help and understanding, I would not have had the chance to pursue my graduate studies. She was the only one who trusted me completely, and the power of her smile helped me regain confidence in the future. My love and gratitude towards her are endless.

*Per aspera ad astra*

## TABLE OF CONTENTS

ABSTRACT .....	ii
ACKNOWLEDGEMENTS.....	iii
TABLE OF CONTENTS.....	v
LIST OF FIGURES .....	viii
LIST OF TABLES .....	xii
CHAPTER 1. INTRODUCTION .....	1
1.1. Introduction .....	1
1.2. Linear viscoelasticity.....	2
1.3. Linear material damping.....	5
1.4. Damping modeling in finite element analysis .....	6
1.5. Longitudinal wave propagation through bars.....	18
1.6. Hopkinson bar shock accelerometer calibration procedure .....	22
1.7. Viscoelastic mechanical filter designs for shock accelerometers .....	27
1.8. Objectives and Motivation of the Current Research .....	29
1.9. Outline .....	31
CHAPTER 2. MODEL DEVELOPMENT.....	32
2.1. Development of the plane stress triangular ADF finite element.....	32
2.1.1. Assumptions and stress-strain equations.....	32

2.1.1.1.	Plane stress approximation.....	33
2.1.1.2.	ADF constitutive equations.....	33
2.1.2.	Governing Equations.....	44
2.1.2.1.	Equations of motion .....	44
2.1.2.2.	Relaxation equations .....	45
2.1.3.	Model development.....	47
2.2.	Development of the axisymmetric triangular ADF finite element.....	54
2.2.1.	Assumptions and stress-strain equations.....	54
2.2.2.	Governing equations .....	55
2.2.3.	Model development.....	59
2.3.	Boundary conditions .....	66
2.4.	Multiple Anelastic Displacement Fields .....	66
2.5.	Determination of model input from material complex moduli data .....	69
CHAPTER 3. RESULTS AND DISCUSSION.....		71
3.1.	Numerical and computational considerations .....	72
3.2.	Longitudinal wave propagation through bars-comparison of finite element results to theory .....	73
3.2.1.	Longitudinal wave propagation through an elastic clamped-free bar .....	74
3.2.2.	Longitudinal wave propagation along a titanium alloy free-free bar.....	80
3.2.3.	Longitudinal wave propagation along a viscoelastic free-free bar .....	83
3.2.4.	Numerical study of longitudinal wave propagation along split Hopkinson bar.....	94
3.2.5.	Modeling of geometrical dispersion in a Perspex™ bar .....	102
3.2.6.	Modeling of longitudinal wave propagation through an elastic bar with mechanical filter and mass at end .....	105
3.3.	Comparison of finite element results to experimental results.....	114

3.3.1.	ADF modeling of mechanical filters subjected to shock and comparison to experiments .....	114
3.3.1.1.	Mechanical filter with 3.5-mm-thick Buna N 60 Durometer rubber layer.....	117
3.3.1.2.	Mechanical filter with 7-mm-thick Buna N 60 Durometer rubber layer	121
3.3.2.	Modeling of wave propagation through metal bars and comparison to experiments .....	125
3.3.3.	Modeling of wave propagation through viscoelastic bars and comparison to experiments .....	129
3.3.4.	Modeling of mechanical filters in shock conditions .....	134
CHAPTER 4. CONCLUSIONS AND FUTURE WORK.....		141
4.1.	Conclusions .....	141
4.2.	Future work .....	142
REFERENCES .....		145
VITA.....		150

## TABLE OF FIGURES

Figure 1.1a. Maxwell model	3
Figure 1.1b. Standard viscoelastic solid	3
Figure 1.2. ATF rod finite element	15
Figure 1.3. One-dimensional bar	16
Figure 1.4. ADF rod finite element	18
Figure 1.5. Time record of displacement at end and middle of free-free elastic bar	20
Figure 1.6. Hopkinson bar test setup	23
Figure 1.7. Front panel of Labview <sup>TM</sup> data acquisition code showing acquired signals, computed sensitivity, zero-shift and shock level	26
Figure 1.8. Sensitivity data for an accelerometer	27
Figure 2.1. Plane-stress finite element	33
Figure 2.2. Axisymmetric finite element	55
Figure 3.1. Ti6Al4V alloy loss and storage moduli data fit with 5 ADF	75
Figure 3.2. Ti6Al4V alloy loss and storage moduli data fit with one ADF	76
Figure 3.3. Finite element mesh for the clamped-free bar, ADF axisymmetric FE	77
Figure 3.4. Time history of ADF predicted longitudinal displacement vs. theory (one ADF)	78
Figure 3.5. Time history of ADF predicted longitudinal displacement vs. theory (five ADF)	78
Figure 3.6. Plane stress finite element mesh for the clamped-free bar	79
Figure 3.7. Time record of predicted longitudinal displacement vs. theory, plane stress element with five ADF	80
Figure 3.8. Impact force on end of bar	81
Figure 3.9. Longitudinal displacement's time history at the free end and in the middle of the bar	82
Figure 3.10. Longitudinal velocity's time history at the free end and at the middle	83
Figure 3.11. Propagation of particle velocity pulse along bar	83
Figure 3.12. Longitudinal wave particle velocity vs. time at three stations along PERSPEX <sup>TM</sup> bar, ADF plane stress element	85



Figure 3.13. Longitudinal wave displacement vs. time at three stations along PERSPEX™ bar, ADF plane stress element	86
Figure 3.14. Longitudinal wave displacement vs. time at three stations along PERSPEX™ bar, ADF axisymmetric FE	87
Figure 3.15. Longitudinal wave velocity vs. time at three stations along PERSPEX™ bar, ADF axisymmetric FE	88
Figure 3.16. Longitudinal wave velocity vs. time at three stations along PERSPEX™ bar, ADF axisymmetric FE	89
Figure 3.17. High frequency components dissipate from 1 <sup>st</sup> (incident) and 2 <sup>nd</sup> reflected stress pulse at free end	90
Figure 3.18. Time record of elastic longitudinal displacement along PERSPEX™ bar	91
Figure 3.19. Time record of longitudinal velocity along PERSPEX™ bar, elastic FEM	92
Figure 3.20. Time record of mechanical energy predicted by the axisymmetric ADF and elastic FEM, respectively	93
Figure 3.21. Axisymmetric grid	94
Figure 3.22. Force acting on free end of split Hopkinson bar	95
Figure 3.23. Particle velocity at various time instances	96
Figure 3.24. Particle velocity as the pulse hits the boundary (0.65 msec. after impact)	97
Figure 3.25. Particle velocity along bar at various instances	98
Figure 3.26. Longitudinal displacement along bar at various instances	99
Figure 3.27. Longitudinal displacement along bar at various instances	100
Figure 3.28. Longitudinal displacement time record at bar ends	101
Figure 3.29. Mechanical energy in Hopkinson bar vs. time	102
Figure 3.30. Dispersion: comparison to normalized end displacements at end of two PERSPEX™ bars	104
Figure 3.31. Mechanical energy in 15-cm diameter bar vs. time	105
Figure 3.32. Time record of displacement at bar's end and at mass	107
Figure 3.33. Particle velocity of end of bar and of mass	108
Figure 3.34. Velocity of mass: low loss and high loss filters	109
Figure 3.35. Displacement of mass: low loss and high loss filters	110
Figure 3.36. Velocity at bar end vs. time: low loss and high loss factor filters	111

Figure 3.37. Displacement at end of bar: low loss and high loss filters	112
Figure 3.38. Energy in system vs. time	113
Figure 3.39. Drop test	115
Figure 3.40. (a & b) ADF curve-fit of storage modulus and loss factor	116
Figure 3.41. Force input for filter with 3.5-mm rubber layer	118
Figure 3.42. Force power spectrum for filter with 3.5 mm rubber layer	118
Figure 3.43. Predicted vs. experimental displacement for filter with 3.5-mm rubber layer	119
Figure 3.44. Predicted velocity vs. experiment, for filter with 3.5-mm thick rubber layer	119
Figure 3.45. Predicted vs. experimental acceleration for filter with 3.5-mm rubber layer	120
Figure 3.46. Experimental vs. predicted acceleration power spectrum	121
Figure 3.47. Force input for filter with 7-mm rubber layer	122
Figure 3.48. Input force power spectrum	122
Figure 3.49. Predicted vs. experimental displacement for filter with 7-mm rubber layer	123
Figure 3.50 Predicted vs. experimental velocity for filter with 7-mm rubber layer	123
Figure 3.51. Predicted vs. experimental acceleration for filter with 7-mm rubber layer	124
Figure 3.52. Experimental vs. predicted acceleration power spectrum, for filter with 7-mm rubber layer	124
Figure 3.53. Impact force of DELRIN <sup>TM</sup> bullet at end of bar	125
Figure 3.54. Predicted vs. experimental longitudinal displacement on the bar	126
Figure 3.55. Predicted vs. experimental longitudinal velocity on ba	127
Figure 3.56. Predicted vs. experimental longitudinal acceleration on bar	128
Figure 3.57. Predicted vs. experimental longitudinal velocity power spectrum on bar	128
Figure 3.58. Predicted vs. experimental strain time record at middle of PERSPEX <sup>TM</sup> bar	130
Figure 3.59. Mechanical energy in PERSPEX <sup>TM</sup> bar	131
Figure 3.60. Predicted displacement time record at middle of PERSPEX <sup>TM</sup> bar	132

Figure 3.61. Time record of predicted particle velocity at strain gauge location, on PERSPEX <sup>TM</sup> bar	133
Figure 3.62. Impact force	136
Figure 3.63. Comparison of single-ADF generated loss factor (a) and shear modulus (b), at 20 <sup>0</sup> C, to corresponding experimental quantities at 10 <sup>0</sup> C	137
Figure 3.64. Particle velocity of mass	138
Figure 3.65. Longitudinal displacement of mass vs. time, 3-mm thick filter	139
Figure 3.66. Mechanical energy in bar vs. time, 3-mm thick filter	140

## LIST OF TABLES

Table 3.1. Material parameters for Ti6Al4V	74
Table 3.2. ADF parameters used (5 ADF) for Ti6Al4V alloy	75
Table 3.3. ADF parameters used for Ti6Al4V alloy (1 ADF)	76
Table 3.4. ADF parameters used for PERSPEX <sup>TM</sup> (one ADF)	84
Table 3.5. Material parameters for viscoelastic material	106
Table 3.6. Material parameters for Buna N rubber Durometer 60	114
Table 3.7. ADF parameters used (5 ADF) for Buna N rubber	116
Table 3.8. ADF parameters used (1 ADF) for nitrile rubber	135

## CHAPTER 1. INTRODUCTION

### 1.1. Introduction

Protection from the potentially damaging effects of shock loading is a common design requirement for diverse mechanical structures, ranging from shock accelerometers to spacecraft. High-damping viscoelastic materials are often employed in the design of impact absorbent components. Since shock transients have a wide frequency spectrum, it is imperative to properly model the frequency dependence of material behavior, such as the stiffness and loss moduli.

The current work focuses on the development and verification of two-dimensional finite elements (FE), which incorporate the Anelastic Displacement Fields (ADF) time-domain material damping model. A series of experiments designed to validate the axisymmetric and plane stress finite element models (FEM) were performed. These experiments involved the propagation of shock-generated longitudinal waves through elastic and viscoelastic rods and behavior of elastomeric mechanical filters subjected to shock. The development of such ADF-based finite element models presents an attractive analytical tool to aid in the design of shock absorbent mechanical filters, and it offers an alternative to theoretical investigations of longitudinal wave propagation through viscoelastic rods, which are limited to circular or elliptical cross section rods. The new ADF FEM also create the possibility of determining material moduli frequency dependence by iteratively fitting model predictions to experimental results.

This chapter reviews viscoelastic theory and damping modeling methods employed in a structural dynamics framework. Chapter 1 also discusses theoretical and experimental investigations of shock longitudinal wave propagation through bars and the applications to the calibration of shock accelerometers through the Hopkinson bar method. The current chapter surveys and reviews the existing literature focused on the design of mechanical filters. The objectives, motivation, and an outline of this work are then

presented. The following section offers a survey of linear viscoelasticity and a survey of current damping models used in structural dynamics.

## 1.2. Linear viscoelasticity

The classical theory of elasticity states that for sufficiently small strains, the stress in an elastic solid is proportional to the instantaneous strain and is independent of the strain rate. In a viscous fluid, according to the theory of hydrodynamics, the stress is proportional to the instantaneous strain rate and is independent of the strain. Viscoelastic materials exhibit solid and fluid behavior [1]. Such materials include plastics, rubbers, glasses, ceramics, and biomaterials (muscle). Viscoelastic materials are characterized by constant-stress creep and constant-strain relaxation. Their deformation response is determined by both current and past stress states, and conversely, the current stress state is determined by both current and past deformation states. It may be said that viscoelastic materials have “memory”; this characteristic constitutes the foundation on which their mathematical modeling is based [2].

Linear viscoelastic materials may be defined by either differential or integral constitutive equations [3]. The differential form of the constitutive law for a one dimensional linear viscoelastic solid is shown in Equation (1.1) [3].

$$P\sigma = Q\epsilon \quad (1.1)$$

The quantities  $\sigma$  and  $\epsilon$  are the one dimensional stress and strain, respectively;  $P$  and  $Q$  are the time linear differential operators, which are further expressed as

$$\begin{aligned} P &= \sum_{j=0}^m p_j \frac{\partial^j}{\partial t^j} = \sum_{j=0}^m p_j D^j \\ Q &= \sum_{j=0}^m q_j \frac{\partial^j}{\partial t^j} = \sum_{j=0}^m q_j D^j \end{aligned} \quad (1.2)$$

where  $p_j$  and  $q_j$  are constant. The number of time derivatives retained in the operators  $P$  and  $Q$  are denoted by  $m$  and  $n$ , respectively;  $j$  is the order of differentiation. Equation (1.2) can describe a spring-dashpot model made of multiple spring and dashpots.

The Maxwell model of a one-dimensional viscoelastic material consists of a linear spring and a linear dashpot connected in series as shown in Figure 1.1a. The Kelvin model is consists of a linear spring and a linear damper connected in parallel. If more than one spring or linear damper are to be included in the model (to better approximate material behavior over a frequency range), more terms may be retained in Equation (1.2). The three-parameter model of a standard viscoelastic solid is shown in Figure 1.1b. It consists of a linear spring  $K_1$  in series with a linear Kelvin element [4] (spring  $K$  and dashpot  $C$  in parallel).

Linear viscoelastic stress-strain laws may also be described using hereditary integrals. The applied load consists of infinitesimal steps; the response to each one of these steps is summed to give the total response. The integral form of the one-dimensional viscoelastic constitutive laws is described in Equation 1.3.

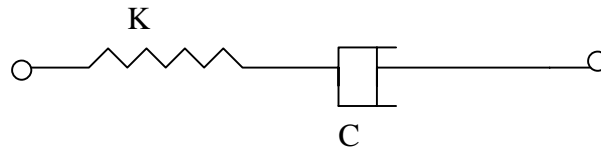


Figure 1.1a. Maxwell model

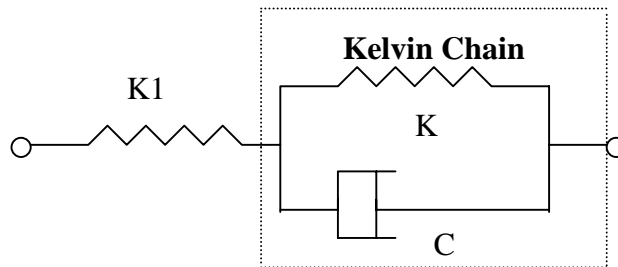


Figure 1.1b. Standard viscoelastic solid

$$\begin{aligned}\varepsilon(t) &= \int_{0-}^t J(t-t') \left[ \frac{\partial \tau(t')}{\partial t'} \right] dt' \\ \text{or} \\ \sigma(t) &= \int_{0-}^t Y(t-t') \left[ \frac{\partial \varepsilon(t')}{\partial t'} \right] dt'\end{aligned}\tag{1.3}$$

$J(t)$  is the creep compliance function and  $Y(t)$  is the relaxation modulus function [3]. The creep compliance function and the relaxation modulus function characterize the material's memory of its past deformations and stresses [4].

Equations (1.1) and (1.3) are equivalent. The creep compliance function and the relaxation modulus may be obtained from the operators  $P$  and  $Q$  through Laplace transforms. If harmonic stress and strain states are considered

$$\begin{aligned}\sigma &= \sigma_0 e^{j\omega t} \\ \varepsilon &= \varepsilon_0 e^{j\omega t}\end{aligned}\tag{1.4}$$

the differential linear viscoelastic constitutive law (Equation 1.1) yields

$$\begin{aligned}\sigma_0 &= K^* \varepsilon_0 \\ K^* &= K' + jK''\end{aligned}\tag{1.5}$$

where  $K^*$  is the material complex modulus and  $K'$  and  $K''$  are the material storage and loss moduli, respectively, corresponding to the circular frequency  $\omega$  [3]. Equation (1.5) states that at a given frequency, a phase shift exists between an oscillatory stress and its corresponding displacement response. Experiments have shown that steady stress-strain trajectories for a linear viscoelastic material are elliptical in shape [5]. Only the relaxation modulus function is needed to completely determine the storage and loss



moduli [4]. The material moduli of linear viscoelastic materials are functions of frequency and temperature; however, they are independent of stress and strain.

### 1.3. Linear material damping

Damping is the dissipation of mechanical energy and is produced by the some non-conservative forces acting on a given structure. Damping may be classified into external and internal, depending upon the nature of the non-conservative forces acting on the structure. External damping is caused by forces acting on the object, such as damping due to air resistance or Coulomb damping due to friction. Internal damping is caused by physical phenomena intimately linked to the structure of the material [6]. In polymers, material damping is a direct result of the relaxation and recovery of the long molecular chains after stress [7].

As stated before, linear damping materials have material moduli that depend on frequency and temperature, but not on strain and stress levels. The loss modulus, introduced in Equation (1.5), is written in terms of the loss factor  $\eta$  as

$$K'' = \eta K' \quad (1.6)$$

The material loss factor is equal to the tangent of the phase angle  $\delta$  between a time harmonic stress input and the corresponding harmonic strain

$$\eta = \tan(\delta) \quad (1.7)$$

The phase angle may be written in terms of the storage and loss moduli as

$$\delta = \tan^{-1}\left(\frac{K''}{K'}\right) \quad (1.8)$$

Both the loss and storage moduli are frequency dependent. Plots of loss factor and Young's modulus versus frequency may be found in Reference [9] and Reference [10]. The frequency dependence of the complex modulus components must be captured accurately; simple models such as Maxwell or Kelvin model are not able to do that. The Maxwell model behaves like a fluid at low frequencies, while the Kelvin model becomes infinitely stiff at high frequencies. Prediction accuracy increases by adding more springs and dampers.

#### 1.4. Damping modeling in finite element analysis

The structural response of a system is determined in computational structural dynamics by solving a set of  $n$  simultaneous, time-dependent equations [11]

$$M \begin{Bmatrix} \ddot{x} \\ \end{Bmatrix} + C \begin{Bmatrix} \dot{x} \\ \end{Bmatrix} + K \{x\} = \{f(t)\} \quad (1.9)$$

where  $M$ ,  $K$  and  $C$  are the mass, stiffness and damping matrices, respectively, and  $\{f(t)\}$  is the time-dependent applied load. Several methods may be used to compute the damping matrix and each one is presented in what follows.

One of the first methods to model damping is that of proportional damping. In this method, the damping matrix is considered to be proportional to the mass and stiffness matrices through two coefficients  $\alpha$  and  $\beta$  (Rayleigh's coefficients) [12]:

$$C = \alpha M + \beta K \quad (1.10)$$

The Rayleigh coefficients are calculated directly from the modal damping ratios  $\zeta_i$ . The damping ratios are the ratio of actual damping to critical damping for a particular mode of vibration. If  $\omega_i$  is the natural circular frequency of the  $i^{\text{th}}$  mode, the Rayleigh parameters satisfy the following relationship:

$$\zeta_i = \frac{\alpha}{2\omega_i} + \frac{\beta\omega_i}{2} \quad (1.11)$$

The drawback of this method is that the damping matrix depends on the arbitrarily determined parameters  $\alpha$  and  $\beta$ , and thus has no physical motivation.

Another well-known approach to model damping is the modal strain energy (MSE) method [13], [14]. The main assumption is that the modes of the damped structure are similar to the real normal modes of the undamped system. Modal analysis of the mechanical system is performed by choosing material properties corresponding to a given frequency and temperature. The effective modal loss factors  $\eta^r$  are given by the weighted sum of the loss factors of each constituent material:

$$\eta^r = \frac{\sum_i \eta_i^r U_i^r}{\sum_i U_i^r} \quad (1.12)$$

where  $U_i^r$  is the strain energy corresponding to component  $i$  in vibration mode  $r$ . The modal loss factors are introduced in the uncoupled modal equations

$$\ddot{\alpha}^r + \eta^r \omega^r \dot{\alpha}^r + \left(\omega^r\right)^2 \alpha^r = l^r(t) \quad (1.13)$$

where  $\alpha^r$  is the modal coordinate,  $\omega^r$  is the undamped frequency of mode  $r$  and  $l^r$  is the associated modal forcing. The displacement  $\{x\}$  of the structure is the superposition of all modes  $\{P^r\}$  of the undamped system multiplied by the corresponding modal coordinate

$$\{x\} = \sum \left\{ P^r \right\} \alpha^r(t) \quad (1.14)$$

The disadvantage of the MSE method is that the effective modal loss factor is obtained iteratively for each vibration mode, since material properties are frequency dependent. The damped modes of vibration are not orthogonal and there is no information on the relative phase of vibration at points on the structure.

Segalman uses a perturbation approach to model linear “slightly” viscoelastic structures [15]. Hereditary integrals, see Equation (1.3) are used in conjunction with the equation of motion and the corresponding nonlinear eigenvalue problem results. This model only applies to “slightly” damped structures. The undamped eigenvalues and eigenmodes need to be found before the computation of the stiffness and damping matrices can occur. This method may not be used to model nonlinear or high-loss linear damping material behavior.

Bagley and Torvik use differential operators of fractional order to model linear frequency dependence of viscoelastic materials [16], [17]. The general form of such model is

$$\sigma(t) + \sum_{m=1}^M b_m D^{\beta_m} \{\sigma(t)\} = E_0 \epsilon(t) + \sum_{n=1}^N E_n D_n^{\alpha} \{\epsilon(t)\} \quad (1.15)$$

where  $E_0$ ,  $E_n$ ,  $b_m$ ,  $\beta$ , and  $\alpha$  are all material properties to be determined experimentally. Time-dependent stresses and strains are related by derivatives of fractional orders. The fractional derivative is

$$D^{\alpha} \{x(t)\} = \frac{1}{\Gamma(1-\alpha)} \frac{d}{dt} \int_0^t \frac{x(\tau)}{(t-\tau)^{\alpha}} d\tau, \quad 0 < \alpha < 1 \quad (1.16)$$

and  $\Gamma$  is the gamma function.

This model connected the molecular theories for uncrosslinked polymer solids and linear viscoelastic models through fractional calculus. By considering the first fractional derivative in each series of Equation (1.15), a five-parameter model is obtained

$$\sigma^*(j\omega) = \left( \frac{E_0 + E_1(j\omega)^\alpha}{1 + b_1(j\omega)^\beta} \right) \varepsilon^*(j\omega) \quad (1.17)$$

where  $\sigma^*(j\omega)$  and  $\varepsilon^*(j\omega)$  are the Fourier transforms of the stress and strain time records, respectively. The frequency dependent complex modulus  $E^*$  is

$$E^* = \left( \frac{E_0 + E_1(j\omega)^\alpha}{1 + b_1(j\omega)^\beta} \right) \quad (1.18)$$

This method only considers the case where  $\alpha=\beta$ . The stiffness matrix of a viscoelastic element was built and the ensuing finite element equations were obtained in the frequency domain. The solutions of the system of equations had to be transformed from the frequency domain back into the time domain. Only loads that have a Laplace transform may be included in subsequent analyses. The Bagley-Torvik approach is only applicable for uncrosslinked polymer solids of linear viscoelastic materials.

Padovan based his computational algorithms for finite element analysis of viscoelastic structures on fractional integral-differential operators [18]. The basis for the model formulation is the fractional derivative by Grunwald [19]

$$D^\alpha \{x(t)\} = \lim_{N \rightarrow \infty} \left\{ \left( \frac{t}{N} \right)^{-\alpha} \sum_{k=0}^{N-1} A_{k+1} x \left( t \left( 1 - \frac{k}{N} \right) \right) \right\} \quad (1.19)$$

where

$$A_{k+1} = \frac{\Gamma(k - \alpha)}{\Gamma(-\alpha)\Gamma(\alpha + 1)} \quad (1.20)$$

The model integrates the fractional derivative of Equation (1.19) in a displacement-based finite element [20] framework by considering a truncated time record of the dependent variable (stress or strain) in Equation (1.15). A viscoelastic, displacement-based, time-domain finite element model results, which may be solved for any type of loading. The Padovan model is valid only for viscoelastic materials that may be modeled through fractional calculus.

Enelund and Lesieutre introduced a fractional derivative model of linear viscoelasticity based on the decomposition of the displacement field into elastic and anelastic displacement fields [21]. A differential equation of fractional order in time describes the evolution equation of the anelastic field and allows this current model to represent weak frequency dependence of damping characteristics. The anelastic displacement field is coupled to the total displacement field through a convolution integral with a Mittag-Leffler function kernel. This viscoelastic model is integrated in a structural dynamics context through the development of related finite element. This method was then used to analyze the response of a viscoelastic bar.

Time- and frequency-domain finite element equations, based on fractional calculus modeling of viscoelastic materials, were developed by Chern [22]. The stress-strain relationship for a three-parameter model based on Equation (1.15) is

$$\sigma(t) = E_0 \varepsilon(t) + \frac{E_1}{\Gamma(1 - \alpha)} \int_0^t (t - \tau)^{-\alpha} \frac{d}{d\tau} (\varepsilon(\tau)) d\tau, \quad t \geq 0, \quad \varepsilon(0) = 0 \quad (1.21)$$

This was then discretized with a first order forward difference,

$$\sigma_n = \left[ E_0 + \frac{E_1}{\Delta t^\alpha \Gamma(2-\alpha)} \right] \varepsilon_n - \left[ \frac{E_1}{\Delta t^\alpha \Gamma(2-\alpha)} \right] \sum_{i=1}^{n-1} \varepsilon_i n_i \quad (1.22)$$

where

$$\begin{aligned} \sigma_n &= \sigma(t_n), \quad \varepsilon_n = \varepsilon(t_n) \\ t_n &- \text{current time} \\ n_i &= -(n-i-1)^{1-\alpha} + 2(n-i)^{1-\alpha} - (n-i+1)^{1-\alpha} \\ i &= 0, \dots, n \end{aligned} \quad (1.23)$$

Then Equation (1.22) and Equation (1.23) were integrated in a finite element model for a three-dimensional isotropic case.

The model developed by Hughes and Golla incorporated the hereditary integral form of the viscoelastic constitutive law in a finite element model [23]. The finite element equations are derived in the Laplace domain through the Ritz technique. The time domain equations are obtained from the frequency domain equations by the linear theory of realizations. The Laplace transform material modulus used in the Golla-Hughes equations is

$$\bar{G}(s) = \frac{1}{s} \left( G^\infty + \sum_{k=1}^n \alpha_k \frac{s^2 + 2\zeta_k \omega_k s}{s^2 + 2\zeta_k \omega_k s + \omega_k^2} \right) \quad (1.24)$$

where  $s=j\omega$ ,  $G^\infty$  is the equilibrium modulus, and  $a_j$  and  $b_j$  are experimentally determined material constants. The method yields a system of second-order matrix differential equations. Internal dissipation coordinates augment the stiffness, damping, and mass matrices. This technique is applicable only for linear viscoelastic materials and may be applied only when the system is initially at equilibrium.

McTavish and Hughes extended the Golla-Hughes model and formulated the GHM (Golla-Hughes-McTavish) model for linear viscoelastic structures [24], [25]. In this new formulation, the material modulus in the Laplace domain becomes

$$\bar{G}(s) = G^\infty \left[ 1 + \sum_i \alpha_i \frac{s^2 + 2\beta_i \xi_i s}{s^2 + 2\beta_i \xi_i s + \xi_i^2} \right] \quad (1.25)$$

where  $G^\infty$  is the equilibrium modulus,  $a_i$ ,  $b_i$  and  $\xi_i$  are experimentally determined material constants. The material modulus is modeled as the sum of mini-oscillators, as shown in Equation (1.25). These oscillators are characterized by the three constants,  $a_i$ ,  $b_i$ ,  $\xi_i$ , and are characterized by a viscous damper, spring and mass. The motion of the mass represents the internal dissipation coordinate. Again, this method leads to a system of second order differential equations of motion in the frequency domain, where the mass, stiffness, and damping matrices are augmented by the internal dissipation coordinates. The stiffness matrix is ill-conditioned and spectral decomposition is needed to remedy the problem.

Yiu introduced another time-domain technique developed to include frequency-dependent damping behavior of linear viscoelastic materials in a finite element framework [26], [27]. This technique employs a generalized Maxwell model to represent material behavior and the dynamic material modulus is defined as

$$G(s) = G^\infty v(s) \quad (1.26)$$

where  $v(s)$  is the viscoelastic operator defined as

$$v(s) = 1 + \sum_{i=1}^m \frac{\alpha_i \tau_i s}{1 + \tau_i s} \quad (1.27)$$



and  $\alpha_i$ , and  $\tau_i$  are constants of the  $i^{\text{th}}$  Maxwell element. This modeling technique is a first order method.

The viscoelastic operator acts on the static elastic stiffness matrix of the structure. As a result, the dynamic stiffness matrix in the Laplace domain is obtained. Internal coordinates are needed so that frequency domain equations may be converted to the time domain. Each internal coordinate is related to a Maxwell element. The viscoelastic operator was modified to be

$$v(s) = 1 + \tau_0 s \sum_{i=1}^m \frac{\alpha_i \tau_i s}{1 + \tau_i s} \quad (1.28)$$

With this change, a dashpot is added in parallel with the generalized Maxwell model to rule out instant elastic response. As with the GHM method, the Yiu method only models linear viscoelastic materials.

Lesieutre developed the “augmenting thermodynamic fields” (ATF) method to model frequency dependent material damping of linear viscoelastic structures in a finite element context [28]. The ATF model the dissipative behavior of linear damping materials. Partial differential equations of evolution and coupled ATF-displacement field equations are found from irreversible thermodynamic theory [29]. A finite element model is then obtained from the discretized system of equations.

An one-dimensional formulation of the ATF model was introduced by Lesieutre and Mingori [30]. The material constitutive equations are derived from the Helmholtz free energy function  $f$ . Stress-strain equations for a simple rod vibrating longitudinally are

$$\sigma = \frac{\partial f}{\partial \epsilon} = E_U \epsilon - \delta \xi \quad (1.29)$$

$$A = -\frac{\partial f}{\partial \xi} = \delta \epsilon - \alpha \xi$$

where  $E_U$  is the unrelaxed or low frequency modulus of elasticity,  $\xi$  is a single ATF, and the affinity  $A$  is to the ATF just as the stress  $\sigma$  is thermodynamically conjugate to the strain  $\epsilon$ . The coupling material property between the mechanical displacement field and the ATF is  $\delta$  while  $\alpha$  relates the change in affinity  $A$  to those in the ATF  $\xi$ .

The ATF evolution equation is determined from the irreversible thermodynamics assumption that the rate of change  $\dot{\xi}$  is proportional to its deviation from an equilibrium value. This results in coupled partial differential equations in terms of the displacement field  $u$  and the gradient of the ATF  $\gamma$ :

$$\rho \ddot{u} - E_U u'' = -\delta \dot{\gamma} \quad (1.30)$$

$$\dot{\gamma} + B\gamma = \left( \frac{B\delta}{\alpha} \right) u''$$

where  $B$  is the inverse of the relaxation time constant at constant strain and  $\rho$  is the density.

The coupled equations of motion are discretized using the method of weighted residuals, and a first order equation system is obtained. The single ATF, rod finite element is shown in Figure 1.2.

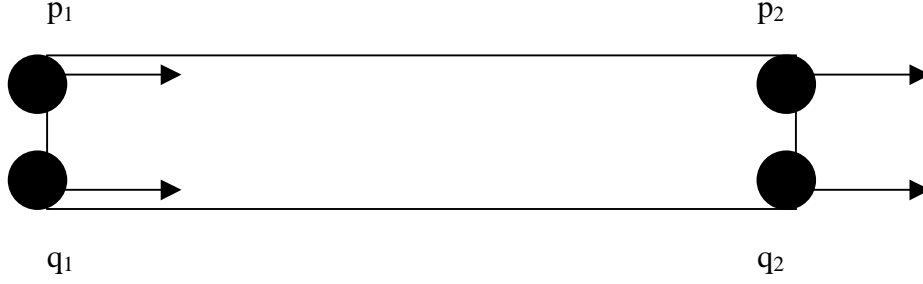


Figure 1.2. ATF rod finite element

For a number of  $N$  ATF, the equations of motion are

$$\rho \ddot{u} - E_u u'' = - \sum_{i=1}^N \delta_i \gamma_i \quad (1.31)$$

$$\dot{\gamma} + B_i \gamma_i = \left( \frac{B_i \delta_i}{\alpha_i} \right) u''$$

More ATF are sometime needed to better approximate frequency dependence of material moduli [31], [32]. The complex modulus may be written as

$$E^* = E_r \left( 1 + \sum_{i=1}^N \Delta_i \frac{(\omega / B_i)^2}{1 + (\omega / B_i)^2} \right) + j E_r \left( \sum_{i=1}^N \Delta_i \frac{(\omega / B_i)^2}{1 + (\omega / B_i)^2} \right) \quad (1.32)$$

where  $E_r$  is the relaxed modulus and  $\Delta_i$  is the relaxation strength of the  $i^{\text{th}}$  ATF. The unrelaxed, or high frequency modulus, and the relaxation strength  $\Delta_i$  is

$$E_u = E_r \left( 1 + \sum_{i=1}^N \Delta_i \right) \quad (1.33)$$

$$\Delta_i = \frac{\delta_i^2}{E_r \alpha_i}$$

The ATF parameters are obtained by iteratively curve fitting the complex modulus of Equation (1.32) to experimental data [33].

The “Anelastic Displacement Field” ADF, method was developed to extend the ATF method to three-dimensional states [34], [35]. The effect of material anelasticity on the displacement field was considered. The displacement field  $u$  was made of an elastic component and an anelastic component:  $u^E(x,t)$  and  $u^A(x,t)$ , respectively

$$u(x,t) = u^E(x,t) + u^A(x,t) \quad (1.34)$$

For a one-dimensional bar, see Figure 1.3., with properties constant along the length, the equation of motion is

$$\rho \ddot{u} - E_u u'' + E_u u''^A = f(t) \quad (1.35)$$

where  $f(t)$  is the applied load.

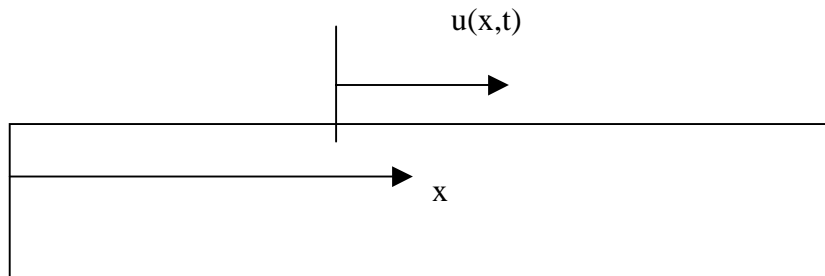


Figure 1.3. One-dimensional bar

The anelastic strain rate is expressed as

$$\frac{\partial \epsilon^A}{\partial t} = -\Omega \left( \epsilon^A - \bar{\epsilon}^A \right) \quad (1.36)$$

where  $\Omega$  is the inverse of relaxation time at constant strain and the equilibrium anelastic strain rate  $\bar{\epsilon}^A$  is coupled to the total strain  $\epsilon$  by a coupling parameter  $c$

$$\bar{\epsilon}^A = \frac{\epsilon}{c} \quad (1.37)$$

Equations (1.36) and (1.37) may be combined in the following form

$$\dot{u}''^A + \Omega u''^A = \frac{\Omega}{c} u'' \quad (1.38)$$

To build a one ADF model, three independent constants are needed:  $E_U$ ,  $c$ , and  $\Omega$ . The complex modulus for a single ADF is, assuming harmonic time dependence of the displacement field  $u$ ,

$$E^* = E_U \left[ 1 - \left( \frac{1}{\frac{ic\omega}{\Omega} + c} \right) \right] \quad (1.39)$$

where  $\omega$  is the circular frequency.

Just like in the ATF model, the ADF parameters are obtained by curve fitting ADF complex moduli to the corresponding experimental data [34]. The equations of motion are discretized by the weighted residuals method to obtain a finite element model.

Multiple ADF may be used to better approximate experimental frequency dependent modulus data. For a one-dimensional rod, the finite element equations are presented in Equation (1.40). ADF rod finite elements, shown in Figure 1.4., were first used in numerical simulation of longitudinal wave propagation through a clamped-free rod by Govindswamy [36].

$$\rho A L_{el} \begin{bmatrix} \frac{1}{3} & \frac{1}{6} \\ \frac{1}{6} & \frac{1}{3} \end{bmatrix} \begin{Bmatrix} \ddot{u}_1 \\ \ddot{u}_2 \end{Bmatrix} + \left( \frac{E_u A}{L_{el}} \right) \begin{bmatrix} 1 & -1 \\ -1 & 1 \end{bmatrix} \begin{Bmatrix} u_1 \\ u_2 \end{Bmatrix} - \left( \frac{E_u A}{L_{el}} \right) \begin{bmatrix} 1 & -1 \\ -1 & 1 \end{bmatrix} \begin{Bmatrix} u_1^A \\ u_2^A \end{Bmatrix} = \begin{Bmatrix} f_1 \\ f_2 \end{Bmatrix} \quad (1.40)$$

$$\left( \frac{c E_u A}{\Omega L_{el}} \right) \begin{bmatrix} \frac{1}{3} & \frac{1}{6} \\ \frac{1}{6} & \frac{1}{3} \end{bmatrix} \begin{Bmatrix} \dot{u}_1 \\ \dot{u}_2 \end{Bmatrix} + \left( \frac{c E_u A}{L_{el}} \right) \begin{bmatrix} 1 & -1 \\ -1 & 1 \end{bmatrix} \begin{Bmatrix} u_1^A \\ u_2^A \end{Bmatrix} - \left( \frac{E_u A}{L_{el}} \right) \begin{bmatrix} 1 & -1 \\ -1 & 1 \end{bmatrix} \begin{Bmatrix} u_1 \\ u_2 \end{Bmatrix} = \begin{Bmatrix} 0 \\ 0 \end{Bmatrix}$$

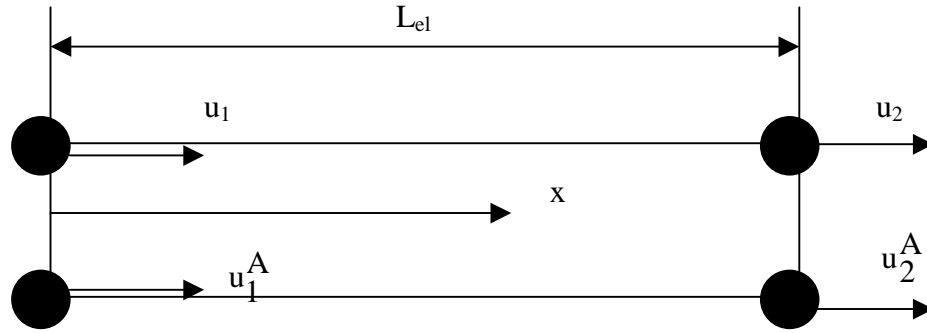


Figure 1.4. ADF rod finite element

Banks introduced a dynamic partial differential equation model based on large deformation elasticity theory [37]. Simple extension and generalized simple shear models are presented.

### 1.5. Longitudinal wave propagation through bars

In this section, a brief introduction to the theory of longitudinal wave propagation through bars is presented. The wave equation governing the elastic longitudinal rod motion is [38]

$$\frac{\partial}{\partial x} \left( E \frac{\partial u}{\partial x} \right) + q = \rho \frac{\partial^2 u}{\partial t^2} \quad (1.41)$$

where  $E$  is the Young's modulus of elasticity, which may be frequency dependent,  $\rho$  is the material density,  $u(x)$  is the displacement at a station  $x$  along the rod and  $q(x)$  is a body force acting along the bar. The main assumption is that during deformation, initially plane sections of the rod remain plane. This equation assumes uniaxial stress and neglects the effects of the Poisson's ratio on the lateral displacements. In an elastic rod, i.e., the Young's modulus has weak or no frequency dependence, the bar velocity is defined as

$$c = \sqrt{\frac{E}{\rho}} \quad (1.42)$$

Propagation or bar velocities in most metals are around 5000 m/s. In contrast, particle velocities in bars are several orders of magnitude less. In an elastic bar, the particle velocity is defined by, [38],

$$V(x, t) = -\frac{c_0 \sigma(x, t)}{E} = c_0 \epsilon(t) \quad (1.43)$$

where  $\sigma$  is the stress in the bar at the given time and location,  $\epsilon$  is the corresponding strain, and  $c_0$  is the bar velocity.

The propagation of stress pulses through longitudinal bars is analyzed next. Consider that an incident stress pulse reaches the fixed boundary of a fixed-free rod. At the fixed boundary, the reflected stress pulse has the same sign as the incident stress pulse. At the free boundary, the reflected pulse has an inverted sign compared to the incident pulse. On a free-free rod, the initial stress pulse reflects repeatedly due to end reflections. Also,

at the free ends of the bar, velocity doubling occurs. All points on the bar move in a series of steps [38], as shown in Figure 1.5.

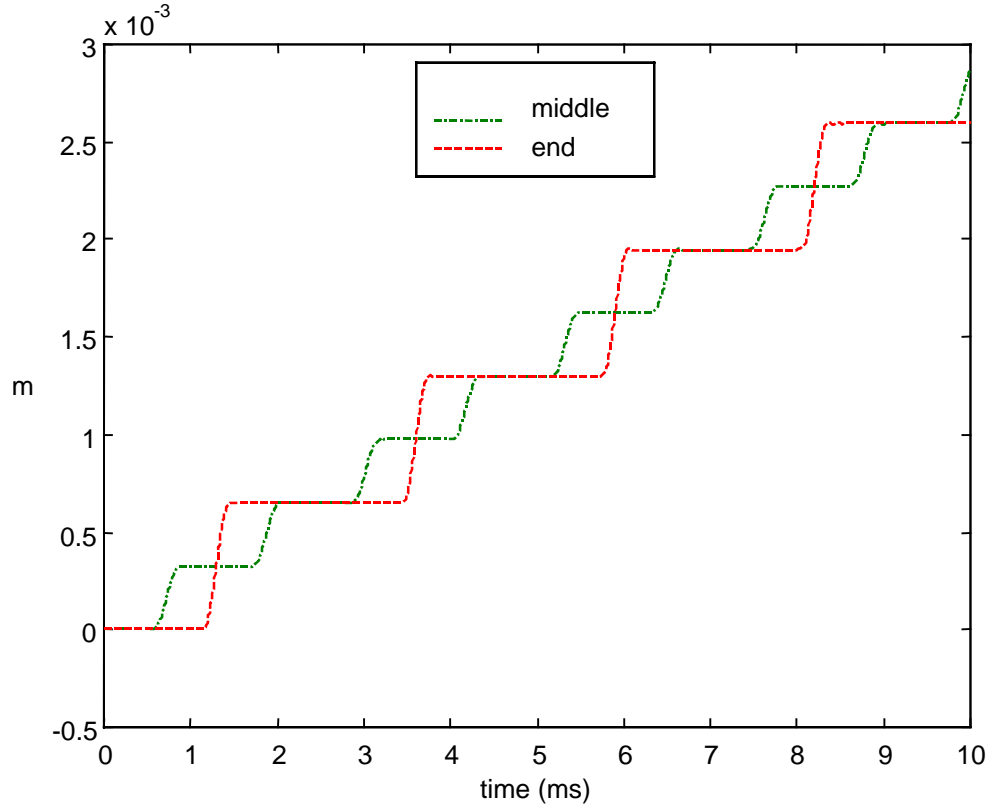


Figure 1.5. Time record of displacement at end and in middle of a free-free elastic bar

During longitudinal wave propagation through a bar, a phenomenon called geometrical dispersion is encountered. As a result of the longitudinal displacement and Poisson's ratio  $\nu$ , displacements in the other two coordinates  $y$  and  $z$  occur ( $v$  and  $w$ , respectively)

$$v = -\nu y \frac{\partial u}{\partial x} \quad (1.44)$$

$$w = -\nu z \frac{\partial u}{\partial x}$$



The wave propagation equation accounting for lateral inertia effects has been developed by Love [38]. If a rectangular pressure pulse incident on one end of a free-free rod occurs, the resulting displacement, as predicted by the distortionless bar theory, would be a ramp function.

The geometrical dispersion phenomenon smoothes the discontinuity at the base of the ramp. It also accounts for small oscillations about the classical displacement result. These results were verified experimentally [38], [40]. Davies [38] presented another interesting result caused by dispersion in a free-free bar of an incident step pulse. The ensuing stress in the bar has an oscillatory character about the result predicted with the distortionless bar theory. Geometrical dispersion becomes a factor only when the wavelength of a given frequency component present in the incident stress pulse  $\Lambda$ ,

$$\Lambda = \frac{2\pi c}{\omega}, \quad (1.45)$$

is on the same order or shorter than the bar radius  $a$ . Lateral inertia causes high-frequency pulse components to travel at lower velocities than lower frequency components, as observed by Kolsky [38] from experimental data. A very sharp pulse ultimately spreads out into a shape several bar diameters in length. Also, there is no sharp discontinuity at the pulse's arrival at a given station long the bar.

Kolsky [38] studied the propagation of stress pulses through viscoelastic rods both analytically and experimentally. In a viscoelastic rod, both viscoelastic attenuation and viscoelastic dispersion phenomena are present. Since viscoelastic materials exhibit frequency dependence of their material moduli, the bar velocity also varies with frequency. If a plane sinusoidal stress wave of amplitude  $\sigma_0 \cos(\omega t)$  propagates along a viscoelastic medium, it attenuates as it reaches a distance  $x$  from the origin and the new amplitude is  $\sigma_0 \exp(-\alpha x) \cos(\omega(t - x/c))$ . The attenuation coefficient is  $\alpha$  and is related to the loss factor  $\tan(\delta)$  by

$$\alpha = \frac{\omega}{2c} \tan(\delta) \quad (1.46)$$

When a mechanical pulse propagates down a viscoelastic bar and is attenuated, high-frequency pulse components travel faster and are attenuated more rapidly than those of lower frequency; note that this effect is opposite to that produced by geometric dispersion. Kolsky [38] has shown by numerical Fourier methods, that it is possible to predict the shape of a mechanical pulse as it propagates down a viscoelastic bar if the material moduli dependence on frequency is known. Furthermore, he was able represent the pulse shape as it travels along a bar in an “Universal Shape” which applies to all high damping polymers and all distances of travel only if the attenuation coefficient is directly proportional to the circular frequency  $\omega$  [40], [41]. These facts were demonstrated experimentally by observing the propagation of a stress pulse, generated by charges of lead azide, along various viscoelastic bars.

#### 1.6. Hopkinson bar shock accelerometer calibration procedure

One practical implementation of longitudinal wave propagation through elastic bars is the Hopkinson bar calibration procedure for shock accelerometers. The following paragraph describes the current Hopkinson bar calibration methodology in general [42-44] and the calibration system currently in use at PCB Piezotronics Inc. in particular [44]. This system is shown in Figure 1.6.

A Hopkinson (or Davies) bar is a long, thin, elastic rod, in which a stress pulse is generated by a projectile (bullet or striker bar) impact at one end of the bar. The test accelerometer is fixed at the other free end. The bar is simply supported at two longitudinal locations. Two resistive strain gauges, located in the middle of the bar and diametrically opposite, are used as reference and to compensate for any bending strains that might occur. The compressive stress pulse generated by the projectile impact resembles a half sine or versed cosine shape. It propagates along the elastic bar at a velocity of  $c_0$ . The pulse is reflected at the free end as a tension wave.

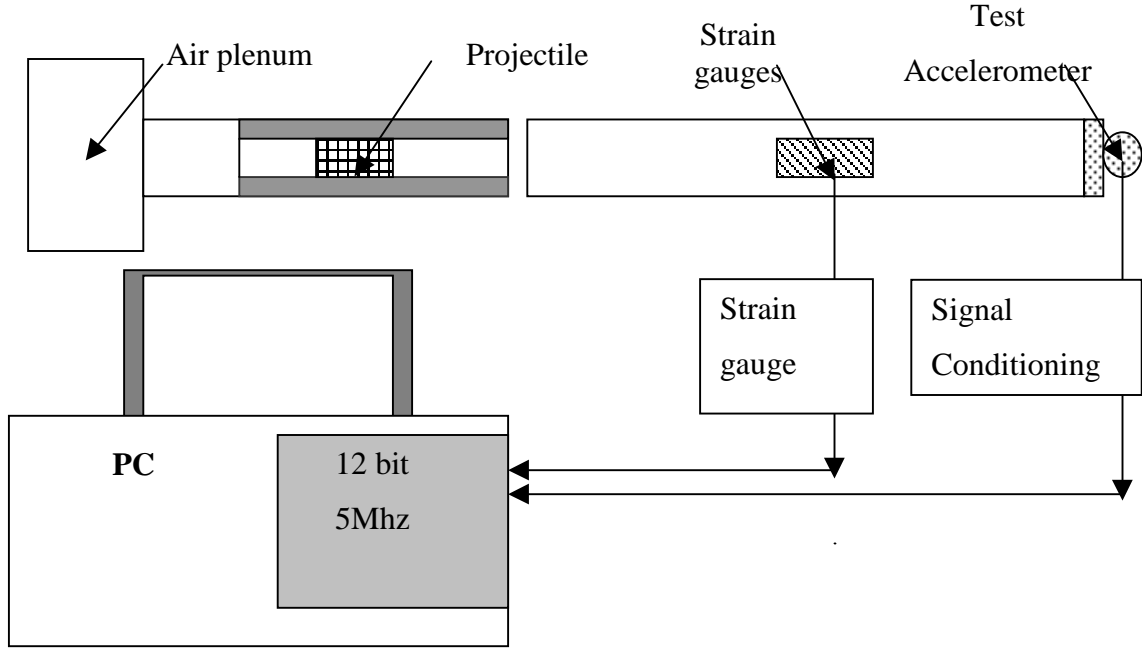


Figure 1.6. Hopkinson bar test setup

The particle velocity at the end of the bar is proportional to the measured strain, Equation 1.43. The reference acceleration at the end is obtained by differentiating the doubled reference particle velocity with respect to time

$$a_r = \frac{dv}{dt} = 2c_0 \frac{d\varepsilon}{dt} \quad (1.47)$$

The sensitivity of the test accelerometer is obtained, for a chosen frequency range, by computing the transfer function between the accelerometer output and the reference acceleration. This method is called the spectral method. The test accelerometer sensitivity  $S_A$  over the frequency range of interest is

$$S_A(j\omega) = \frac{V_A(j\omega)}{V_{ref}(j\omega)}, \quad (1.48)$$

where  $V_A(j\omega)$  and  $V_{\text{ref}}(j\omega)$  are the Fast Fourier Transform (FFT) of the accelerometer output and of the reference, respectively. The frequency range of interest is usually from 1 to 10 kHz. An average of the sensitivity array for the entire frequency range of interest is made to yield a single sensitivity value.

This calibration technique relies upon the following assumptions [44]:

1. The bar is elastic; thus the pulse attenuation due to internal friction is negligible.
2. Geometrical dispersion is kept small in the calibration frequency range of interest by choosing a small enough bar diameter.
3. Impact levels must be small enough to keep strain levels within elastic limits so that linear elastic stress-strain relationships apply.
4. The Hopkinson bar must be long enough to permit the propagating stress pulse to become uniform, i.e. attain a half-sine shape. Such an uniform shape does not develop initially at the impacted end of the bar due to transients caused by projectile/bar interaction [40]. The stress pulse becomes uniform after traveling a distance more than 15 bar diameters.
5. The compression pulse that reaches the accelerometer end must be unaffected by the presence of the test gauge. This is achieved by keeping the length of the accelerometer small in comparison to the wavelengths included in the frequency range of interest and by keeping the accelerometer diameter small in comparison to the bar diameter.

The Hopkinson bar used at PCB Piezotronics is 2.03m long, has a 1.9-cm diameter, and is made out of titanium alloy Ti6Al4V, [44]. For frequencies less than 80 kHz, geometrical dispersion is negligible. The measured attenuation for this titanium alloy bar is less than 3%. A technician releases a trigger that allows compressed air from the air plenum to push a projectile through the launch tube. The projectile strikes the bar at one of the free ends. The velocity of the projectile and the amplitude of the stress pulse are controlled by the air pressure inside the plenum chamber. The impact projectile may be made out of steel or DELRIN<sup>TM</sup>, a plastic material. The shape (blunt or sharp impact

end) and material of the projectile also influence the duration and shape of the resulting stress pulse. The stress pulse generated by a steel bullet has a shorter duration and higher amplitude than the one created by a plastic bullet; a flat-end bullet causes a shorter and stronger stress pulse than a sharp-end projectile.

A fast Gage<sup>TM</sup> data acquisition board (5 megasamples/second and 12 bit A/D) controlled by a Labview<sup>TM</sup> based code (developed by the author) acquires and displays both strain gauge and accelerometer traces, corresponding to the first and second stress pulses, as shown in Figure 1.7. The technician then selects the data record of the first incident strain gauge pulse and another record of the first accelerometer transient with the cursors provided. The code computes and displays the sensitivity of the accelerometer for the corresponding reference acceleration level, in g's ( $1\text{ g} = 9.806\text{ m/s}^2$ ), as shown in Figures 1.7. and 1.8. It also displays the particle velocity along the bar, the power spectrum of the accelerometer and strain gauge incident responses, between the incident and the reflected strain gauge power spectrum and the sensitivity deviation with respect to the vibration sensitivity measured at 100 Hz, Figure 1.8. After repeating the calibration procedures for various shock levels and recording sensitivity and zero-shift, a linearity plot of sensitivity versus reference acceleration is obtained.

Zero-shift is defined as an undesired change in the accelerometer's zero acceleration level after the accelerometer has been subjected to high g shock levels, see Figure 1.7. It is expressed as a percentage of the peak acceleration. Some shock accelerometer designs employ a mechanical filter (usually made of a viscoelastic material) to protect the sensing element from the effect of very high shock transients. The response of such accelerometers may exhibit significant zero-shift when subjected to very high shock levels [44]. Some shock accelerometer designs employ a mechanical filter (usually made of a viscoelastic material) to protect the sensing element from the effect of very high shock transients. The response of such accelerometers may exhibit significant zero-shift when subjected to very high shock levels [44].

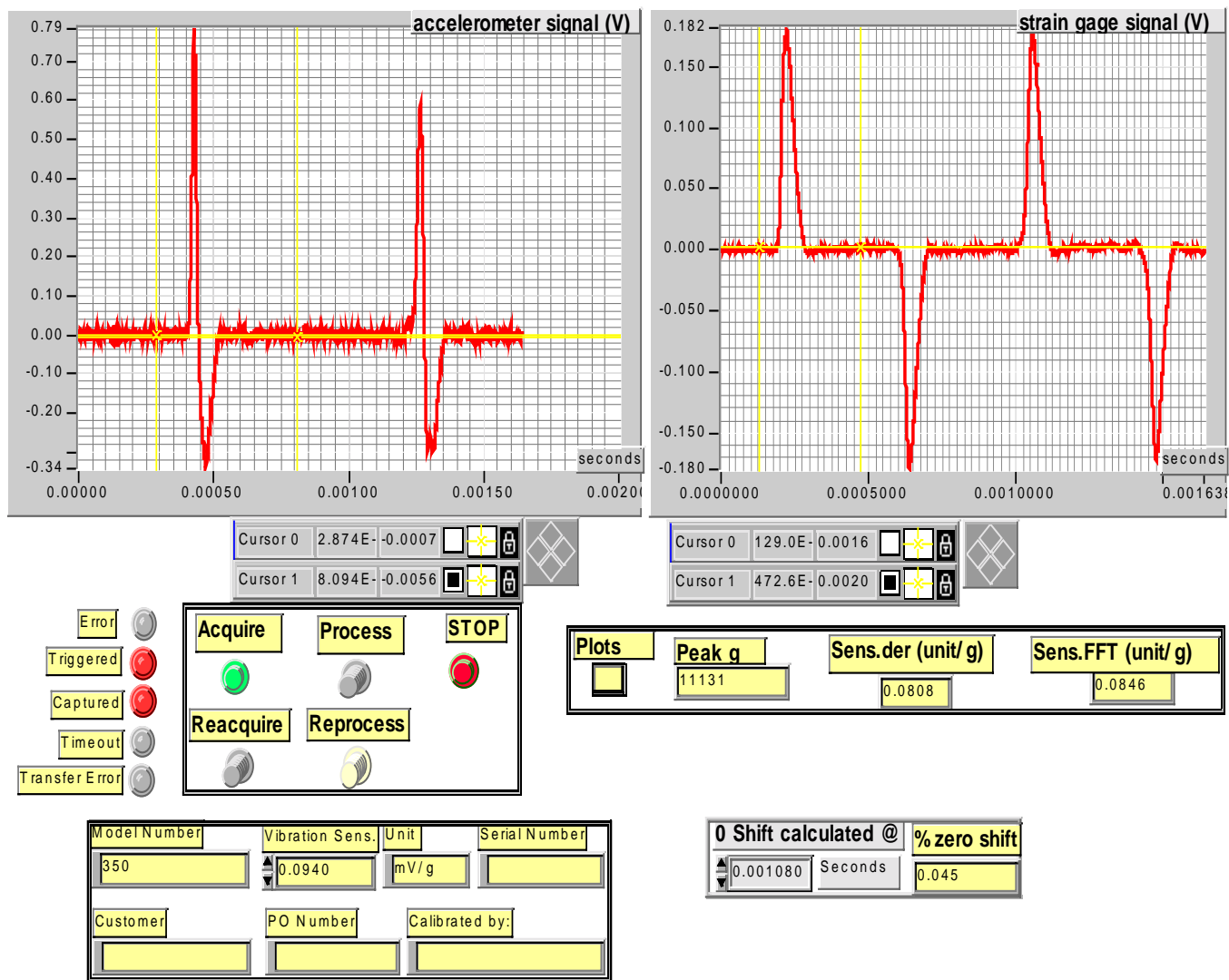


Figure 1.7. Front panel of Labview™ data acquisition code showing acquired signals, computed sensitivity, zero-shift and shock level

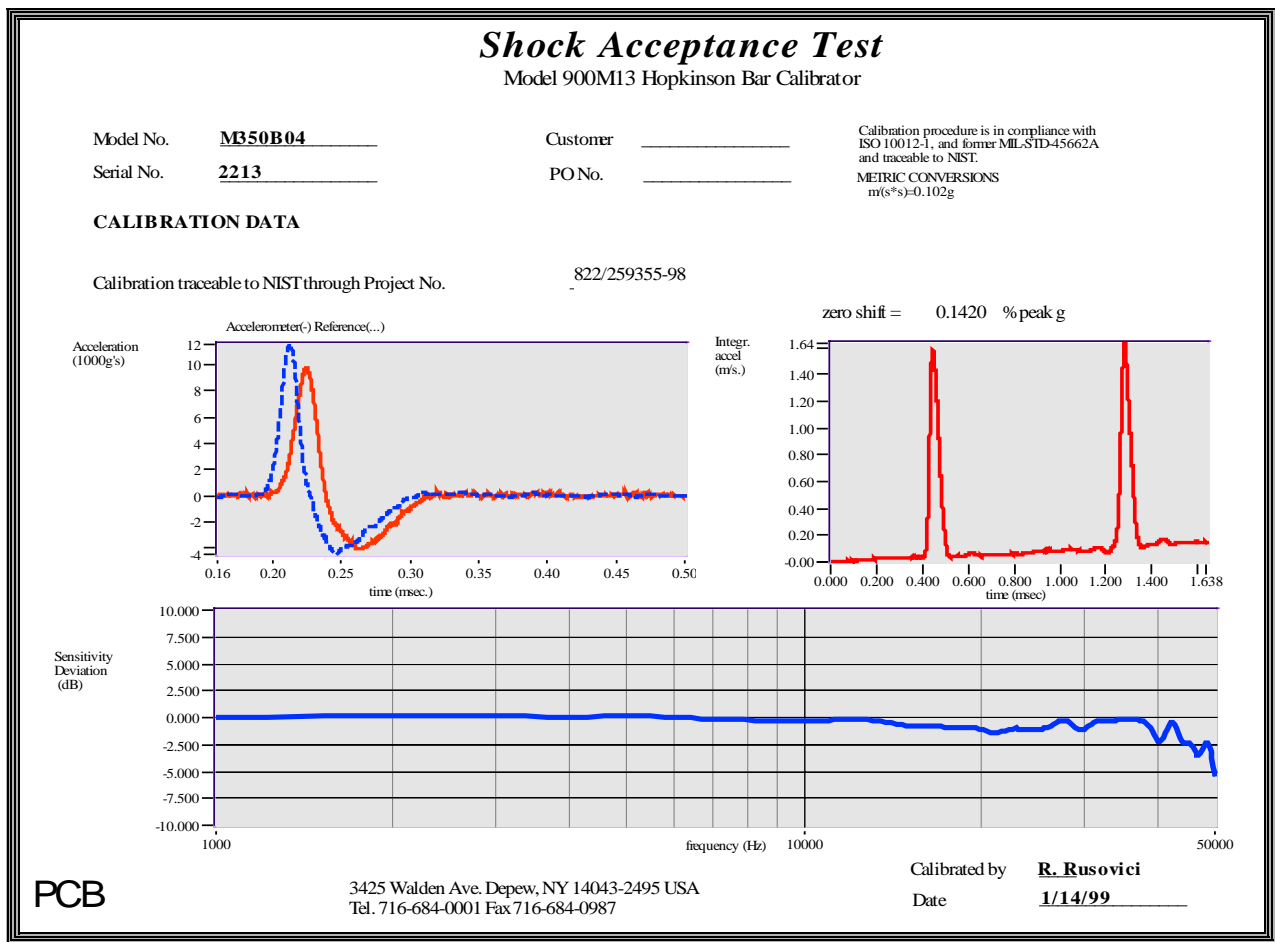


Figure 1.8. Sensitivity data for an accelerometer

### 1.7. Viscoelastic mechanical filter designs for shock accelerometers

As mentioned in Section 1.6, shock accelerometer sensing elements require protection from frequency components of input shock spectra found beyond the frequency range of interest. Shock accelerometers are generally designed to have their resonant frequency well above the frequency range of interest; however some short duration shock transients, whose shape approach that of a Dirac delta function, contain frequency components above the resonant frequency of most shock accelerometers [44]. Proper design of mechanical filters for shock accelerometers allows good protection of the sensing

element from harmful shock transients. Very few papers address the design of mechanical filters for shock accelerometers. Even fewer use a finite element approach to study the shock response of a shock accelerometer model comprising a mechanical filter. One paper that addresses the use of finite elements and frequency dependent damping models for design of shock accelerometer comprising a mechanical filter is that published by Oyadiji et al. [45]. In this paper, a model of a mechanical filter made of a 4-mm thick and 40-mm diameter viscoelastic disk sandwiched between two identical metal plates is analyzed with a finite element approach. The frequency-domain complex Young's modulus is transformed to the time-domain extensional relaxation function using a collocation method. The finite element code accepts viscoelastic data in terms of Prony series coefficients. The Wiechert-Kelvin model of viscoelasticity states that the extensional relaxation modulus is

$$E(t) = E_e + \sum_k E_k \exp(-t / \tau_k) \quad (1.49)$$

where  $\tau_k$  is the relaxation time constant,  $t$  is the time,  $E_e$  is the equilibrium or long-term modulus, and  $E_k$  are the relative relaxation moduli. This model is applied to the time-domain data, and Equation (1.49) is rewritten to include the instantaneous modulus (the modulus at time  $t=0$  or when  $k=0$ ),

$$E_j = E(t_j) = E_g \left( 1 - \sum_k e_k \left[ 1 - \sum_k \exp\left(-\frac{t}{\tau_k}\right) \right] \right), \quad (1.50)$$

where  $e_k = E_k / E_g$ ;  $k = 0, 1, 2, \dots, N$ ;  $j = 1, 2, \dots, k$ ;  $E_j$  are the derived relaxation moduli,  $E_g$  is the glassy modulus,  $e_k$  is the modulus ratio. Equation (1.50) represents the Prony series. These coefficients are derived by curve fitting the derived time-domain extensional relaxation modulus data to experimental data. The curve fit coefficients are determined through a collocation method. The finite element mesh employs axisymmetric finite elements for incompressible and near incompressible material behavior. The filters are subjected to a half sine acceleration pulse of  $10000 \text{ m/s}^2$  and of



$10^{-4}$  second duration. The paper analyzes the shock response of five mechanical filter viscoelastic materials. No comparison to experiment is made. Frequency-dependent modulus data is given for the five materials, but no density information is presented.

Tomlinson et al. [46] continued to investigate methods of designing mechanical filters with commercial finite element code. The finite element code ABAQUS<sup>TM</sup> was used to predict large static and dynamic strains, and to investigate the optimum finite element mesh from a computational point of view. The predicted results matched well the experimental results.

Bateman developed a mechanical filter for a piezoresistive shock accelerometer [47]. The design approach was purely experimental. The Hopkinson bar was used to perform a frequency response analysis between the accelerometer with mechanical filter and the reference acceleration obtained from strain gauge readings (see previous Section 1.6). The mechanical filter was tuned so that its power spectrum matched that of the reference acceleration in order to prevent the filter from amplifying the shock pulse.

Chu discussed the critical design parameters for a mechanical filter [48]. They are

- a) filter-accelerometer combination must be robust to shock levels;
- b) amplification of the mechanical filter must be very low since, otherwise, the linearity of the passband data would be negatively affected; and
- c) relative displacement between transducer and mounting surface must not exceed the linear range of spring/ damping materials and also must prevent the accelerometer from “bottoming” out.

An accelerometer with a mechanical filter was successfully built and tested, based on these above principles.

### 1.8. Objectives and Motivation of the Current Research

The objectives of the current research are listed below.

- 1) To model mechanical filters subjected to shock loading

It is desirable to accurately model mechanical filters since they are used often in engineering practice to alleviate or eliminate shock transients. Theoretical simulations and experiments involving mechanical filters subjected to shock will be conducted, and the results will be compared to ADF model predictions.

- 2) To study longitudinal wave propagation through viscoelastic bars.

Longitudinal wave propagation along a viscoelastic PERSPEX<sup>TM</sup> bar will be studied with an ADF axisymmetric and plane-stress finite element model. Finite element model predictions will be compared to theory and experiment. The ability of the new models to capture such phenomena as geometric dispersion, and viscoelastic dispersion and attenuation will be analyzed.

- 3) To develop single and multiple ADF axisymmetric and plane stress finite elements.

Finite elements are needed to properly model three-dimensional and bi-dimensional viscoelastic structures with frequency dependent material properties. These new finite elements will be based upon the Anelastic Displacement Fields (ADF) theory. Theoretical simulations and experiments, involving longitudinal wave propagation through elastic and viscoelastic bars, will be used to validate ADF plane stress and axisymmetric finite element model results.

- 4) Determine material moduli frequency dependence using Hopkinson bar experiments

This study will also focus on the determination of material moduli frequency dependence by curve fitting ADF model predicted results to experimental displacement data, i.e., match frequency content and magnitude of predicted and experimental displacement pulses.

## 1.9. Outline

To attain the goals set forth in the preceding section, this work addresses the enumerated topics in the following Chapters:

Chapter 2: This chapter presents the theoretical framework and develops single and multiple ADF plane stress and axisymmetric linear finite elements. These new types of finite elements are created to aid in the modeling of complicated three-dimensional and two-dimensional structures, such as viscoelastic mechanical filters, beams with viscoelastic damping layers etc.;

Chapter 3: This chapter compares results of the ADF axisymmetric and plane stress finite elements against theoretical and experimental results. The new finite elements are used to study longitudinal wave propagation in elastic and viscoelastic bars, and to model behavior of mechanical filters subjected to shock transients. It presents a method to determine material moduli frequency dependence by curve fitting ADF model results to corresponding experimental values;

Chapter 4: This chapter summarizes current work and suggests future research.

## CHAPTER 2. MODEL DEVELOPMENT

### 2.1. Development of the plane stress triangular ADF finite element

This chapter shows how frequency-dependent material behavior modeled with anelastic displacement fields (ADF) is incorporated in a finite element framework and presents the development of two new types of ADF finite elements: the displacement based triangular plane stress and the triangular axisymmetric finite element. These new types of finite elements permit the modeling of complex 3-D viscoelastic structures and the understanding of frequency dependence in such structures. First, the linear ADF equations of motion and the material constitutive equations are presented; then, the ADF finite element equations are developed.

The ADF method was chosen to develop a finite element model since [33]

- it has a physical basis based on the principles of irreversible thermodynamics and
- it has the potential to model both weak and strong frequency dependent material behavior.

An ADF-based model is characterized by time domain equations. These time domain equations coupled with an appropriate time integration scheme offer the possibility of predicting structure response to shock loads.

#### 2.1.1. Assumptions and stress-strain equations

In this work, the single-ADF, plane-stress, triangular finite element is created to model bars of rectangular cross section subjected to transient loading. The two-dimensional plane stress finite element allows the capturing of longitudinal wave propagation phenomena such as geometric dispersion.

### 2.1.1.1. Plane stress approximation

According to the theory of elasticity, the following assumptions exist for plane stress

$$\begin{aligned}
 \sigma_x (= \sigma_1), \sigma_y (= \sigma_2), \tau_{xy} (= \sigma_6) &\neq 0 \\
 \varepsilon_x \left( = \varepsilon_1 = \frac{\partial u}{\partial x} \right), \varepsilon_y \left( = \varepsilon_2 = \frac{\partial v}{\partial y} \right), \varepsilon_z (= \varepsilon_3), \gamma_{xy} \left( = \varepsilon_6 = \frac{\partial u}{\partial y} + \frac{\partial v}{\partial x} \right) &\neq 0 \\
 \tau_{zy} (= \sigma_5) = \tau_{zx} (= \sigma_4) = \sigma_z (= \sigma_3) &= 0 \\
 \gamma_{xz}, \gamma_{zy} &= 0
 \end{aligned} \tag{2.1}$$

The plane stress element is shown in Figure 2.1. The displacement field is given only by displacements  $u$  and  $v$  in the Cartesian and orthogonal  $x$  and  $y$  directions, respectively [20]. Only the stresses in the  $x$  and  $y$  direction are nonzero and contribute to internal work; however, from Equation (2.1) it may be seen that the strain in the  $z$  direction is not zero.

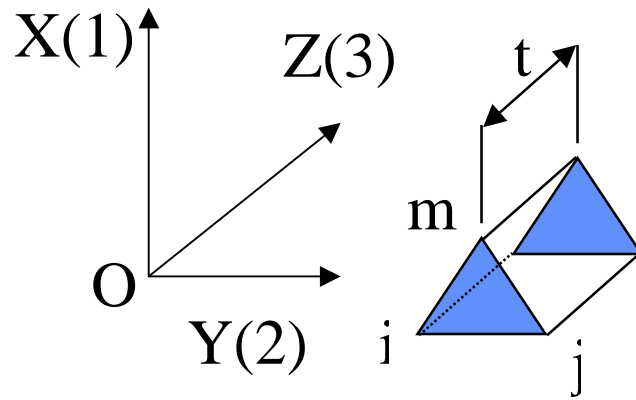


Figure 2.1. Plane-stress finite element

### 2.1.1.2. ADF constitutive equations

The ADF approach focuses on the effects that irreversible thermodynamical processes have on the displacement field. The total displacement field is considered to be the sum of elastic and anelastic components [33]

$$u(x, t) = u^E(x, t) + u^A(x, t) \quad (2.2)$$

where  $u^E(x, t)$  is the elastic displacement fields and the  $u^A(x, t)$  is the anelastic displacement field. The strain tensor is defined by linear strain-displacement equations

$$\varepsilon_{kl} = \frac{1}{2} \left( \frac{\partial u_k}{\partial x_l} + \frac{\partial u_l}{\partial x_k} \right), \quad k, l = 1, 2, 3 \quad (2.3)$$

Strains are also described in compressed matrix notation, using the conversion

$$\begin{aligned} \varepsilon_1 &= \varepsilon_{11} \\ \varepsilon_2 &= \varepsilon_{22} \\ \varepsilon_3 &= \varepsilon_{33} \\ \varepsilon_4 &= 2\varepsilon_{23} \\ \varepsilon_5 &= 2\varepsilon_{31} \\ \varepsilon_6 &= 2\varepsilon_{12} \end{aligned} \quad (2.4)$$

The stress-strain relationship for an elastic material may be expressed in tensor form as

$$\sigma_{ij} = E_{ijkl} \varepsilon_{kl}^E \quad (2.5a)$$

or in compressed matrix form

$$\{\sigma\} = [E] \{\varepsilon^E\} \quad (2.5b)$$

where  $\{\varepsilon^E\}$  is vector consisting of the elastic strains and  $[E]$  is a matrix consisting of unrelaxed or high frequency material elastic constants. Equation (2.5) may be expressed with the help of invariant scalar moduli as, [33]

$$\{\sigma\} = \sum_m \beta_m [M_m] \{\epsilon^E\} = \left( \sum_m \beta_m [M_m] \right) \{\epsilon^E\} \quad (2.6)$$

where  $[M_m]$  is the strain weighting matrix and  $\beta_m$  is the corresponding scalar modulus. For an isotropic material, Equation (2.6) takes the form

$$\{\sigma\} = \beta_K M_K \{\epsilon^E\} + \beta_G M_G \{\epsilon^E\} \quad (2.7)$$

where  $\beta_K$  and  $\beta_G$  are the bulk and shear moduli, respectively, and the matrices  $M_K$  and  $M_G$  are

$$M_K = \begin{bmatrix} 1 & 1 & 1 & 0 & 0 & 0 \\ 1 & 1 & 1 & 0 & 0 & 0 \\ 1 & 1 & 1 & 0 & 0 & 0 \\ 0 & 0 & 0 & 0 & 0 & 0 \\ 0 & 0 & 0 & 0 & 0 & 0 \\ 0 & 0 & 0 & 0 & 0 & 0 \end{bmatrix}$$

$$M_G = \begin{bmatrix} \frac{4}{3} & -\frac{2}{3} & -\frac{2}{3} & 0 & 0 & 0 \\ -\frac{2}{3} & \frac{4}{3} & -\frac{2}{3} & 0 & 0 & 0 \\ -\frac{2}{3} & -\frac{2}{3} & \frac{4}{3} & 0 & 0 & 0 \\ 0 & 0 & 0 & 1 & 0 & 0 \\ 0 & 0 & 0 & 0 & 1 & 0 \\ 0 & 0 & 0 & 0 & 0 & 1 \end{bmatrix} \quad (2.8)$$

Since the elastic strain is the difference between the total strain and the anelastic strain, the Equation (2.5) may be written in compressed matrix and vectorial form as, respectively,

$$\{\sigma\} = [E] \left( \{\epsilon\} - \{\epsilon^A\} \right) \quad (2.9a)$$

$$\sigma_{ij} = E_{ijkl} \left( \epsilon_{kl} - \epsilon_{kl}^A \right) \quad (2.9b)$$

where  $\{\epsilon\}$  and  $\{\epsilon^A\}$  are vectors containing the total and anelastic strains, respectively.

The stresses ( $\sigma_i$ ,  $i=1,2..6$ ), and anelastic stresses ( $\sigma_i^A$ ) may be expressed in terms of the anelastic strain  $\epsilon_i^A$  and total strains  $\epsilon_i$  as [33]

$$[\sigma] = \beta_K M_K \left( \{\epsilon\} - \{\epsilon^A\} \right) + \beta_G M_G \left( \{\epsilon\} - \{\epsilon^A\} \right) \quad (2.10)$$

or

$$\begin{bmatrix} \sigma_1 \\ \sigma_2 \\ \sigma_3 \\ \sigma_4 \\ \sigma_5 \\ \sigma_6 \end{bmatrix} = \left( \beta_K \begin{bmatrix} 1 & 1 & 1 & 0 & 0 & 0 \\ 1 & 1 & 1 & 0 & 0 & 0 \\ 1 & 1 & 1 & 0 & 0 & 0 \\ 0 & 0 & 0 & 0 & 0 & 0 \\ 0 & 0 & 0 & 0 & 0 & 0 \\ 0 & 0 & 0 & 0 & 0 & 0 \end{bmatrix} + \beta_G \begin{bmatrix} \frac{4}{3} & -\frac{2}{3} & -\frac{2}{3} & 0 & 0 & 0 \\ -\frac{2}{3} & \frac{4}{3} & -\frac{2}{3} & 0 & 0 & 0 \\ -\frac{2}{3} & -\frac{2}{3} & \frac{4}{3} & 0 & 0 & 0 \\ 0 & 0 & 0 & 1 & 0 & 0 \\ 0 & 0 & 0 & 0 & 1 & 0 \\ 0 & 0 & 0 & 0 & 0 & 1 \end{bmatrix} \right) \begin{bmatrix} \epsilon_1 - \epsilon_1^A \\ \epsilon_2 - \epsilon_2^A \\ \epsilon_3 - \epsilon_3^A \\ \epsilon_4 - \epsilon_4^A \\ \epsilon_5 - \epsilon_5^A \\ \epsilon_6 - \epsilon_6^A \end{bmatrix} \quad (2.10b)$$

If the plane stress approximations are used, Equation (2.10b) may be simplified to

$$\begin{bmatrix} \sigma_1 \\ \sigma_2 \\ \sigma_3 \\ \sigma_6 \end{bmatrix} = \beta_K \begin{bmatrix} 1 & 1 & 1 & 0 \\ 1 & 1 & 1 & 0 \\ 1 & 1 & 1 & 0 \\ 0 & 0 & 0 & 0 \end{bmatrix} \begin{bmatrix} \epsilon_1 - \epsilon_1^A \\ \epsilon_2 - \epsilon_2^A \\ \epsilon_3 - \epsilon_3^A \\ \epsilon_6 - \epsilon_6^A \end{bmatrix} + \beta_G \begin{bmatrix} \frac{4}{3} & -\frac{2}{3} & -\frac{2}{3} & 0 \\ -\frac{2}{3} & \frac{4}{3} & -\frac{2}{3} & 0 \\ -\frac{2}{3} & -\frac{2}{3} & \frac{4}{3} & 0 \\ 0 & 0 & 0 & 1 \end{bmatrix} \begin{bmatrix} \epsilon_1 - \epsilon_1^A \\ \epsilon_2 - \epsilon_2^A \\ \epsilon_3 - \epsilon_3^A \\ \epsilon_6 - \epsilon_6^A \end{bmatrix} \quad (2.11)$$



In the plane stress case, the stress in the Z Cartesian direction is zero, however

$$\sigma_3 = \left( \beta_K + \frac{4}{3} \beta_G \right) (\varepsilon_3 - \varepsilon_3^A) + \left( \beta_K - \frac{2}{3} \beta_G \right) \left[ (\varepsilon_1 - \varepsilon_1^A) + (\varepsilon_2 - \varepsilon_2^A) \right] = 0 \quad (2.12)$$

As a result, the relationship between the strains  $\varepsilon_3$  and  $\varepsilon_3^A$  may be found in terms of the strains in the Cartesian X and Y directions ( $\varepsilon_1$  and  $\varepsilon_2$ , respectively):

$$\begin{aligned} (\varepsilon_3 - \varepsilon_3^A) &= - \frac{\left( \beta_K - \frac{2}{3} \beta_G \right)}{\left( \beta_K + \frac{4}{3} \beta_G \right)} \left[ (\varepsilon_1 - \varepsilon_1^A) + (\varepsilon_2 - \varepsilon_2^A) \right] = \dots \\ &= - \frac{E_2}{E_1} \left[ (\varepsilon_1 - \varepsilon_1^A) + (\varepsilon_2 - \varepsilon_2^A) \right] = - \frac{E_2}{E_1} (\varepsilon_1 + \varepsilon_2) + \frac{E_2}{E_1} (\varepsilon_1^A + \varepsilon_2^A) \end{aligned} \quad (2.13)$$

If the anelastic strains would be neglected, Equation (2.13) would be reduced to the well-known formula from the theory of elasticity [20]

$$\varepsilon_3^E = - \frac{E_2}{E_1} (\varepsilon_1^E + \varepsilon_2^E) \quad (2.14)$$

where

$$\begin{aligned} E_1 &= \beta_K + \frac{4}{3} \beta_G \\ E_2 &= \beta_K - \frac{2}{3} \beta_G \\ E_3 &= \beta_G \end{aligned} \quad (2.15)$$

The relationship between the anelastic stresses and the total and anelastic strains must be found. The same hypotheses that were valid for the elastic stress and strains are considered for the anelastic stresses and strains; the plane stress approximations are

$$\begin{aligned}
& \sigma_z^A (= \sigma_1^A), \sigma_y^A (= \sigma_2^A), \tau_{XY}^A (= \sigma_6^A) \neq 0 \\
& \varepsilon_x^A (= \varepsilon_1^A = \frac{\partial u^A}{\partial x}), \varepsilon_y^A (= \varepsilon_2^A = \frac{\partial v^A}{\partial y}), \varepsilon_z^A (= \varepsilon_3^A), \\
& \gamma_{xy}^A (= \varepsilon_6^A = \frac{\partial u^A}{\partial y} + \frac{\partial v^A}{\partial x}) \neq 0 \\
& \tau_{zy}^A (= \sigma_5^A) = \tau_{xy}^A (= \sigma_4^A) = \sigma_z^A (= \sigma_3^A) = 0 \\
& \gamma_{zy}^A, \gamma_{xz}^A = 0
\end{aligned} \tag{2.16}$$

The relationship between the anelastic stresses, and the total and anelastic strains is found from thermodynamics by selecting the total and anelastic strains as dependent field variables. For a reversible isothermal process, the differential of the Helmholtz free energy density function is [28]

$$dF = \sigma_{ij} d\varepsilon_{ij} \tag{2.17}$$

It may be seen that for isothermal reversible processes, the strain energy density function equals the Helmholtz function. Both anelastic and total stress must satisfy the following conditions respective to the Helmholtz function [33]:

$$\begin{aligned}
\sigma &= \frac{\partial F}{\partial \varepsilon}; \\
\sigma^A &= - \frac{\partial F}{\partial \varepsilon^A}
\end{aligned} \tag{2.18}$$

From thermodynamic considerations and for small deformations, the strain energy density function is a positive definite function of the strains [28]. The quadratic form of the free energy function may be found by considering Equation (2.9a)

$$F = \frac{1}{2} \left( E_{ijkl} \epsilon_{ij} \epsilon_{kl} - 2E_{ijkl} \epsilon_{ij} \epsilon_{kl}^A + E_{ijkl}^A \epsilon_{kl}^A \epsilon_{ij}^A \right) - \text{tensor form}$$

or

$$F = \frac{1}{2} \left\{ \begin{Bmatrix} \{\epsilon\} \\ \{\epsilon^A\} \end{Bmatrix} \right\}^T \begin{bmatrix} [E] & [-E] \\ [-E] & [E^A] \end{bmatrix} \left\{ \begin{Bmatrix} \{\epsilon\} \\ \{\epsilon^A\} \end{Bmatrix} \right\} - \text{matrix form} \quad (2.19)$$

where  $[E^A]$  is a matrix made of anelastic material constants. If the tensor form of Equation (2.19) is substituted into Equation (2.18), the following equation is obtained in tensor and matrix form, respectively

$$\sigma_{ij}^A = E_{ijkl} \epsilon_{kl} - E_{ijkl}^A \epsilon_{kl}^A \quad (a)$$

$$\text{or} \quad (2.20)$$

$$\left\{ \sigma^A \right\} = [E] \left\{ \epsilon \right\} - [E^A] \left\{ \epsilon^A \right\} \quad (b)$$

Equation (2.20b) can be expressed as

$$\left\{ \sigma^A \right\} = \sum_m \beta_m [M_m] \left( \left\{ \epsilon \right\} - C_m \left\{ \epsilon^A \right\} \right) \quad (2.21)$$

if the assumption that anelastic behavior is similar to elastic behavior is made. The scalar parameter  $C_m$  is equal to

$$C_m = \frac{\beta_m^A}{\beta_m} = \frac{1 + \Delta_m}{\Delta_m}, \quad m = K, G \quad (2.22)$$

and describes the coupling between the physical relaxation process (characterized by the relaxation strength  $\Delta_m$ ) and the total displacement field (K and G refer to the bulk and, respectively, shear moduli). By further expanding Equation (2.21), the constitutive equations for the anelastic stress are found to be

$$\{\sigma^A\} = \beta_K M_K \left( \{\varepsilon\} - C_K \{\varepsilon^A\} \right) + \beta_G M_G \left( \{\varepsilon\} - C_G \{\varepsilon^A\} \right) \quad (2.23)$$

By expanding Equation (2.23), as in [33], the following results are obtained

$$\begin{aligned} \begin{bmatrix} \sigma_1^A \\ \sigma_2^A \\ \sigma_3^A \\ \sigma_4^A \\ \sigma_5^A \\ \sigma_6^A \end{bmatrix} &= \beta_K \begin{bmatrix} 1 & 1 & 1 & 0 & 0 & 0 \\ 1 & 1 & 1 & 0 & 0 & 0 \\ 1 & 1 & 1 & 0 & 0 & 0 \\ 0 & 0 & 0 & 0 & 0 & 0 \\ 0 & 0 & 0 & 0 & 0 & 0 \\ 0 & 0 & 0 & 0 & 0 & 0 \end{bmatrix} \begin{bmatrix} \varepsilon_1 \\ \varepsilon_2 \\ \varepsilon_3 \\ \varepsilon_4 \\ \varepsilon_5 \\ \varepsilon_6 \end{bmatrix} - C_K \begin{bmatrix} \varepsilon_1^A \\ \varepsilon_2^A \\ \varepsilon_3^A \\ \varepsilon_4^A \\ \varepsilon_5^A \\ \varepsilon_6^A \end{bmatrix} + \dots \\ &+ \beta_G \begin{bmatrix} \frac{4}{3} & -\frac{2}{3} & -\frac{2}{3} & 0 & 0 & 0 \\ \frac{2}{3} & \frac{4}{3} & -\frac{2}{3} & 0 & 0 & 0 \\ -\frac{2}{3} & \frac{2}{3} & \frac{4}{3} & 0 & 0 & 0 \\ -\frac{2}{3} & -\frac{2}{3} & \frac{4}{3} & 0 & 0 & 0 \\ 0 & 0 & 0 & 1 & 0 & 0 \\ 0 & 0 & 0 & 0 & 1 & 0 \\ 0 & 0 & 0 & 0 & 0 & 1 \end{bmatrix} \begin{bmatrix} \varepsilon_1 \\ \varepsilon_2 \\ \varepsilon_3 \\ \varepsilon_4 \\ \varepsilon_5 \\ \varepsilon_6 \end{bmatrix} - C_G \begin{bmatrix} \varepsilon_1^A \\ \varepsilon_2^A \\ \varepsilon_3^A \\ \varepsilon_4^A \\ \varepsilon_5^A \\ \varepsilon_6^A \end{bmatrix}; \end{aligned} \quad (2.24)$$

By using the plane stress assumptions and simplifying Equation (2.24), a new relationship between the anelastic stresses and elastic strains is obtained, similar to Equation (2.11)

$$\begin{aligned}
\begin{bmatrix} \sigma_1^A \\ \sigma_2^A \\ \sigma_3^A \\ \sigma_6^A \end{bmatrix} &= \beta_K \begin{bmatrix} 1 & 1 & 1 & 0 \\ 1 & 1 & 1 & 0 \\ 1 & 1 & 1 & 0 \\ 0 & 0 & 0 & 0 \end{bmatrix} \left\{ \begin{bmatrix} \epsilon_1 \\ \epsilon_2 \\ \epsilon_3 \\ \epsilon_6 \end{bmatrix} \right\} - C_K \left\{ \begin{bmatrix} \epsilon_1^A \\ \epsilon_2^A \\ \epsilon_3^A \\ \epsilon_6^A \end{bmatrix} \right\} + \dots \\
\beta_G \begin{bmatrix} \frac{4}{3} & -\frac{2}{3} & -\frac{2}{3} & 0 \\ -\frac{2}{3} & \frac{4}{3} & -\frac{2}{3} & 0 \\ -\frac{2}{3} & -\frac{2}{3} & \frac{4}{3} & 0 \\ 0 & 0 & 0 & 1 \end{bmatrix} &\left\{ \begin{bmatrix} \epsilon_1 \\ \epsilon_2 \\ \epsilon_3 \\ \epsilon_6 \end{bmatrix} \right\} - C_G \left\{ \begin{bmatrix} \epsilon_1^A \\ \epsilon_2^A \\ \epsilon_3^A \\ \epsilon_6^A \end{bmatrix} \right\}
\end{aligned} \tag{2.25}$$

The anelastic stress in the Z Cartesian direction is assumed to be zero, and an additional relationship between the strains  $\epsilon_3$  and  $\epsilon_3^A$  in terms of the strains in the X and Y Cartesian orthogonal directions may be found. First, let

$$\begin{aligned}
E_1^A &= \beta_K C_K + \frac{4}{3} \beta_G C_G \\
E_2^A &= \beta_K C_K - \frac{2}{3} \beta_G C_G \\
E_3^A &= \beta_G C_G
\end{aligned} \tag{2.26}$$

Then

$$\begin{aligned}
\sigma_3^A &= \left( \beta_K + \frac{4}{3} \beta_G \right) \epsilon_3 + \left( \beta_K - \frac{2}{3} \beta_G \right) \epsilon_1 + \left( \beta_K - \frac{2}{3} \beta_G \right) \epsilon_2 - \dots \\
&\left( \beta_K C_K + \frac{4}{3} \beta_G C_G \right) \epsilon_3^A - \left( \beta_K C_K - \frac{2}{3} \beta_G C_G \right) \epsilon_1^A - \dots \\
&\left( \beta_K C_K - \frac{2}{3} \beta_G C_G \right) \epsilon_2^A = 0 \Leftrightarrow \dots \\
E_1 \epsilon_3 - E_1^A \epsilon_3^A &= -E_2 (\epsilon_2 + \epsilon_1) + E_2^A (\epsilon_1^A + \epsilon_2^A)
\end{aligned} \tag{2.27}$$

From Equations (2.13), (2.26) and (2.27), the strains  $\epsilon_3$  and  $\epsilon_3^A$  are found to be

$$\epsilon_3 = -\frac{E_2}{E_1}(\epsilon_2 + \epsilon_1) + (\epsilon_1^A + \epsilon_2^A) \left( \frac{E_1^A E_2 - E_1 E_2^A}{E_1(E_1^A - E_1)} \right) = \dots \quad (2.28)$$

$$= -\frac{E_2}{E_1} \left( \frac{\partial v}{\partial y} + \frac{\partial u}{\partial x} \right) + \left( \frac{\partial v^A}{\partial y} + \frac{\partial u^A}{\partial x} \right) \left( \frac{E_1^A E_2 - E_1 E_2^A}{E_1(E_1^A - E_1)} \right)$$

$$\epsilon_3^A = \frac{(E_2 - E_2^A)}{(E_1^A - E_1)} (\epsilon_1^A + \epsilon_2^A) = \frac{(E_2 - E_2^A)}{(E_1^A - E_1)} \left( \frac{\partial u^A}{\partial x} + \frac{\partial v^A}{\partial y} \right) \quad (2.28b)$$

The term  $E_2 \epsilon_3 - E_2^A \epsilon_3^A$  appears in the  $\sigma_1^A$  and  $\sigma_2^A$  stress-strain equations. This term may be developed using the expressions for strains  $\epsilon_3$  and  $\epsilon_3^A$

$$\begin{aligned} E_2 \epsilon_3 - E_2^A \epsilon_3^A &= \dots \\ &= -\frac{(E_2)^2}{E_1}(\epsilon_2 + \epsilon_1) + (\epsilon_1^A + \epsilon_2^A) \left( \frac{-E_1^A E_2^2 - E_1 (E_2^A)^2 + 2E_2^A E_1 E_2}{E_1(-E_1^A + E_1)} \right) = \dots \quad (2.29) \\ &= (\epsilon_2 + \epsilon_1)\vartheta + (\epsilon_1^A + \epsilon_2^A)\lambda \end{aligned}$$

where

$$\vartheta = -\frac{(E_2)^2}{E_1} \quad (2.30)$$

$$\lambda = \left( \frac{-E_1^A E_2^2 - E_1 (E_2^A)^2 + 2E_2^A E_1 E_2}{E_1 (-E_1^A + E_1)} \right)$$

As a result of these simplifications, the stress matrix expressed as a function of only the  $\varepsilon_1, \varepsilon_2, \varepsilon_6$  strains is

$$\begin{bmatrix} \sigma_1 \\ \sigma_2 \\ \sigma_6 \\ \sigma_1^A \\ \sigma_2^A \\ \sigma_6^A \end{bmatrix} = \begin{bmatrix} E_1 + \vartheta & E_2 + \vartheta & 0 & -(E_1 + \vartheta) & -(E_2 + \vartheta) & 0 \\ E_2 + \vartheta & E_1 + \vartheta & 0 & -(E_2 + \vartheta) & -(E_1 + \vartheta) & 0 \\ 0 & 0 & E_3 & 0 & 0 & -E_3 \\ E_1 + \vartheta & E_2 + \vartheta & 0 & -(E_1^A - \lambda) & -(E_2^A - \lambda) & 0 \\ E_2 + \vartheta & E_1 + \vartheta & 0 & -(E_2^A - \lambda) & -(E_1^A - \lambda) & 0 \\ 0 & 0 & E_3 & 0 & 0 & -E_3^A \end{bmatrix} \begin{bmatrix} \varepsilon_1 \\ \varepsilon_2 \\ \varepsilon_6 \\ \varepsilon_1^A \\ \varepsilon_2^A \\ \varepsilon_6^A \end{bmatrix} \quad (2.31)$$

By grouping the total stresses and anelastic stresses in the vectors  $\{\sigma\}$  and  $\{\sigma^A\}$ , respectively, and all the total strains and anelastic stresses in the vectors  $\{\varepsilon\}$  and  $\{\varepsilon^A\}$ , Equation (2.31) which can be condensed further to

$$\begin{Bmatrix} \{\sigma\} \\ \{\sigma^A\} \end{Bmatrix} = \begin{bmatrix} [D_1] & -[D_1] \\ [D_1] & -[D_1^A] \end{bmatrix} \begin{Bmatrix} \{\varepsilon\} \\ \{\varepsilon^A\} \end{Bmatrix} \quad (2.32)$$

where matrices  $[D_1]$  and  $[D_1^A]$  are, respectively

$$[D_1] = \begin{bmatrix} E_1 + \vartheta & E_2 + \vartheta & 0 \\ E_2 + \vartheta & E_1 + \vartheta & 0 \\ 0 & 0 & E_3 \end{bmatrix} \quad (2.33)$$

$$[D_1^A] = \begin{bmatrix} (E_1^A - \lambda) & (E_2^A - \lambda) & 0 \\ (E_2^A - \lambda) & (E_1^A - \lambda) & 0 \\ 0 & 0 & E_3^A \end{bmatrix} \quad (2.34)$$

### 2.1.2. Governing Equations

The governing equations of a viscoelastic structure modeled with ADF are represented by

- equations of motion describing the motion of the viscoelastic material particles as a function of the total displacement field; and
- relaxation equations describing the time history of the anelastic displacement field.

Together with the boundary conditions, the governing equations completely describe the frequency and time dependent behavior of the viscoelastic material.

#### 2.1.2.1. Equations of motion

The tensor form of the equation of motion for a material of density  $\rho$ , acted upon by a body force  $f_i$ , in Cartesian direction  $i$  ( $i=1,2,3$ ) is [28]

$$\rho u_{i,tt} - \sigma_{ij,j} = f_i \quad (2.35)$$

The stress may now be expressed in terms of the total and anelastic strains; Equation (2.35) now becomes [33]

$$\rho u_{i,tt} - \left( E_{ijkl} \left( \epsilon_{kl} - \epsilon_{kl}^A \right) \right)_{,j} = f_i \quad (2.36)$$



For the plane stress case, Equation (2.35), in terms of the total displacement  $u$  and  $v$  and stresses is

$$\begin{aligned}\rho \ddot{u} - \frac{\partial \sigma_{11}}{\partial x} - \frac{\partial \sigma_{12}}{\partial y} &= f_x \\ \rho \ddot{v} - \frac{\partial \sigma_{21}}{\partial x} - \frac{\partial \sigma_{22}}{\partial y} &= f_y\end{aligned}\tag{2.37}$$

The stresses are expressed in terms of the total and anelastic displacements

$$\begin{aligned}\rho \frac{\partial^2 u}{\partial t^2} - (E_1 + \nu) \left( \frac{\partial^2 u}{\partial x^2} \right) - (E_2 + \nu) \left( \frac{\partial^2 v}{\partial x \partial y} \right) - E_3 \left( \frac{\partial^2 v}{\partial x \partial y} + \frac{\partial^2 u}{\partial y^2} \right) + \dots \\ (E_1 + \nu) \left( \frac{\partial^2 u^A}{\partial x^2} \right) + (E_2 + \nu) \left( \frac{\partial^2 v^A}{\partial x \partial y} \right) + E_3 \left( \frac{\partial^2 v^A}{\partial x \partial y} + \frac{\partial^2 u^A}{\partial y^2} \right) &= f_x \\ \rho \frac{\partial^2 v}{\partial t^2} - (E_1 + \nu) \left( \frac{\partial^2 v}{\partial y^2} \right) - (E_2 + \nu) \left( \frac{\partial^2 u}{\partial x \partial y} \right) - E_3 \left( \frac{\partial^2 u}{\partial x \partial y} + \frac{\partial^2 v}{\partial x^2} \right) + \dots \\ (E_1 + \nu) \left( \frac{\partial^2 v^A}{\partial y^2} \right) + (E_2 + \nu) \left( \frac{\partial^2 u^A}{\partial x \partial y} \right) + E_3 \left( \frac{\partial^2 u^A}{\partial x \partial y} + \frac{\partial^2 v^A}{\partial x^2} \right) &= f_y\end{aligned}\tag{2.38}$$

### 2.1.2.2. Relaxation equations

The relaxation equations may be obtained from a nonequilibrium thermodynamics assumption, which states that the time rate of change of the state variable is proportional to the conjugate quantity. Here, the preceding assumption means that the rate of change of the anelastic strain is proportional to the anelastic stress [33]

$$\varepsilon_{kl,t}^A = L_{klij} \sigma_{ij}^A \quad (2.39)$$

In what follows, a single anelastic displacement field (ADF) is considered. The rate of change of the anelastic strain is proportional to the difference between its equilibrium and actual value ( $\bar{\varepsilon}^A$ )

$$\varepsilon_{kl,t}^A = -\Omega \left( \varepsilon_{kl}^A - \bar{\varepsilon}_{kl}^A \right) \quad (2.40)$$

where  $\Omega$  is the inverse of the relaxation time at constant strain.

The equilibrium value of the anelastic strain  $\bar{\varepsilon}^A$  corresponds to a null anelastic stress

$$\bar{\varepsilon}^A = \left( E_{ijkl}^A \right)^{-1} E_{ijkl} \varepsilon_{kl} \quad (2.41)$$

The time rate of change of the anelastic strain becomes

$$E_{ijkl}^A \varepsilon_{kl,t}^A = -\Omega \left( E_{ijkl}^A \varepsilon_{kl}^A - E_{ijkl} \varepsilon_{kl} \right) \quad (2.42)$$

or, extracting the anelastic stress, [33]

$$\frac{1}{\Omega} E_{ijkl}^A \varepsilon_{kl,t}^A = E_{ijkl} \varepsilon_{kl} - E_{ijkl}^A \varepsilon_{kl}^A = \sigma_{ij}^A \quad (2.43)$$

The divergence of Equation (2.43) is

$$\left( \frac{1}{\Omega} E_{ijkl}^A \varepsilon_{kl,t}^A \right)_{,j} - \sigma_{ij,j}^A = 0 \quad (2.44)$$

Equation (2.44) may be developed in terms of the strains, Reference [33] as

$$\left( \frac{1}{\Omega} E_{ijkl}^A \varepsilon_{kl,t}^A - E_{ijkl} \varepsilon_{kl} + E_{ijkl}^A \varepsilon_{kl}^A \right)_{,j} = 0 \quad (2.45)$$

Equation (2.45) shows the coupling between the elastic and anelastic fields. For the plane stress case, Equation (2.45) becomes, after taking into account Equation (2.31),

$$\begin{aligned} & \frac{(E_1^A - \lambda)}{\Omega} \frac{\partial}{\partial t} \left( \frac{\partial^2 u^A}{\partial x^2} \right) + \frac{(E_2^A - \lambda)}{\Omega} \frac{\partial}{\partial t} \left( \frac{\partial^2 v^A}{\partial x \partial y} \right) + \frac{E_3^A}{\Omega} \frac{\partial}{\partial t} \left( \frac{\partial^2 u^A}{\partial y^2} + \frac{\partial^2 v^A}{\partial x \partial y} \right) - \dots \\ & (E_1 + \nu) \left( \frac{\partial^2 u}{\partial x^2} \right) - (E_2 + \nu) \left( \frac{\partial^2 v}{\partial x \partial y} \right) - E_3 \left( \frac{\partial^2 u}{\partial y^2} + \frac{\partial^2 v}{\partial x \partial y} \right) + \dots \\ & (E_1^A - \lambda) \left( \frac{\partial^2 u^A}{\partial x^2} \right) + (E_2^A - \lambda) \left( \frac{\partial^2 v^A}{\partial x \partial y} \right) + E_3^A \left( \frac{\partial^2 u^A}{\partial y^2} + \frac{\partial^2 v^A}{\partial x \partial y} \right) = 0 \end{aligned} \quad (2.46a)$$

and

$$\begin{aligned} & \frac{(E_1^A - \lambda)}{\Omega} \frac{\partial}{\partial t} \left( \frac{\partial^2 v^A}{\partial y^2} \right) + \frac{(E_2^A - \lambda)}{\Omega} \frac{\partial}{\partial t} \left( \frac{\partial^2 u^A}{\partial x \partial y} \right) + \frac{E_3^A}{\Omega} \frac{\partial}{\partial t} \left( \frac{\partial^2 v^A}{\partial x^2} + \frac{\partial^2 u^A}{\partial x \partial y} \right) - \dots \\ & (E_1 + \nu) \left( \frac{\partial^2 v}{\partial y^2} \right) - (E_2 + \nu) \left( \frac{\partial^2 u}{\partial x \partial y} \right) - E_3 \left( \frac{\partial^2 v}{\partial x^2} + \frac{\partial^2 u}{\partial x \partial y} \right) + \dots \\ & (E_1^A - \lambda) \left( \frac{\partial^2 v^A}{\partial y^2} \right) + (E_2^A - \lambda) \left( \frac{\partial^2 u^A}{\partial x \partial y} \right) + E_3^A \left( \frac{\partial^2 v^A}{\partial x^2} + \frac{\partial^2 u^A}{\partial x \partial y} \right) = 0 \end{aligned} \quad (2.46b)$$

### 2.1.3. Model development

In what follows, the elemental stiffness, mass and damping matrices for the plane stress, single-ADF, triangular, finite element are developed.

A single ADF, plane-stress, triangular finite element, is now defined. Each node has two degrees of freedom:  $u$ , displacement in the horizontal  $X$  direction, and  $v$ , displacement in the vertical  $Y$  direction. The element thickness is  $t$  and  $\Delta$  is the element area, as shown in Figure 2.1. The displacements are approximated using the following shape functions at each node (denoted by subscripts  $i, j$  and  $m$ , respectively) of the triangular finite element

$$N_i(x, y) = \frac{a_i + b_i x + c_i y}{2\Delta} \quad \text{and} \quad [N_1(x, y)] = [N_i \ N_j \ N_m] \quad (2.47)$$

where

$$\begin{aligned} a_i &= x_j y_m - x_m y_j \\ b_i &= y_j - y_m = y_{jm} \\ c_i &= x_m - x_j = x_{mj} \end{aligned} \quad (2.48)$$

The shape functions  $N_j$  and  $N_m$  are obtained similarly to  $N_i$ . In terms of the shape function, the total and anelastic displacements of the finite element are, respectively

$$u(x, y, t) = [u(x, y)]\{U(t)\} = [N_1(x, y)]\{U(t)\} = \begin{bmatrix} N_i \\ N_j \\ N_m \end{bmatrix}^T \begin{Bmatrix} u_i \\ u_j \\ u_m \end{Bmatrix} \quad (2.49a)$$

$$v(x, t) = [v(x, y)]\{V(t)\} = [N_1(x, y)]\{V(t)\} = \begin{bmatrix} N_i \\ N_j \\ N_m \end{bmatrix}^T \begin{Bmatrix} v_i \\ v_j \\ v_m \end{Bmatrix}$$

$$u^A(x, y, t) = [u^A(x, y)] \{U^A(t)\} = [N_1(x, y)] \{U^A(t)\} = \begin{bmatrix} N_i \\ N_j \\ N_m \end{bmatrix}^T \begin{Bmatrix} u_i^A \\ u_j^A \\ u_m^A \end{Bmatrix} \quad (2.49)$$

$$v^A(x, y, t) = [v^A(x, y)] \{V^A(t)\} = [N_1(x, y)] \{V^A(t)\} = \begin{bmatrix} N_i \\ N_j \\ N_m \end{bmatrix}^T \begin{Bmatrix} v_i^A \\ v_j^A \\ v_m^A \end{Bmatrix}$$

The total and anelastic displacements are as a function of the shape function matrix [N]

$$\begin{Bmatrix} u \\ v \\ u^A \\ v^A \end{Bmatrix} = [N] \begin{Bmatrix} u_i \\ u_j \\ u_m \\ v_i \\ v_j \\ v_m \\ u_i^A \\ u_j^A \\ u_m^A \\ v_i^A \\ v_j^A \\ v_m^A \end{Bmatrix} = [N] \begin{Bmatrix} \{\delta(t)\} \\ \{\delta^A(t)\} \end{Bmatrix} \quad (2.50)$$

where the matrix [N] is

$$[N] = \begin{bmatrix} [N_1] & 0 & 0 & 0 \\ 0 & [N_1] & 0 & 0 \\ 0 & 0 & [N_1] & 0 \\ 0 & 0 & 0 & [N_1] \end{bmatrix}_{4 \times 12} \quad (2.51)$$

and where  $\{\delta\}$  and  $\{\delta^A\}$  are the total and anelastic time dependent parameter coordinates, respectively

$$\{\delta(t)\} = \begin{bmatrix} u_i \\ u_j \\ u_m \\ v_i \\ v_j \\ v_m \end{bmatrix}; \quad \{\delta^A(t)\} = \begin{bmatrix} u_i^A \\ u_j^A \\ u_m^A \\ v_i^A \\ v_j^A \\ v_m^A \end{bmatrix} \quad (2.52)$$

If the shape functions are substituted, the strain matrix as a function of the displacements is obtained

$$\begin{Bmatrix} \{\epsilon\} \\ \{\epsilon^A\} \end{Bmatrix} = [B] \begin{Bmatrix} \{\delta(t)\} \\ \{\delta^A(t)\} \end{Bmatrix} \quad (2.53)$$

and the matrix  $[B]$  is

$$[B] = \frac{1}{2\Delta} \begin{bmatrix} b_i & b_j & b_m & 0 & 0 & 0 & 0 & 0 & 0 & 0 & 0 & 0 \\ 0 & 0 & 0 & c_i & c_j & c_m & 0 & 0 & 0 & 0 & 0 & 0 \\ c_i & c_j & c_m & b_i & b_j & b_m & 0 & 0 & 0 & 0 & 0 & 0 \\ 0 & 0 & 0 & 0 & 0 & 0 & b_i & b_j & b_m & 0 & 0 & 0 \\ 0 & 0 & 0 & 0 & 0 & 0 & 0 & 0 & 0 & c_i & c_j & c_m \\ 0 & 0 & 0 & 0 & 0 & 0 & c_i & c_j & c_m & b_i & b_j & b_m \end{bmatrix} \quad (2.54)$$

where

$$\frac{\partial N_i}{\partial x} = b_i \quad ; \quad \frac{\partial N_j}{\partial y} = c_j. \quad (2.55)$$

In detailed matrix form, Equation (2.53) is expressed as

$$\left\{ \begin{Bmatrix} \epsilon \end{Bmatrix} \right\} = \frac{1}{2\Delta} \begin{bmatrix} b_i & b_j & b_m & 0 & 0 & 0 & 0 & 0 & 0 & 0 & 0 & 0 \\ 0 & 0 & 0 & c_i & c_j & c_m & 0 & 0 & 0 & 0 & 0 & 0 \\ c_i & c_j & c_m & b_i & b_j & b_m & 0 & 0 & 0 & 0 & 0 & 0 \\ 0 & 0 & 0 & 0 & 0 & 0 & b_i & b_j & b_m & 0 & 0 & 0 \\ 0 & 0 & 0 & 0 & 0 & 0 & 0 & 0 & 0 & c_i & c_j & c_m \\ 0 & 0 & 0 & 0 & 0 & 0 & c_i & c_j & c_m & b_i & b_j & b_m \end{bmatrix} \begin{bmatrix} u_i \\ u_j \\ u_m \\ v_i \\ v_j \\ v_m \\ u_i^A \\ u_j^A \\ u_m^A \\ u_j^A \\ v_i^A \\ v_j^A \\ v_m^A \end{bmatrix} \quad (2.56)$$

The elemental mass matrix [m] is obtained from the expression of the kinetic energy, as follows [33]

$$T(x, y, t) = \frac{1}{2} \rho \int_V \left[ \begin{Bmatrix} \dot{u} \\ \dot{v} \end{Bmatrix}^T \begin{Bmatrix} \dot{u} \\ \dot{v} \end{Bmatrix} \right] dV = \dots \quad (2.57)$$

$$= \frac{1}{2} \rho \int_V \left\{ \begin{Bmatrix} \dot{\delta} \\ 0 \end{Bmatrix} \right\}^T \begin{bmatrix} [N_1] & 0 & 0 & 0 \\ 0 & [N_1] & 0 & 0 \\ 0 & 0 & 0 & 0 \\ 0 & 0 & 0 & 0 \end{bmatrix} \begin{bmatrix} [N_1] & 0 & 0 & 0 \\ 0 & [N_1] & 0 & 0 \\ 0 & 0 & 0 & 0 \\ 0 & 0 & 0 & 0 \end{bmatrix} \left\{ \begin{Bmatrix} \dot{\delta} \\ 0 \end{Bmatrix} \right\} dV = \dots \quad (2.57 \text{ cont.})$$

$$= \frac{1}{2} [m] \left\{ \begin{Bmatrix} \dot{\delta} \\ 0 \end{Bmatrix} \right\}^T \left\{ \begin{Bmatrix} \dot{\delta} \\ 0 \end{Bmatrix} \right\}$$

Finally, the mass matrix may be written in the following form, if the thickness is constant over the element

$$[m] = \rho t \iint \begin{bmatrix} [M_1]_{3 \times 3} & \{0\}_{3 \times 3} & \{0\}_{3 \times 3} & \{0\}_{3 \times 3} \\ \{0\}_{3 \times 3} & [M_1]_{3 \times 3} & \{0\}_{3 \times 3} & \{0\}_{3 \times 3} \\ \{0\}_{3 \times 3} & \{0\}_{3 \times 3} & \{0\}_{3 \times 3} & \{0\}_{3 \times 3} \\ \{0\}_{3 \times 3} & \{0\}_{3 \times 3} & \{0\}_{3 \times 3} & \{0\}_{3 \times 3} \end{bmatrix}_{12 \times 12} dx dy = \dots \quad (2.58)$$

$$= \rho t \iint \begin{bmatrix} [M_1]_{3 \times 3} & \{0\}_{3 \times 3} & \{0\}_{3 \times 3} & \{0\}_{3 \times 3} \\ \{0\}_{3 \times 3} & [M_1]_{3 \times 3} & \{0\}_{3 \times 3} & \{0\}_{3 \times 3} \\ \{0\}_{3 \times 3} & \{0\}_{3 \times 3} & \{0\}_{3 \times 3} & \{0\}_{3 \times 3} \\ \{0\}_{3 \times 3} & \{0\}_{3 \times 3} & \{0\}_{3 \times 3} & \{0\}_{3 \times 3} \end{bmatrix} dx dy$$

where

$$[M_1] = \begin{bmatrix} (N_i)^2 & N_i N_j & N_i N_m \\ N_i N_j & (N_j)^2 & N_m N_j \\ N_i N_m & N_m N_j & (N_m)^2 \end{bmatrix} \quad (2.59)$$

Note that



$$\iint N_i N_j dx dy = \begin{cases} \frac{1}{12} \Delta, & i \neq j \\ \frac{1}{6} \Delta, & i = j \end{cases} \quad (2.60)$$

The elemental stiffness matrix  $[k]$  can be extracted from the strain energy expression [20]. The strain energy is shown in Equation (2.61) and the stiffness matrix in Equation (2.62) [33]

$$U_s = \frac{1}{2} \int_V \left\{ \begin{Bmatrix} \{\epsilon\} \\ \{\epsilon^A\} \end{Bmatrix} \right\}^T \begin{bmatrix} [D_1] & [-D_1] \\ [-D_1] & [D_1^A] \end{bmatrix} \left\{ \begin{Bmatrix} \{\epsilon\} \\ \{\epsilon^A\} \end{Bmatrix} \right\} dV = \dots \quad (2.61)$$

$$\frac{1}{2} \int_V \left\{ \begin{Bmatrix} \{\delta\} \\ \{\delta^A\} \end{Bmatrix} \right\}^T B^T \begin{bmatrix} [D_1] & [-D_1] \\ [-D_1] & [D_1^A] \end{bmatrix} B \left\{ \begin{Bmatrix} \{\delta\} \\ \{\delta^A\} \end{Bmatrix} \right\} dV$$

$$[k] = \int_V B^T \begin{bmatrix} [D_1] & [-D_1] \\ [D_1] & [D_1^A] \end{bmatrix} B dV = \iint B^T \begin{bmatrix} [D_1] & [-D_1] \\ [-D_1] & [D_1^A] \end{bmatrix} B t dx dy = \dots \quad (2.62)$$

$$= \begin{bmatrix} [K_1] & [-K_1] \\ [-K_1] & [K_1^A] \end{bmatrix}_{12 \times 12}$$

If the thickness of the element is constant, Equation (2.62) becomes

$$[k] = B^T \begin{bmatrix} [D_1] & [-D_1] \\ [-D_1] & [D_1^A] \end{bmatrix} B t \Delta = \begin{bmatrix} [K_1]_{6 \times 6} & -[K_1]_{6 \times 6} \\ -[K_1]_{6 \times 6} & [K_1^A]_{6 \times 6} \end{bmatrix}_{12 \times 12} \quad (2.63)$$

The damping matrix may be extracted similarly from the first term of the equation for virtual work (Equation (2.46) and [33])

$$\begin{aligned} \delta W(x, y, t) = \int_V -\frac{1}{\Omega} \left\{ \begin{matrix} \{0\} \\ \dot{\epsilon}^A \end{matrix} \right\}^T \begin{bmatrix} 0 & 0 \\ 0 & D_1^A \end{bmatrix} \delta \left\{ \begin{matrix} \{0\} \\ \dot{\epsilon}^A \end{matrix} \right\} dV + \{\sigma\} \delta \{u\}_0^V + \dots \\ + \int_V \{f\} \delta \{u\} dV \end{aligned} \quad (2.64)$$

where  $\{f\}$  is the distributed force vector. The damping matrix  $[c]$  is

$$[c] = \frac{1}{\Omega} \int_V B^T \begin{bmatrix} 0 & 0 \\ 0 & D_1^A \end{bmatrix} B dV = \frac{1}{\Omega} \iint B^T \begin{bmatrix} 0 & 0 \\ 0 & D_1^A \end{bmatrix} B t dx dy \quad (2.65)$$

If the thickness  $t$  is constant across the element, the damping matrix becomes

$$[c] = \frac{1}{\Omega} B^T \begin{bmatrix} 0 & 0 \\ 0 & D_1^A \end{bmatrix} B t \Delta = \frac{1}{\Omega} \begin{bmatrix} [0]_{6 \times 6} & [0]_{6 \times 6} \\ [0]_{6 \times 6} & [K_1^A]_{6 \times 6} \end{bmatrix}_{12 \times 12} \quad (2.66)$$

## 2.2. Development of the axisymmetric triangular ADF finite element

In the current work, an axisymmetric triangular element is developed to address modeling of more complex viscoelastic structures, such as viscoelastic O-rings.

### 2.2.1. Assumptions and stress-strain equations

According to the theory of elasticity, the following hypotheses are advanced for the axisymmetric case [20]

$$\begin{aligned}
&\sigma_r (= \sigma_1), \sigma_\theta (= \sigma_2), \sigma_z (= \sigma_3), \tau_{rz} (= \sigma_5) \neq 0 \\
&\varepsilon_r \left( = \varepsilon_1 = \frac{\partial u}{\partial r} \right), \varepsilon_\theta \left( = \varepsilon_2 = \frac{u}{r} \right), \varepsilon_z \left( = \varepsilon_3 = \frac{\partial v}{\partial z} \right), \gamma_{rz} \left( = \varepsilon_5 = \frac{\partial v}{\partial z} + \frac{\partial v}{\partial r} \right) \neq 0 \quad (2.67) \\
&\tau_{r\theta} (= \sigma_6) = \tau_{z\theta} (= \sigma_4) = 0
\end{aligned}$$

where  $u$  is the displacement in the radial direction  $r$  and  $v$  is the displacement in the vertical direction  $z$ .

The shear stresses in the circumferential polar direction  $\theta$  are null. Note that any radial strain induces a circumferential strain ( $\varepsilon_2$ ). The coordinate system and the axisymmetric finite element are shown in Figure 2.2.

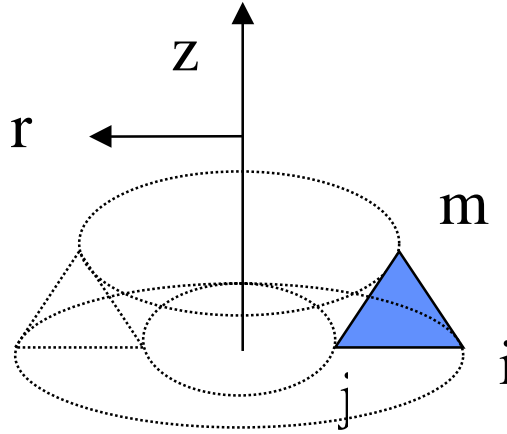


Figure 2.2. Axisymmetric finite element

### 2.2.2. Governing equations

The ADF constitutive equations for the axisymmetric case may be developed in a manner similar to that used in the plane stress case (see Section 2.1.2) and are

$$\begin{bmatrix} \sigma_1 \\ \sigma_2 \\ \sigma_3 \\ \sigma_5 \end{bmatrix} = \beta_K \begin{bmatrix} 1 & 1 & 1 & 0 \\ 1 & 1 & 1 & 0 \\ 1 & 1 & 1 & 0 \\ 0 & 0 & 0 & 0 \end{bmatrix} \begin{Bmatrix} \varepsilon_1 - \varepsilon_1^A \\ \varepsilon_2 - \varepsilon_2^A \\ \varepsilon_3 - \varepsilon_3^A \\ \varepsilon_5 - \varepsilon_5^A \end{Bmatrix} + \beta_G \begin{bmatrix} \frac{4}{3} & -\frac{2}{3} & -\frac{2}{3} & 0 \\ -\frac{2}{3} & \frac{4}{3} & -\frac{2}{3} & 0 \\ -\frac{2}{3} & -\frac{2}{3} & \frac{4}{3} & 0 \\ 0 & 0 & 0 & 1 \end{bmatrix} \begin{Bmatrix} \varepsilon_1 - \varepsilon_1^A \\ \varepsilon_2 - \varepsilon_2^A \\ \varepsilon_3 - \varepsilon_3^A \\ \varepsilon_5 - \varepsilon_5^A \end{Bmatrix} \quad (2.68)$$

where

$$E_1 = \beta_K + \frac{4}{3}\beta_G \quad (2.69)$$

$$E_2 = \beta_K - \frac{2}{3}\beta_G$$

(2.69 cont.)

$$E_3 = \beta_G$$

The anelastic stresses may also be obtained in the same way as in Section 2.1.2. The axisymmetric hypotheses also apply to the anelastic stresses and strains

$$\begin{aligned} & \sigma_r^A (= \sigma_1^A), \sigma_\theta^A (= \sigma_2^A), \sigma_z^A (= \sigma_3^A), \tau_{rz}^A (= \sigma_5^A) \neq 0 \\ & \varepsilon_r^A \left( = \varepsilon_1^A = \frac{\partial u^A}{\partial r} \right), \varepsilon_\theta^A \left( = \varepsilon_2^A = \frac{u^A}{r} \right), \\ & \varepsilon_z^A \left( = \varepsilon_3^A = \frac{\partial v^A}{\partial z} \right), \gamma_{rz}^A \left( = \varepsilon_5^A = \frac{\partial u^A}{\partial z} + \frac{\partial v^A}{\partial r} \right) \neq 0 \\ & \tau_{\theta z}^A (= \sigma_6^A) = \tau_{\theta r}^A (= \sigma_4^A) = 0 \end{aligned} \quad (2.70)$$

In a similar way to Section 2.1.2, the relationship between anelastic stresses and anelastic and total strains is obtained

$$\begin{aligned}
\begin{bmatrix} \sigma_1^A \\ \sigma_2^A \\ \sigma_3^A \\ \sigma_5^A \end{bmatrix} &= \beta_K \begin{bmatrix} 1 & 1 & 1 & 0 \\ 1 & 1 & 1 & 0 \\ 1 & 1 & 1 & 0 \\ 0 & 0 & 0 & 0 \end{bmatrix} \left\{ \begin{bmatrix} \varepsilon_1 \\ \varepsilon_2 \\ \varepsilon_3 \\ \varepsilon_5 \end{bmatrix} \right\} - C_K \left\{ \begin{bmatrix} \varepsilon_1^A \\ \varepsilon_2^A \\ \varepsilon_3^A \\ \varepsilon_5^A \end{bmatrix} \right\} + \dots \\
&+ \beta_G \begin{bmatrix} \frac{4}{3} & -\frac{2}{3} & -\frac{2}{3} & 0 \\ -\frac{2}{3} & \frac{4}{3} & -\frac{2}{3} & 0 \\ -\frac{2}{3} & -\frac{2}{3} & \frac{4}{3} & 0 \\ 0 & 0 & 0 & 1 \end{bmatrix} \left\{ \begin{bmatrix} \varepsilon_1 \\ \varepsilon_2 \\ \varepsilon_3 \\ \varepsilon_5 \end{bmatrix} \right\} - C_G \left\{ \begin{bmatrix} \varepsilon_1^A \\ \varepsilon_2^A \\ \varepsilon_3^A \\ \varepsilon_5^A \end{bmatrix} \right\}
\end{aligned} \tag{2.71}$$

First, let

$$\begin{aligned}
E_1^A &= \beta_K C_K + \frac{4}{3} \beta_G C_G \\
E_2^A &= \beta_K C_K - \frac{2}{3} \beta_G C_G \\
E_3^A &= \beta_G C_G
\end{aligned} \tag{2.72}$$

In matrix form, the stress-strain relationship becomes, expressed in complex matrix form

$$\left\{ \begin{bmatrix} \{\sigma\} \\ \{\sigma^A\} \end{bmatrix} \right\} = \begin{bmatrix} [D_1] & [-D_1] \\ [D_1] & [-D_1^A] \end{bmatrix} \left\{ \begin{bmatrix} \{\varepsilon\} \\ \{\varepsilon^A\} \end{bmatrix} \right\} \tag{2.73}$$

or in expanded matrix form

$$\begin{bmatrix} \sigma_1 \\ \sigma_2 \\ \sigma_3 \\ \sigma_5 \\ \sigma_1^A \\ \sigma_2^A \\ \sigma_3^A \\ \sigma_5^A \end{bmatrix} = \begin{bmatrix} E_1 & E_2 & E_2 & 0 & -E_1 & -E_2 & -E_2 & 0 \\ E_2 & E_1 & E_2 & 0 & -E_2 & -E_1 & -E_2 & 0 \\ E_2 & E_2 & E_1 & 0 & -E_2 & -E_2 & -E_1 & 0 \\ 0 & 0 & 0 & E_3 & 0 & 0 & 0 & -E_3 \\ E_1 & E_2 & E_2 & 0 & -E_1^A & -E_2^A & -E_2^A & 0 \\ E_2 & E_1 & E_2 & 0 & -E_2^A & -E_1^A & -E_2^A & 0 \\ E_2 & E_2 & E_1 & 0 & -E_2^A & -E_2^A & -E_1^A & 0 \\ 0 & 0 & 0 & E_3 & 0 & 0 & 0 & -E_3^A \end{bmatrix} \begin{bmatrix} \varepsilon_1 \\ \varepsilon_2 \\ \varepsilon_3 \\ \varepsilon_5 \\ \varepsilon_1^A \\ \varepsilon_2^A \\ \varepsilon_3^A \\ \varepsilon_5^A \end{bmatrix} \quad (2.74)$$

where the elastic and anelastic stress matrices are, respectively

$$\{\sigma\} = \begin{bmatrix} \sigma_1 \\ \sigma_2 \\ \sigma_3 \\ \sigma_5 \end{bmatrix}, \quad \{\sigma^A\} = \begin{bmatrix} \sigma_1^A \\ \sigma_2^A \\ \sigma_3^A \\ \sigma_5^A \end{bmatrix} \quad (2.75)$$

where matrix  $[D_1]$  is

$$[D_1] = \begin{bmatrix} E_1 & E_2 & E_2 & 0 \\ E_2 & E_1 & E_2 & 0 \\ E_2 & E_2 & E_1 & 0 \\ 0 & 0 & 0 & E_3 \end{bmatrix} \quad (2.76)$$

and matrix  $[D_1^A]$  is

$$[D_1^A] = \begin{bmatrix} E_1^A & E_2^A & E_2^A & 0 \\ E_2^A & E_1^A & E_2^A & 0 \\ E_2^A & E_2^A & E_1^A & 0 \\ 0 & 0 & 0 & E_3^A \end{bmatrix} \quad (2.77)$$

The strains in expanded matrix form are

$$\{\epsilon\} = \begin{Bmatrix} \epsilon_1 \\ \epsilon_2 \\ \epsilon_3 \\ \epsilon_5 \end{Bmatrix} = \begin{Bmatrix} \frac{\partial u}{\partial r} \\ \frac{u}{r} \\ \frac{\partial v}{\partial z} \\ \frac{\partial u}{\partial z} + \frac{\partial v}{\partial r} \end{Bmatrix}, \quad \{\epsilon^A\} = \begin{Bmatrix} \epsilon_1^A \\ \epsilon_2^A \\ \epsilon_3^A \\ \epsilon_5^A \end{Bmatrix} = \begin{Bmatrix} \frac{\partial u^A}{\partial r} \\ \frac{u^A}{r} \\ \frac{\partial v^A}{\partial z} \\ \frac{\partial u^A}{\partial z} + \frac{\partial v^A}{\partial r} \end{Bmatrix} \quad (2.78)$$

### 2.2.3. Model development

In what follows, the elemental stiffness, mass, and damping matrices for the axisymmetric, single ADF, triangular finite element are developed.

Each node has two degrees of freedom (DOF):  $u$ , displacement in the radial direction  $r$ ,  $v$ , displacement in the vertical direction  $z$ . The element area is denoted by  $\Delta$ . The displacements are approximated using the following shape functions at each node (denoted respectively by subscripts  $i$ ,  $j$  and  $m$ ) of the triangular finite element [20]

$$N_i(r, z) = \frac{a_i + b_i r + c_i z}{2\Delta} \quad \text{and} \quad [N_2(r, z)] = [N_i \ N_j \ N_m] \quad (2.79)$$

Thus, the total displacements and anelastic displacements of the finite element are, respectively

$$\begin{aligned}
u(r, z, t) &= [N_2(r, z)] \{U(t)\} = \begin{bmatrix} N_i \\ N_j \\ N_m \end{bmatrix}^T \begin{Bmatrix} u_i \\ u_j \\ u_m \end{Bmatrix} \\
v(r, z, t) &= [N_2(r, z)] \{V(t)\} = \begin{bmatrix} N_i \\ N_j \\ N_m \end{bmatrix}^T \begin{Bmatrix} v_i \\ v_j \\ v_m \end{Bmatrix} \\
u^A(r, z, t) &= [N_2(r, z)] \{U^A(t)\} = \begin{bmatrix} N_i \\ N_j \\ N_m \end{bmatrix}^T \begin{Bmatrix} u_i^A \\ u_j^A \\ u_m^A \end{Bmatrix} \\
v^A(r, z, t) &= [N_2(r, z)] \{V^A(t)\} = \begin{bmatrix} N_i \\ N_j \\ N_m \end{bmatrix}^T \begin{Bmatrix} v_i^A \\ v_j^A \\ v_m^A \end{Bmatrix}
\end{aligned} \tag{2.80}$$

Equation (2.80) can be condensed into Equation (2.81)



$$\begin{Bmatrix} u \\ v \\ u^A \\ v^A \end{Bmatrix} = [N] \begin{Bmatrix} u_i \\ u_j \\ u_m \\ v_i \\ v_j \\ v_m \\ u_i^A \\ u_j^A \\ u_m^A \\ v_i^A \\ v_j^A \\ v_m^A \end{Bmatrix} = [N] \begin{Bmatrix} \{\delta(t)\} \\ \{\delta^A(t)\} \end{Bmatrix} \quad (2.81)$$

Matrix  $[N]$  is

$$[N] = \begin{bmatrix} [N_2] & 0 & 0 & 0 \\ 0 & [N_2] & 0 & 0 \\ 0 & 0 & [N_2] & 0 \\ 0 & 0 & 0 & [N_2] \end{bmatrix}_{4 \times 12} \quad (2.82)$$

where  $\{\delta\}$  and  $\{\delta^A\}$  are the total and anelastic time dependent parameter vectors, respectively,

$$\{\delta(t)\} = \begin{bmatrix} u_i \\ u_j \\ u_m \\ v_i \\ v_j \\ v_m \end{bmatrix}; \quad \{\delta^A(t)\} = \begin{bmatrix} u_i^A \\ u_j^A \\ u_m^A \\ v_i^A \\ v_j^A \\ v_m^A \end{bmatrix} \quad (2.83)$$

By substituting the shape functions, the strain matrix is obtained as a function of the displacements

$$\left\{ \begin{Bmatrix} \{\epsilon\} \\ \{\epsilon^A\} \end{Bmatrix} \right\} = [B] \left\{ \begin{Bmatrix} \{\delta(t)\} \\ \{\delta^A(t)\} \end{Bmatrix} \right\} \quad (2.84)$$

where matrix [B] is

$$[B] = \frac{1}{2\Delta} \begin{bmatrix} b_i & b_j & b_m & 0 & 0 & 0 & 0 & 0 & 0 & 0 & 0 & 0 \\ d_i & d_j & d_m & 0 & 0 & 0 & 0 & 0 & 0 & 0 & 0 & 0 \\ 0 & 0 & 0 & c_i & c_j & c_m & 0 & 0 & 0 & 0 & 0 & 0 \\ c_i & c_j & c_m & b_i & b_j & b_m & 0 & 0 & 0 & 0 & 0 & 0 \\ 0 & 0 & 0 & 0 & 0 & 0 & b_i & b_j & b_m & 0 & 0 & 0 \\ 0 & 0 & 0 & 0 & 0 & 0 & d_i & d_j & d_m & 0 & 0 & 0 \\ 0 & 0 & 0 & 0 & 0 & 0 & 0 & 0 & 0 & c_i & c_j & c_m \\ 0 & 0 & 0 & 0 & 0 & 0 & c_i & c_j & c_m & b_i & b_j & b_m \end{bmatrix} \quad (2.85)$$

and

$$\frac{\partial N_i}{\partial r} = \frac{b_i}{2\Delta} ; \quad \frac{\partial N_i}{\partial z} = \frac{c_i}{2\Delta} ; \quad \frac{N_i}{r} = \frac{d_i}{2\Delta} \quad (2.86)$$

In more detailed form, Equation (2.85) becomes

$$\left\{ \begin{Bmatrix} \{\epsilon\} \\ \{\epsilon^A\} \end{Bmatrix} \right\} = \frac{1}{2\Delta} \begin{bmatrix} b_i & b_j & b_m & 0 & 0 & 0 & 0 & 0 & 0 & 0 & 0 & 0 \\ d_i & d_j & d_m & 0 & 0 & 0 & 0 & 0 & 0 & 0 & 0 & 0 \\ 0 & 0 & 0 & c_i & c_j & c_m & 0 & 0 & 0 & 0 & 0 & 0 \\ c_i & c_j & c_m & b_i & b_j & b_m & 0 & 0 & 0 & 0 & 0 & 0 \\ 0 & 0 & 0 & 0 & 0 & 0 & b_i & b_j & b_m & 0 & 0 & 0 \\ 0 & 0 & 0 & 0 & 0 & 0 & d_i & d_j & d_m & 0 & 0 & 0 \\ 0 & 0 & 0 & 0 & 0 & 0 & 0 & 0 & 0 & c_i & c_j & c_m \\ 0 & 0 & 0 & 0 & 0 & 0 & c_i & c_j & c_m & b_i & b_j & b_m \end{bmatrix} \begin{bmatrix} u_i \\ u_j \\ u_m \\ v_i \\ v_j \\ v_m \\ u_i^A \\ u_j^A \\ u_m^A \\ v_i^A \\ v_j^A \\ v_m^A \end{bmatrix} \quad (2.87)$$

For an axisymmetric three node triangular finite element with one ADF, the elastic strain energy is given by Equation (2.88)

$$\begin{aligned} U_s &= \frac{1}{2} \int_V \left\{ \begin{Bmatrix} \{\epsilon\} \\ \{\epsilon^A\} \end{Bmatrix} \right\}^T \begin{bmatrix} [D_1] & [-D_1] \\ [-D_1] & [D_1^A] \end{bmatrix} \left\{ \begin{Bmatrix} \{\epsilon\} \\ \{\epsilon^A\} \end{Bmatrix} \right\} dV = \dots \\ &= \frac{1}{2} \int_V \left\{ \begin{Bmatrix} \{\delta\} \\ \{\delta^A\} \end{Bmatrix} \right\}^T [B]^T \begin{bmatrix} [D_1] & [-D_1] \\ [-D_1] & [D_1^A] \end{bmatrix} [B] \left\{ \begin{Bmatrix} \{\delta\} \\ \{\delta^A\} \end{Bmatrix} \right\} dV \end{aligned} \quad (2.88)$$

After integrating over the volume, the element stiffness matrix becomes

$$[k] = 2\pi \int [B]^T \begin{bmatrix} [D_1] & [-D_1] \\ [-D_1] & [D_1^A] \end{bmatrix} [B] r dr dz \quad (2.89)$$

Note that matrix  $[B]$  depends on the coordinates, unlike in the plane stress case. Thus, the integration in Equation (2.89) is more difficult to do. A simple approximate

integration procedure is used to determine [B] for a centroidal point of coordinates  $(\bar{r}, \bar{z})$

$$\begin{aligned}\bar{r} &= \frac{(r_i + r_j + r_m)}{3} \\ \bar{z} &= \frac{(z_i + z_j + z_m)}{3}\end{aligned}\tag{2.90}$$

where  $r_{i,j,m}$  and  $z_{i,j,m}$  are the coordinates of the three nodes of the finite element.

The stiffness matrix then becomes

$$[k] = 2\pi [\bar{B}]^T \begin{bmatrix} [D_1] & [-D_1] \\ [-D_1] & [D_1^A] \end{bmatrix} [\bar{B}] \bar{r} \Delta = \begin{bmatrix} [K_1] & -[K_1] \\ -[K_1] & [K_1^A] \end{bmatrix}_{12 \times 12}\tag{2.91}$$

Zienkiewicz [20] considers the approximate integration to be superior to the exact integration, since the exact formulation yields logarithmic terms, which at large distances from the axis of symmetry may yield inaccurate results.

The damping matrix is found using similar considerations as in the plane stress case [33]

$$[c] = \int_V [B]^T \begin{bmatrix} \{0\} & \{0\} \\ \{0\} & \frac{[D_1^A]}{\Omega} \end{bmatrix} [B] dV = 2\pi \int [B]^T \begin{bmatrix} \{0\} & \{0\} \\ \{0\} & \frac{[D_1^A]}{\Omega} \end{bmatrix} [B] r dr dz\tag{2.92}$$

For a centroidal point of coordinates  $(\bar{r}, \bar{z})$ , the damping matrix becomes

$$[c] = 2\pi [\bar{B}]^T \begin{bmatrix} \{0\} & \{0\} \\ \{0\} & \frac{[D_1^A]}{\Omega} \end{bmatrix} [\bar{B}] \bar{r} \Delta = \begin{bmatrix} \{0\} & \{0\} \\ \{0\} & \frac{[K_1^A]}{\Omega} \end{bmatrix}_{12 \times 12}\tag{2.92a}$$

Just like in the plane stress case, the mass matrix of the ADF axisymmetric element does not include any contribution from the anelastic displacement fields and resembles the mass matrix of a simple, elastic, triangular axisymmetric finite element

$$\begin{aligned}
 [m] &= \rho \int_V \begin{bmatrix} [N_2] & 0 & 0 & 0 \\ 0 & [N_2] & 0 & 0 \\ 0 & 0 & 0 & 0 \\ 0 & 0 & 0 & 0 \end{bmatrix}^T \begin{bmatrix} [N_2] & 0 & 0 & 0 \\ 0 & [N_2] & 0 & 0 \\ 0 & 0 & 0 & 0 \\ 0 & 0 & 0 & 0 \end{bmatrix} dV = \dots \\
 &= 2\pi\rho \iint \begin{bmatrix} [N_2] & 0 & 0 & 0 \\ 0 & [N_2] & 0 & 0 \\ 0 & 0 & 0 & 0 \\ 0 & 0 & 0 & 0 \end{bmatrix}^T \begin{bmatrix} [N_2] & 0 & 0 & 0 \\ 0 & [N_2] & 0 & 0 \\ 0 & 0 & 0 & 0 \\ 0 & 0 & 0 & 0 \end{bmatrix} r dr dz
 \end{aligned} \tag{2.93}$$

or

$$[m] = 2\pi\rho \iint \begin{bmatrix} [M_1]_{3 \times 3} & \{0\}_{3 \times 3} & \{0\}_{3 \times 3} & \{0\}_{3 \times 3} \\ \{0\}_{3 \times 3} & [M_1]_{3 \times 3} & \{0\}_{3 \times 3} & \{0\}_{3 \times 3} \\ \{0\}_{3 \times 3} & \{0\}_{3 \times 3} & \{0\}_{3 \times 3} & \{0\}_{3 \times 3} \\ \{0\}_{3 \times 3} & \{0\}_{3 \times 3} & \{0\}_{3 \times 3} & \{0\}_{3 \times 3} \end{bmatrix} r dr dz \tag{2.94}$$

The mass matrix evaluated around the centroidal point is

$$[m] = 2\pi\rho\Delta\bar{r} \begin{bmatrix} [M_1]_{3 \times 3} & \{0\}_{3 \times 3} & \{0\}_{3 \times 3} & \{0\}_{3 \times 3} \\ \{0\}_{3 \times 3} & [M_1]_{3 \times 3} & \{0\}_{3 \times 3} & \{0\}_{3 \times 3} \\ \{0\}_{3 \times 3} & \{0\}_{3 \times 3} & \{0\}_{3 \times 3} & \{0\}_{3 \times 3} \\ \{0\}_{3 \times 3} & \{0\}_{3 \times 3} & \{0\}_{3 \times 3} & \{0\}_{3 \times 3} \end{bmatrix}_{12 \times 12} \tag{2.94a}$$

where

$$[M_1] = [N_2]^T [N_2] = \begin{bmatrix} (N_i)^2 & N_i N_j & N_i N_m \\ N_i N_j & (N_j)^2 & N_m N_j \\ N_i N_m & N_m N_j & (N_m)^2 \end{bmatrix} \quad (2.95)$$

### 2.3. Boundary conditions

A complete set of equations describing the time evolution of a continuum requires a set of geometric and force boundary conditions. In the ADF case, the total displacement field requires the specification of either geometric or force boundary conditions [33]. The anelastic displacement field is coupled to the total displacement field through strain and cannot have its own force boundary conditions. However, boundary conditions applied to the total displacement field induce certain boundary conditions on the ADF [33]. Consider the dynamic ADF finite element analysis of a free-free continuum; i.e., longitudinal wave propagation through a free-free bar caused by a sharp impact at one end of the bar. Since the anelastic displacement field does not contribute to the mass matrix, the latter is ill conditioned. To solve the system of equations, the ADF degrees of freedom of at least one node must be fully constrained. This constraint improves the conditioning of the matrix and allows the system to be solved. It means physically that rigid body motion of an internal variable associated with the ADF is not permitted. Eliminating rigid body motion from the anelastic field does not affect coupling.

### 2.4. Multiple Anelastic Displacement Fields

Multiple ADF are required if the behavior of materials that exhibit weak frequency dependence is to be modeled accurately. The anelastic displacement field may be expressed as a sum of ADF corresponding to individual relaxation phenomena [30]

$$u^A(x, t) = \sum_{n=1}^N u_n^A(x, t), \quad (2.96)$$

and the constitutive equations become

$$\sigma_{ij} = E_{ijkl} \left( \varepsilon_{kl} - \sum_{n=1}^N \varepsilon_{nkl}^A \right) \quad (2.97)$$

and

$$\sigma_{nij}^A = E_{ijkl} \varepsilon_{kl} - E_{nijkl}^A \varepsilon_{nkl}^A \quad (2.98)$$

The equation of motion and the relaxation equation become a set of N equations [33]

$$\rho u_{i,tt} - \left( E_{ijkl} \left( \varepsilon_{kl} - \sum_{n=1}^N \varepsilon_{nkl}^A \right) \right)_{,j} = f_i \quad (2.99)$$

$$\left( \frac{1}{\Omega_n} E_{nijkl}^A \varepsilon_{nkl,t}^A - E_{ijkl} \varepsilon_{kl} + E_{nijkl}^A \varepsilon_{nkl}^A \right)_{,j} = 0 \quad (2.100)$$

The multiple ADF mass, stiffness, and damping matrices are obtained in the same way as for a single ADF case. For example, the stiffness matrix for a five ADF, axisymmetric, triangular, finite element is

$$[k] = \int_V [B]^T \begin{bmatrix} [D_1] & [-D_1] & [-D_2] & [-D_3] & [-D_4] & [-D_5] \\ [-D_1] & [D_1^A] & \{0\} & \{0\} & \{0\} & \{0\} \\ [-D_2] & \{0\} & [D_2^A] & \{0\} & \{0\} & \{0\} \\ [-D_3] & \{0\} & \{0\} & [D_3^A] & \{0\} & \{0\} \\ [-D_4] & \{0\} & \{0\} & \{0\} & [D_4^A] & \{0\} \\ [-D_5] & \{0\} & \{0\} & \{0\} & \{0\} & [D_5^A] \end{bmatrix} [B]_{24 \times 36} dV \quad (2.101)$$

where, for  $i=1,2,5$ ,

$$[D_i^A] = \begin{bmatrix} E_{i1}^A & E_{i2}^A & E_{i2}^A & 0 \\ E_{i2}^A & E_{i1}^A & E_{i2}^A & 0 \\ E_{i2}^A & E_{i2}^A & E_{i1}^A & 0 \\ 0 & 0 & 0 & E_{i3}^A \end{bmatrix} \quad (2.102)$$

and

$$[D_1] = \begin{bmatrix} E_1 & E_2 & E_2 & 0 \\ E_2 & E_1 & E_2 & 0 \\ E_2 & E_2 & E_1 & 0 \\ 0 & 0 & 0 & E_3 \end{bmatrix} \quad (2.103)$$

The damping matrix is

$$[c] = \int_V [B]^T \begin{bmatrix} \{0\}_{4 \times 4} & \{0\} & \{0\} & \{0\} & \{0\} & \{0\} \\ \{0\} & \frac{[D_1^A]}{\Omega_1} & \{0\} & \{0\} & \{0\} & \{0\} \\ \{0\} & \{0\} & \frac{[D_2^A]}{\Omega_2} & \{0\} & \{0\} & \{0\} \\ \{0\} & \{0\} & \{0\} & \frac{[D_3^A]}{\Omega_3} & \{0\} & \{0\} \\ \{0\} & \{0\} & \{0\} & \{0\} & \frac{[D_4^A]}{\Omega_4} & \{0\} \\ \{0\} & \{0\} & \{0\} & \{0\} & \{0\} & \frac{[D_5^A]}{\Omega_5} \end{bmatrix} [B] dV \quad (2.104)$$

$_{24 \times 24}$



The mass matrix has no contribution from the anelastic fields and is shown in Equation (2.105).

$$[m] = \int_V \rho \begin{bmatrix} \begin{bmatrix} [M_1] & \{0\} \\ \{0\} & [M_1] \end{bmatrix}_{6 \times 6} & \begin{bmatrix} \{0\} & \{0\} & \{0\} & \{0\} & \{0\} \end{bmatrix} \\ \begin{bmatrix} \{0\} \\ \{0\} \\ \{0\} \\ \{0\} \\ \{0\} \end{bmatrix}_{5 \times 1} & \begin{bmatrix} \{0\} & \{0\} & \{0\} & \{0\} & \{0\} \\ \{0\} & \{0\} & \{0\} & \{0\} & \{0\} \\ \{0\} & \{0\} & \{0\} & \{0\} & \{0\} \\ \{0\} & \{0\} & \{0\} & \{0\} & \{0\} \\ \{0\} & \{0\} & \{0\} & \{0\} & \{0\} \end{bmatrix}_{5 \times 5} \end{bmatrix} dV \quad (2.105)$$

## 2.5. Determination of model input from material complex moduli data

The ADF method can describe the material moduli frequency dependence. The value of an individual scalar modulus  $\beta_m^*$ , at a given circular frequency  $\omega$  (rad/s), is [33]

$$\beta_m^*(\omega) = \beta_{mr} \left( 1 + \sum_{n=1}^N \Delta_{mn} \frac{(\omega / \Omega_n)^2}{1 + (\omega / \Omega_n)^2} \right) + i \beta_{mr} \left( \sum_{n=1}^N \Delta_{mn} \frac{(\omega / \Omega_n)}{1 + (\omega / \Omega_n)^2} \right) \quad (2.106)$$

where  $\beta_m^*$  is the complex modulus,  $\beta_{mr}$  is the relaxed or low-frequency modulus and  $\Omega_n$  is the characteristic relaxation time at constant strain corresponding to the n-th anelastic displacement field. The high-frequency (or unrelaxed) modulus is [33]

$$\beta_m = \beta_{mr} (1 + \Delta_{mtotal}) \quad (2.107)$$

where

$$\Delta_{mtotal} = \sum_{n=1}^N \Delta_{mn} \quad (2.108)$$

For an isotropic material, the ADF model input parameters are determined by curve fitting the predicted material moduli (bulk and shear) to the corresponding experimental values. The input parameter values are adjusted iteratively to minimize differences between predicted and experimental values in a least square approximation method. The number of anelastic displacement fields used determines how well the predicted material data compares to the measured value over a given frequency range. More than one ADF are required to approximate material moduli that exhibit weak frequency dependence, especially if the frequency range of interest spans several decades. In the case of impact, for example, the frequency spectrum usually contains important frequency components extending from DC to a few kHz.

Lesieutre [34] and Govindswamy [35] use the following formula to compute the relaxation magnitude for a single ADF finite element:

$$\Delta = 2\eta_p \left[ \eta_p + \sqrt{1 + \eta_p^2} \right] \quad (2.109)$$

where  $\eta_p$  is the peak loss factor and the inverse of the relaxation time is

$$\Omega = \omega_p (1 + \Delta)^{1/2} \quad (2.110)$$

where  $\omega_p$  is the circular frequency corresponding to the peak loss factor value.

### CHAPTER 3. RESULTS AND DISCUSSION

The main purpose of this chapter is to present and analyze the ability of axisymmetric and plane stress ADF (anelastic displacement field) finite elements (FE) to accurately model and investigate the dynamic behavior of two- and three-dimensional structures subjected to shock loads.

One application of these particular finite element models (FEM) is the design of mechanical filters and in particular filters used in shock accelerometers. Shock sensors must withstand severe acceleration environments, sometimes in excess of  $1,000,000 \text{ m/s}^2$ . As a result, it is often necessary to protect the sensing element (usually made of quartz crystal) from the shock loads with a viscoelastic mechanical filter. The mechanical filter may be an O-ring or a round plate.

Another ADF-based FE application is the investigation of shock wave propagation through structures characterized by weak or strong frequency dependence of material properties. In particular, the study of longitudinal wave propagation through bars relates to the Hopkinson bar shock sensor calibration procedure. A bar with a high- or low-loss factor may be used in this calibration procedure, depending on the desired frequency content of the shock pulse. If the same impact force is applied to the end of a low- and high-loss bar, the resulting pulse that propagates through the high loss-factor bar generally has longer duration and lower shock level, than the pulse propagating through the lower loss-factor bar. That is because of viscoelastic dispersion and attenuation that occur in the high loss bar. Thus, it would be of interest to predict the peak magnitude and the frequency content of the shock pulse hitting the test shock accelerometer, which is mounted at the other end of the bar. Longitudinal wave propagation has been studied extensively and results obtained through the ADF FE method may be compared against previous experiments and theoretical predictions. ADF finite elements allow the modeling of longitudinal wave propagation through an elastic bar with a viscoelastic mechanical filter at one end. Such is the case when a shock accelerometer featuring a mechanical filter is calibrated on a Hopkinson bar. ADF plane stress FE may also be

employed to study wave propagation in viscoelastic bars with square or rectangular cross sections, since exact solutions do not exist for these types of problems, or study vibration of beams with damping layers.

### 3.1. Numerical and computational considerations

The transient response of the finite element models considered in what follows is obtained through direct integration of the equations of motion by the Newmark trapezoidal rule (or constant average acceleration method) [49-50]. The Newmark method is characterized by two factors:  $\alpha$  and  $\beta$ . The trapezoidal rule, or constant average acceleration method is characterized by  $\alpha=1/4$  and  $\beta=1/2$ . This method was chosen because it is implicit, and unconditionally stable for the chosen  $\alpha$  and  $\beta$ ; due to accuracy reasons, however, the time step must be chosen properly in relation to the finite element length. The time step may be taken to be greater than the one chosen in the central difference method, which allows for savings in computation time. This choice of parameters allows no amplitude decay and retains the high frequency response. In order to allow for amplitude decay,  $\beta$  must be greater than 0.5 and  $\alpha$  is

$$\alpha = \frac{1}{4}(\beta + 0.5)^2 \quad (3.1)$$

Since in shock problems a large number of frequencies are excited, it is necessary for analysis purposes to define a high cutoff frequency needed to obtain reasonable solution accuracy [49]. The goal is to determine that cutoff frequency  $\omega_{c0}$  and to define a finite element mesh accordingly. The cutoff frequency to be included determines the critical wavelength to be represented,  $L_w$ . The total time for the corresponding wave to travel past a point is [49]

$$t_w = \frac{L_w}{c} \quad (3.2)$$

where  $c$  is the wave velocity at the corresponding frequency. Assuming that  $n$  time steps are necessary to properly represent the waveform of wavelength  $L_w$ , the time step is

$$\Delta t = \frac{t_w}{n} \quad (3.3)$$

In finite element practice,  $n$  is recommended to be equal or greater than 20 [49]. The element length is thus

$$L_e = c \Delta t \quad (3.4)$$

Numerical damping is introduced to alleviate integration errors if the ratio  $\Delta t/t_w$  is large.

### 3.2. Longitudinal wave propagation through bars-comparison of finite element results to theory

In this section, the validity of results predicted with plane stress and axisymmetric ADF FEM are compared against theoretical results. The first case considered is the propagation of a longitudinal wave along a clamped-free, titanium alloy bar. The longitudinal wave is generated by the sudden release of a force initially acting on the free end of the bar [51]. The second case studied is the propagation of a longitudinal wave along a free-free titanium alloy bar. In this case, a versed sine impact force at one free end generates the longitudinal wave.

In both wave propagation studies, an elastic FEM could have provided similar answers to an ADF FEM model, since material properties of metals generally show weak frequency dependence. However, the ability of ADF FEM to properly approximate weak frequency dependence and to accurately predict displacement and wave propagation velocities under these conditions is established.

### 3.2.1. Longitudinal wave propagation through an elastic clamped-free bar

The first theoretical case considered was the longitudinal wave propagation along a titanium-alloy (Ti6Al4V), clamped-free bar 2.033 m long with a 1.9-cm cross section diameter, loaded initially by a 20-kN force ( $F_0$ ) at the free end (Reference [1]). The force loading was equivalent to an initial displacement along the length of the bar of

$$u(x, z)|_{t=0} = \frac{F_0 x}{AE}, \quad (3.5)$$

where  $L$  and  $A$  are the length and area, respectively, of the bar,  $E$  is the low frequency Young's modulus, and  $\epsilon_0(x, t=0)$  is the initial strain at a station  $x$  along the bar. After the force is released, theory predicts a displacement  $u(x, t)$  at time  $t$  and longitudinal station  $x$  along the bar equal to ( $c$  is the velocity of sound in the bar) to be

$$u(x, t) = 8 \frac{F_0 L}{AE \pi^2} \sum_i \frac{(-1)^i}{(2i+1)^2} \sin \left[ \left( \frac{2i+1}{2L} \right) \pi x \right] \cos \left[ \left( \frac{2i+1}{2L} \right) \pi c t \right] \quad (3.6)$$

The material input parameters that characterize the titanium alloy are shown in Table 3.1.

Table 3.1. Material parameters for Ti6Al4V

Density(kg/m <sup>3</sup> )	Relaxed shear modulus (Pa)	Young's modulus (Pa)	Poisson's ratio	Loss factor <sup>*</sup>
4408.2	4.206e10	1.1377e11	0.29	0.0018

<sup>\*</sup> assumed to be constant over chosen frequency range of interest: 0.1 to 2500 Hz

The release of the initial force  $F_0$  is equivalent to a displacement step input. The amplitude spectrum of the step force input has the highest energy density concentrated at low frequencies. Thus, the material properties' frequency dependence is modeled with

ADF over a 1Hz to 2.5 kHz frequency range. The limits of the approximation frequency range are determined by the number of ADF used (the more ADF, the wider the frequency range that may be modeled). Table 3.2. shows the ADF parameters used to model the material properties for the Ti6Al4V alloy.

Table 3.2. ADF parameters used (five ADF) for Ti6Al4V alloy

Parameter	1	2	3	4	5
$\Omega/2\pi$ (Hz)	1E-1	1E0	1E1	2E2	3E3
$\Delta_G^*$	0.0013	0.00116	0.0012	0.0011	0.0014

\* $\Delta_G = \Delta_K$  relaxation strengths corresponding to the shear and bulk modulus, respectively, are assumed equal.

The results of the ADF approximation of the storage and loss moduli are shown in Figure 3.1. The approximation was performed using a least square method based code developed at Penn State. It may be seen that the curve fit approximates within 10% both the loss and storage moduli at any frequency included in the frequency range of interest.

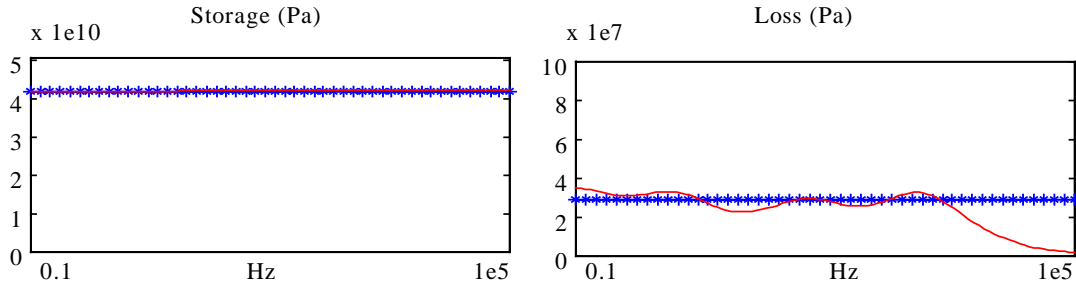


Figure 3.1. Ti6Al4V alloy loss and storage moduli data fit with five ADF

For comparison purposes, the material data of Ti6Al4V is also approximated using one ADF terms. The parameters used to approximate material data over the frequency range of interest, using one ADF, are shown in Table 3.3.

Table 3.3. ADF parameters used for Ti6Al4V alloy (one ADF)

Parameter	1
$\Omega/2\pi$ (Hz)	10
$\Delta_G^*$	0.003

\* $\Delta_G = \Delta_K$  relaxation strengths of the shear and bulk modulus, respectively, are assumed equal

The results of the approximation of the storage and loss moduli with one ADF are shown in Figure 3.2.

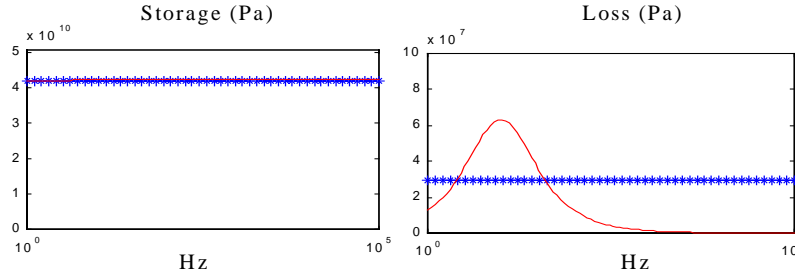


Figure 3.2. Ti6Al4V alloy loss and storage moduli data fit with one ADF

The storage modulus' frequency dependence is well approximated (within 2%), while the loss modulus' frequency dependence is not. At low and at high frequencies, the loss factor approximated with one ADF is much lower than desired. As a result, high-frequency components of the velocity or displacement spectrum are less damped than they would be in reality.

The ADF axisymmetric finite element model mesh for the bar uses a grid of 4 nodes along the radius by 20 nodes along the length of the bar. This mesh is shown schematically in Figure 3.3. (the length of the element in the Z direction is greater than the length of the element in the radial dimension). The force  $F_0$  is applied at the center of the bar. Clamped boundary conditions are applied on all four nodes found at the clamped



end of the bar on the elastic degrees of freedom. The ADF degrees of freedom are also constrained for just one node, due to reasons explained in Section 2.3.

The element size is 0.1 cm and is chosen in part due to numerical reasons. A time step of  $1.99\text{e-}5$  seconds is determined based on Equation (3.4), which corresponds, in turn, to a critical frequency of approximately 2.5kHz. The time step used is, however,  $6.5\text{e-}7$  seconds, to improve the time resolution.

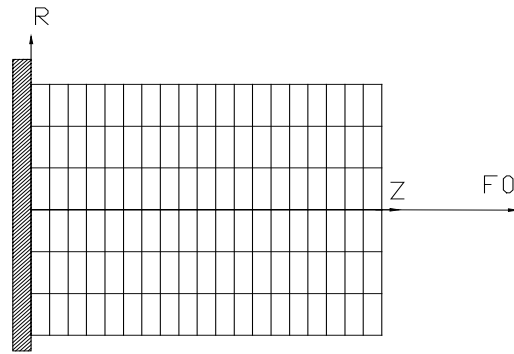


Figure 3.3. Finite element mesh for the clamped-free bar, ADF axisymmetric FE

In Figures 3.4. and 3.5., the longitudinal displacement time history predicted using axisymmetric finite elements with one and five ADF is compared to theory. Good agreement between the finite element predicted and theoretical displacement time histories is observed. For example, after 325 microseconds at one meter away from the clamped end, the relative error of the predicted vs. theoretical displacements is 7.5%, and 4% for one and five ADF FEM, respectively. Little difference in results is observed between the one ADF and five ADF predictions, although the five ADF FEM yields slightly better results in terms of magnitude.

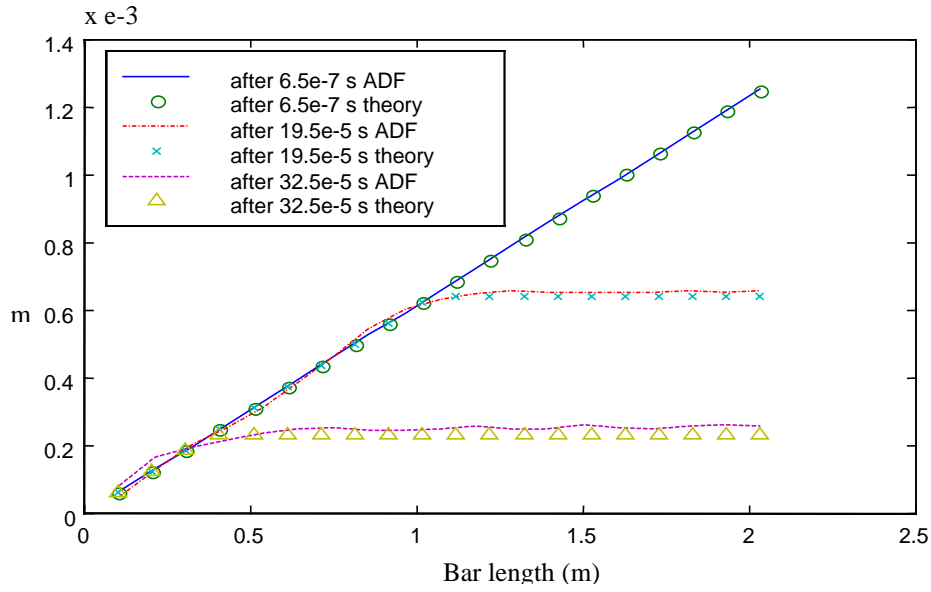


Figure 3.4. Time record of predicted longitudinal displacement vs. theory (one ADF)

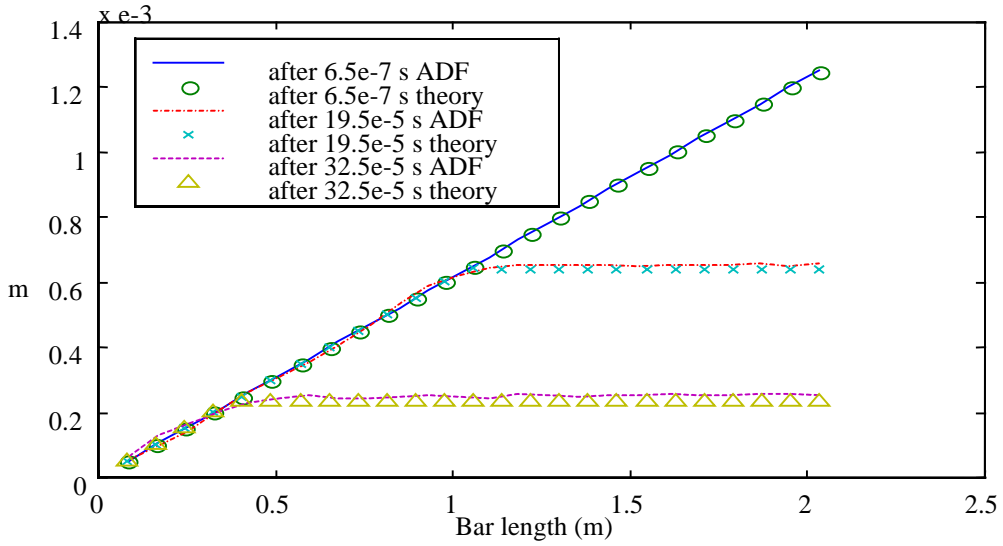


Figure 3.5. Time record of predicted longitudinal displacement vs. theory (five ADF)

The finite element predicted wave propagation velocity agrees well with speed of sound in the titanium alloy ( $c=5080.2$  m/s computed using the relaxed Young's modulus  $E_r$ ): the

FEM predicts a sound velocity of approximately 5153 m/s - a relative error of 1.5% compared to the experimental value.

Next, a plane stress ADF finite element model is used to model the wave propagation for the same problem as above. The plane stress FE mesh modeling the bar is different from the mesh used in the axisymmetric case in that there are 2 rows of elements by 96 elements for each row. A representation of the mesh is shown in Figure 3.6.

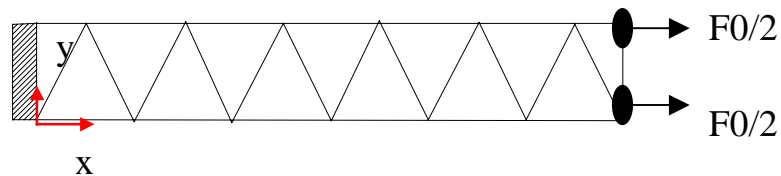


Figure 3.6. Plane stress finite element mesh for clamped-free bar

Five ADFs are used to model material behavior. The round cross section of the bar is substituted with a rectangular cross section of equivalent area (3-mm thickness by 100-mm depth). The element size is chosen to be approximately 0.01 m long. This type of grid has little resolution in the cross section, but has more elements in the longitudinal direction. A time step of 1.97e-6 seconds is determined based on Equation 3.4, which corresponds, in turn, to a critical frequency of approximately 25 kHz. The time step used is, as before, 6.5e-7 seconds, for better time resolution. The time step and element size chosen for this type of mesh and FE allow good modeling of high frequency (up to 25 kHz) content in the transient response.

There is very good agreement between the finite element predicted longitudinal displacement and theory (as shown in Figure 3.7.). For example, after 195 microseconds, the predicted displacement has a relative error of approximately 2% when compared to theory. Predicted propagation velocity is less than 1% in error versus the experimental value.

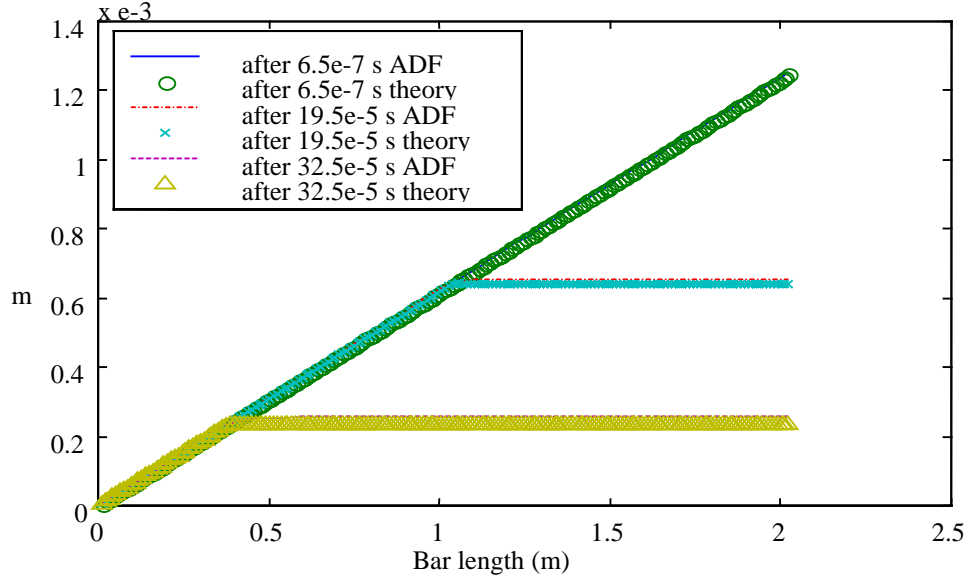


Figure 3.7. Time record of predicted longitudinal displacement vs. theory, plane stress element with five ADF

### 3.2.2. Longitudinal wave propagation along a titanium alloy free-free bar

In this section, the ability of the new finite elements to predict shock behavior of structures consisting of materials with weak frequency dependence is investigated. The second theoretical case considered is the longitudinal wave propagation along a titanium alloy (Ti6Al4V) bar with free-free boundary conditions after one of the ends is subjected to impact. A compressive, versed-sine force  $F$  with a period  $T$  of 26.2 microseconds, described in Figure 3.8. and Equation 3.3, produces the impact.

$$F = 237.73 \left( 1 - \cos \left( 2\pi \frac{t}{T} \right) \right) \quad [\text{N}] \quad (2.13)$$

As in the previous theoretical case, the bar considered is 2.03-m long, with a diameter of 1.9-cm. A grid of 120 nodes (4 rows by 30 columns), similar to the one shown in Figure 3.3., models the bar. The corresponding time step, considering a propagation velocity of 5080 m/s, is 13 microseconds. For better time resolution, the time step is chosen to be 1

microsecond. The grid size and time step size allow critical frequencies up to 3.75 kHz to be accurately represented in the transient response.

Figure 3.9. shows the time history of the longitudinal displacement at the free end and in the middle of the bar. The end of the bar moves in small steps, as opposed to having one continuous motion, at time intervals of  $2L/c_0$ , where  $c_0$  is the velocity of sound through the bar. These predicted results compare well qualitatively to both theory and experiments [39]. The middle of the bar is moving twice as often as the end of the bar, because the wave travels through it twice for each reflection at an end.

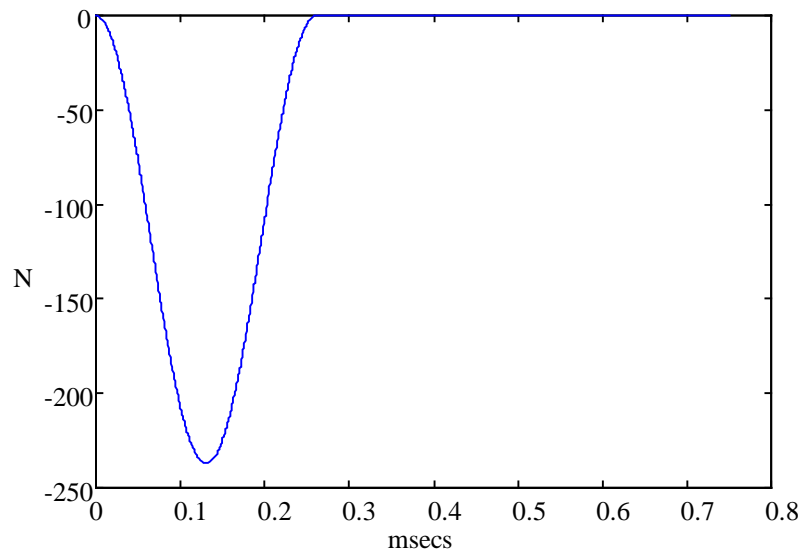


Figure 3.8. Impact force on end of bar

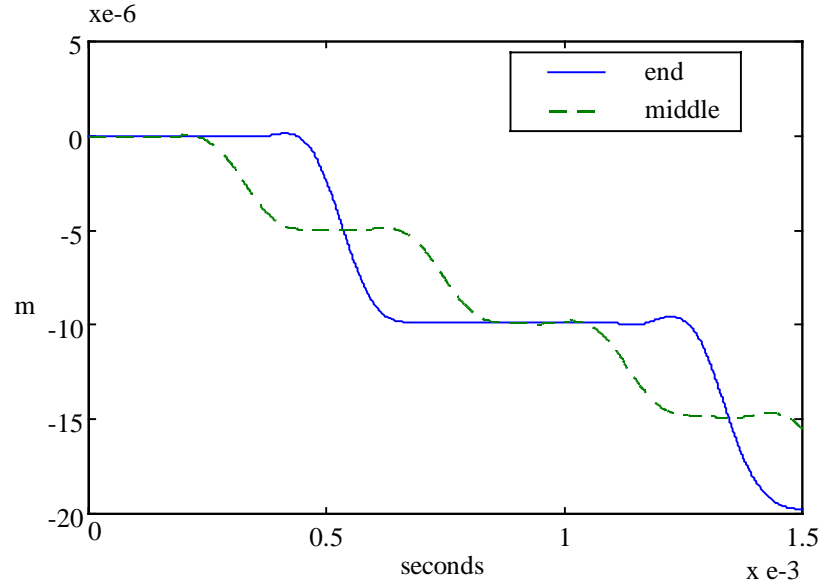


Figure 3.9. Longitudinal displacement time history at free end and in middle of bar

The change in the magnitude of the longitudinal displacement in the middle is half of that at the free end (the small "bumps" present at the beginning of each displacement step are caused by coarseness of the node mesh).

Figure 3.10. shows the longitudinal velocity of the middle and of the end of the bar. Figure 3.11. shows the velocity pulse along the bar at various time instances. The amplitude of the pulse varies little as it reflects back and forth along the bar, since the loss factor of the Ti alloy is small (approximately 0.0018 [52]). The predicted propagation velocity matches the speed of sound in Ti6Al4V ( $c=5080$  m/s).

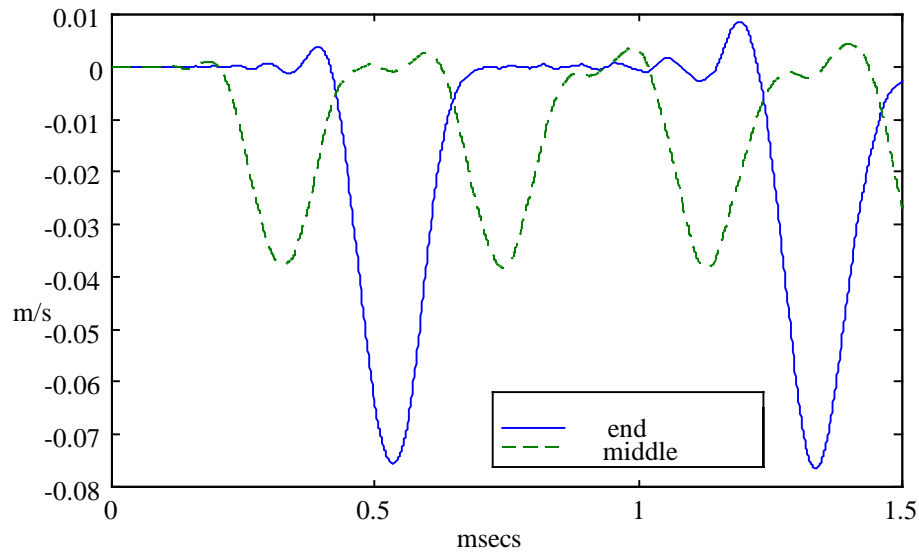


Figure 3.10. Longitudinal velocity's time history at the free end and at the middle

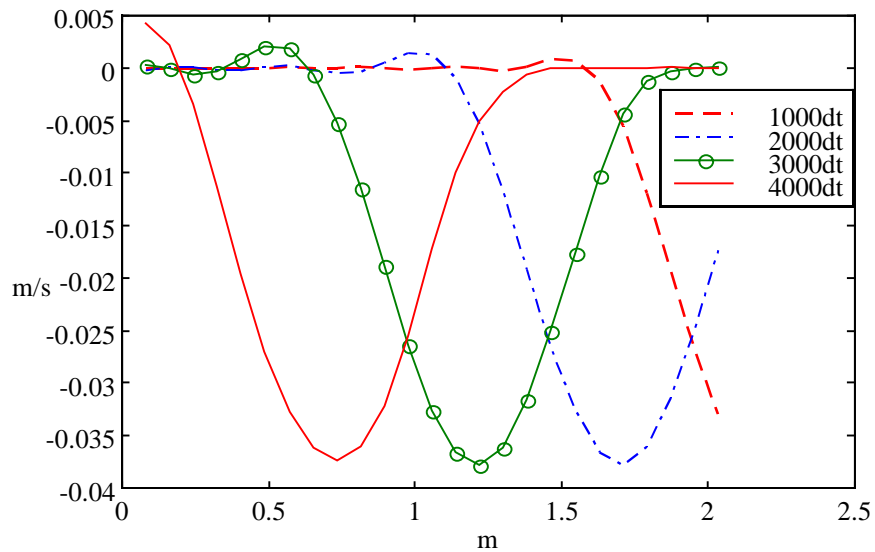


Figure 3.11. Propagation of particle velocity pulse along bar

### 3.2.3. Longitudinal wave propagation along a viscoelastic free-free bar

The next numerical study is the propagation of a longitudinal wave along a PERSPEX<sup>TM</sup> free-free bar. PERSPEX<sup>TM</sup> is a plastic material characterized by high loss factor (three orders of magnitude higher than that of most metals), has a relaxed Young's modulus of

$E_r=4.18\text{GN}$  and a density of  $\rho=1185\text{ kg/m}^3$ . Numerically, the longitudinal wave is generated by a half sine force of 1000N magnitude and 3333 Hz frequency acting on one free end of the bar. The bar is 2.0 m long and has a cross sectional area of  $2.85\text{e-}4\text{ m}^2$ . The models employ both ADF plane stress and ADF axisymmetric FE. Table 3.4. shows the input ADF parameters.

Table 3.4. ADF parameters used for PERSPEX<sup>TM</sup> (one ADF)

Parameter	1
$\Omega$ (rad/s)	27000
$\Delta_G^*$	0.185

\* $\Delta_G = \Delta_K$  relaxation strengths of the shear and bulk modulus, respectively, are assumed equal

The particle velocity record obtained with a one-ADF plane stress FEM, at three longitudinal stations as a function of time, is depicted in Figure 3.12. The effects of wave attenuation due to the rheological properties of the bar are clearly shown. Since the high frequency components travel faster (the front of the pulse is steeper than the back) and are attenuated more rapidly than those of lower frequency, the velocity pulse decreases in magnitude and lengthens as it travels along the bar. As time progresses, the pulse spreads until it merges with the pulse going in the opposite direction; this can be clearly seen at the middle of the bar. Note that at the free end, the velocity doubles. The predicted propagation velocity is 1858 m/s, which is close to the velocity of sound computed with the relaxed Young's modulus,  $c=1738\text{ m/s}$ . As the pulse spreads, it tends to attain what is called an "Universal Pulse Shape" [38]. Figure 3.13. depicts the longitudinal history of the displacement as it travels along the bar. The sharp succession of displacement steps characterizing the first reflections slowly tend to become more rounded with time [39]. Eventually, these steps merge into a straight line corresponding to a constant bar velocity. The same displacement and velocity record are obtained using an ADF axisymmetric FEM (see Figure 3.14. and Figure 3.15.).



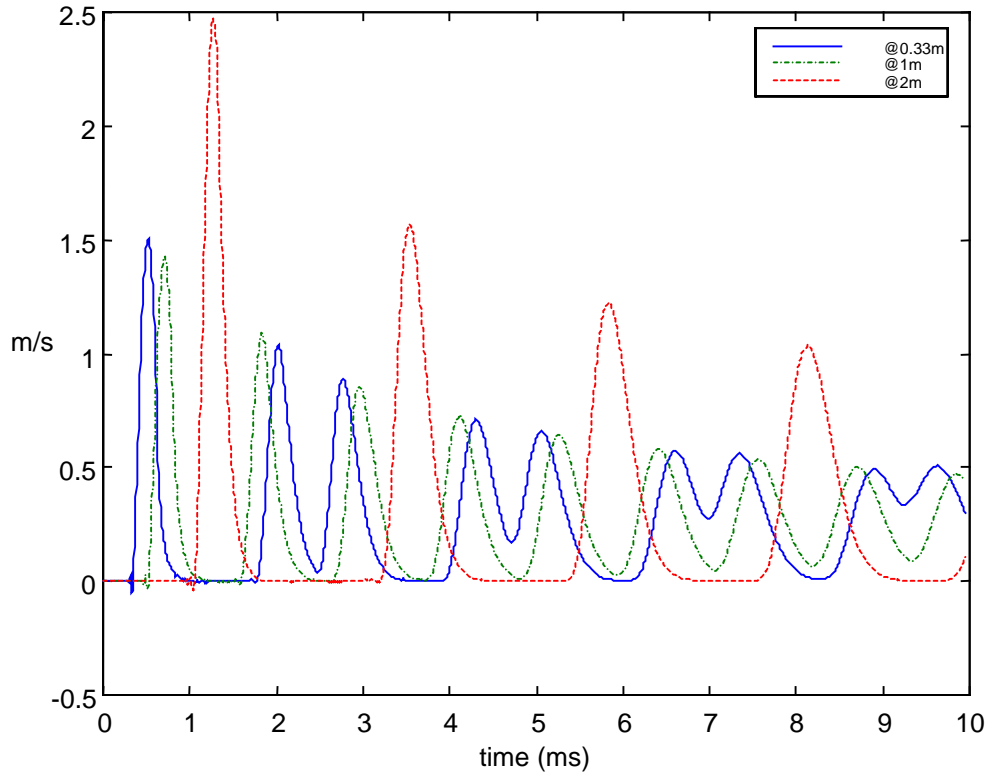


Figure 3.12. Longitudinal wave particle velocity vs. time at three stations along PERSPEX™ bar, ADF plane stress element

Figure 3.16. shows the ADF predicted acceleration at three longitudinal stations along the bar. The mechanical energy is the sum of the strain and kinetic energy. The mechanical energy dissipation is shown in Figure 3.17., where the normalized power spectrum (normalized to its DC component) of the incident stress pulse has more energy than the reflected pulse. That is because because high frequency components are dissipated from the incident to the reflected pulse. Next, an axisymmetric, elastic FEM is considered to model the PERSPEX™ bar. Figure 3.18. shows the predicted displacements. The displacement steps are equal in magnitude and the slope does not change from one step to the other. As opposed to the ADF models, the predicted velocity pulses are symmetrical with respect to their center, since no attenuation is considered and all frequency components travel with the same velocity, as shown in Figure 3.19.

The predicted velocity of propagation is within 2% of that given by

$$c = \sqrt{\frac{E_r}{\rho}} \quad (3.7)$$

Since it is assumed that the frequency components are considered to have the same velocity of propagation, the stress pulse magnitude is higher than the corresponding ADF predicted stress pulse magnitude by 40% and does not attenuate as it propagates. Figure 3.20. shows the ADF model versus the elastic model predicted mechanical energy (equal to the sum of the kinetic and strain energy) as a function of time. The ADF predicted mechanical energy dissipates in time, as opposed to the elastic FEM predicted mechanical energy.

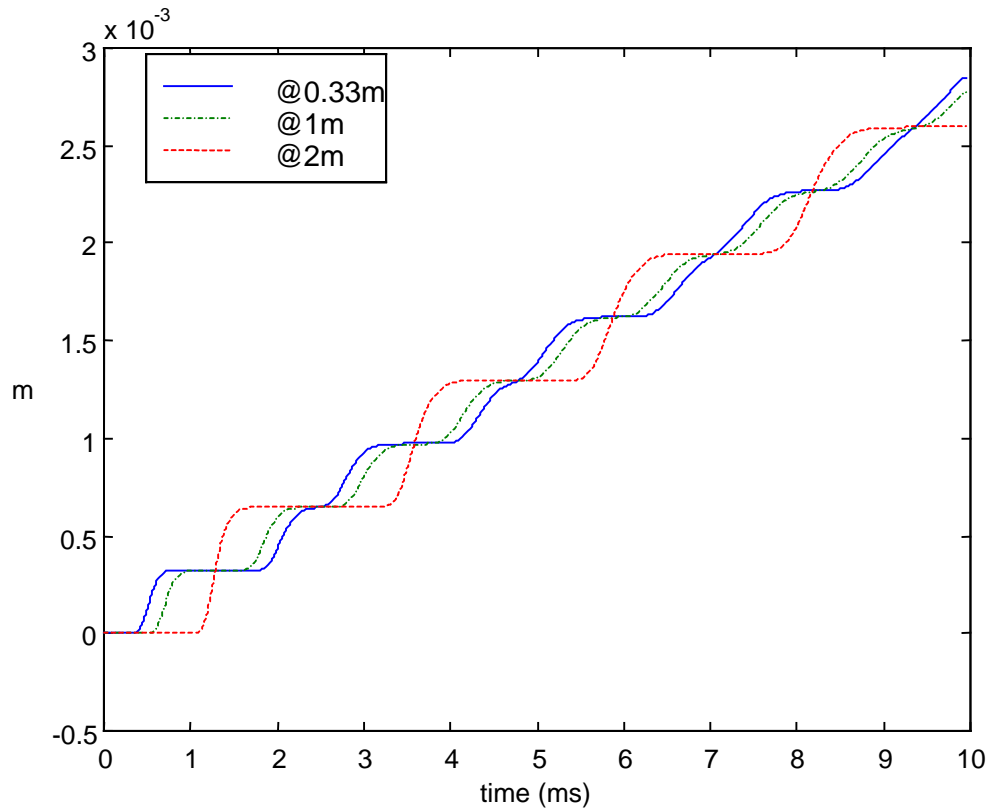


Figure 3.13. Longitudinal wave displacement vs. time at three stations along PERSPEX™ bar, ADF plane stress element

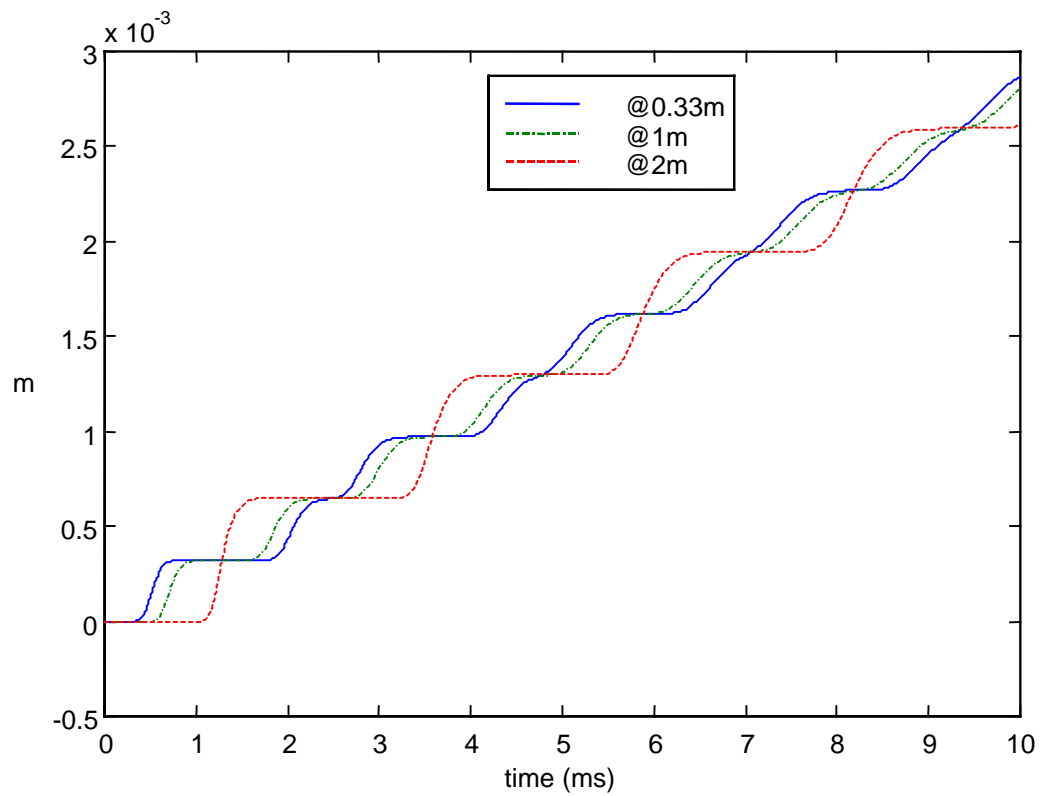


Figure 3.14. Longitudinal wave displacement vs. time at three stations along PERSPEX<sup>TM</sup> bar, ADF axisymmetric FE

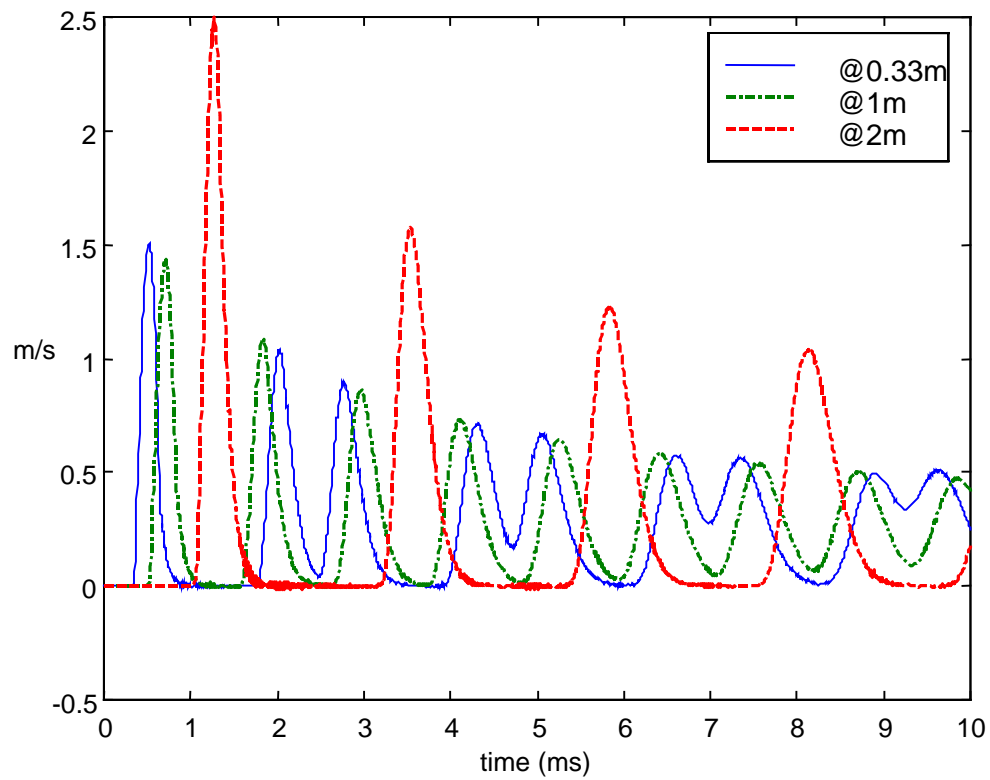


Figure 3.15. Longitudinal wave particle velocity vs. time at three stations along PERSPEX<sup>TM</sup> bar, ADF axisymmetric FE

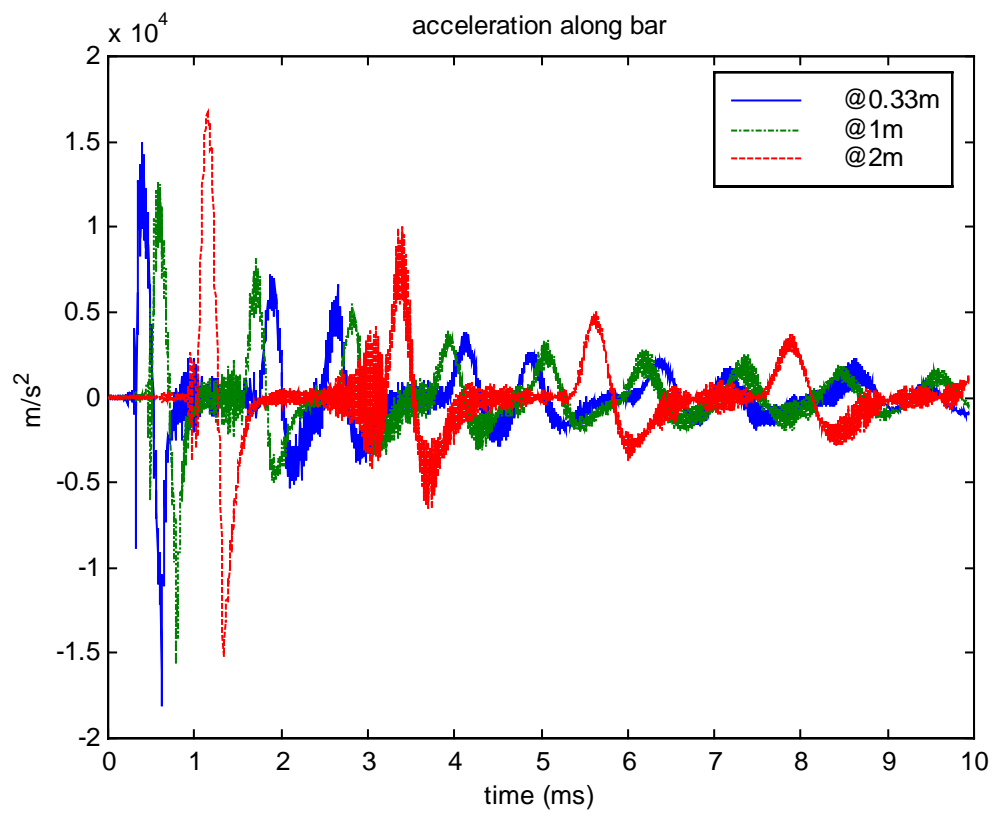


Figure 3.16. Longitudinal wave acceleration vs. time at three stations along PERSPEX<sup>TM</sup> bar, ADF axisymmetric FE

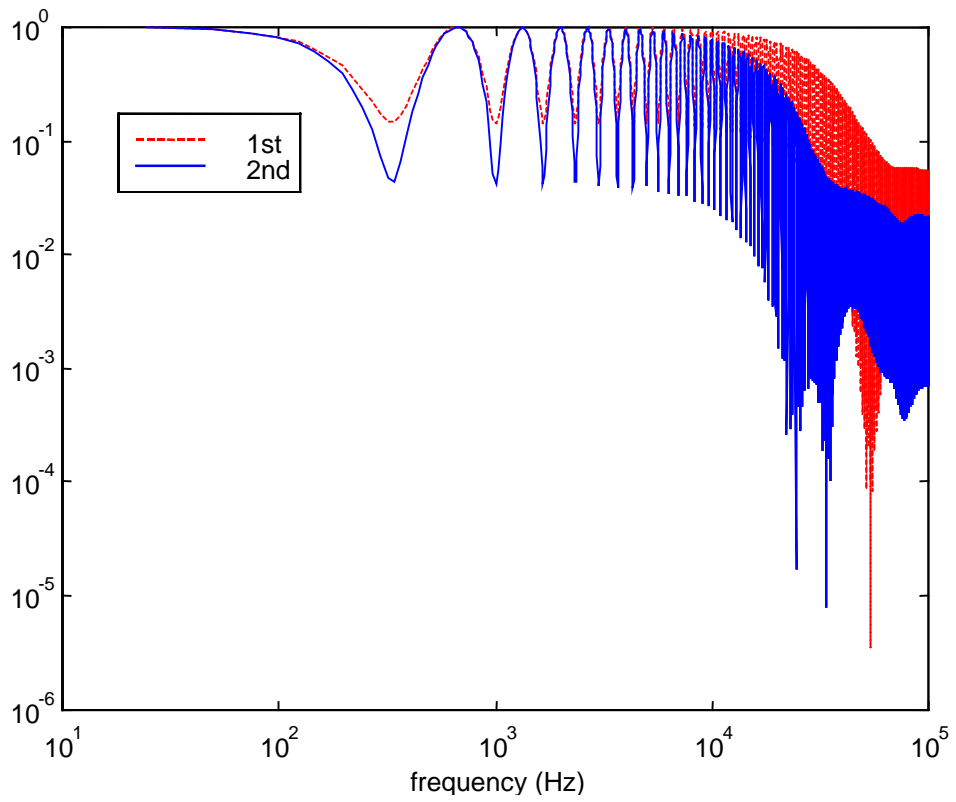


Figure 3.17. High frequency components dissipate from 1<sup>st</sup> (incident) to 2<sup>nd</sup> (reflected) stress pulse at free end

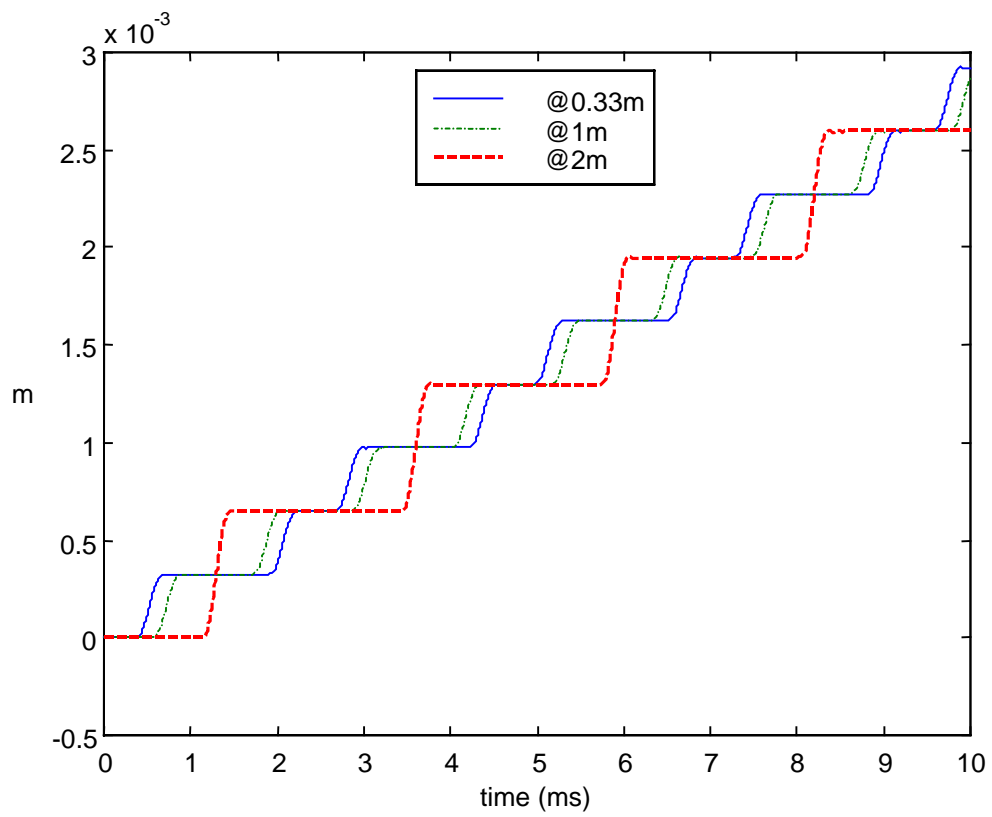


Figure 3.18. Time record of elastic longitudinal displacement along PERSPEX™ bar

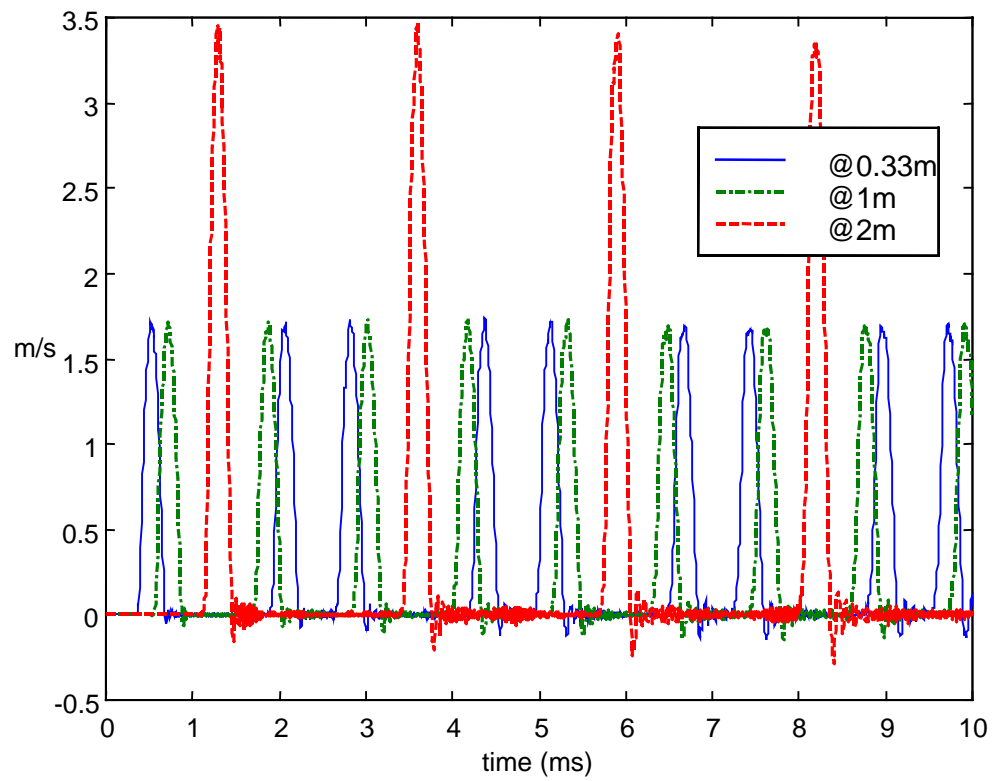


Figure 3.19. Time record of longitudinal velocity along PERSPEX™ bar, elastic FEM



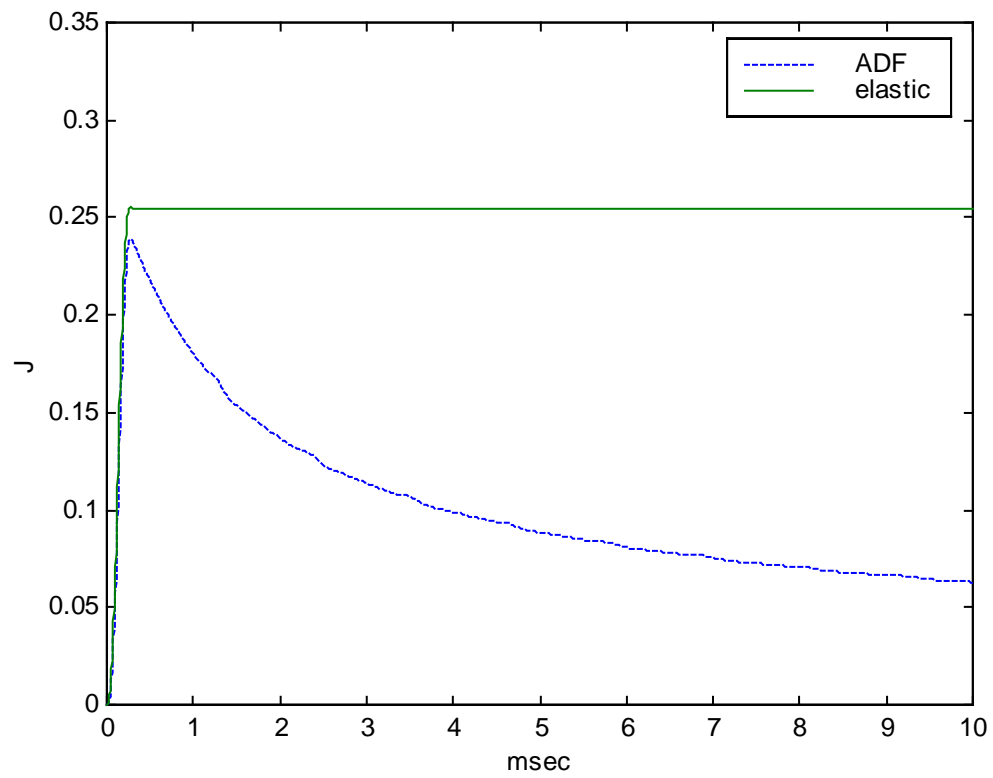


Figure 3.20. Time record of mechanical energy predicted by the axisymmetric ADF and elastic FEM, respectively

### 3.2.4. Numerical study of longitudinal wave propagation along split Hopkinson bar

In this section, the longitudinal wave propagation along a split Hopkinson bar is studied. The bar, made of two equal length segments of titanium and PERSPEX<sup>TM</sup>, is 2.4 m long and has a 1.9-cm diameter. The time step chosen is 1 millisecond and the triangular axisymmetric ADF FEM grid, representatively shown in Figure 3.21., has 200 nodes.

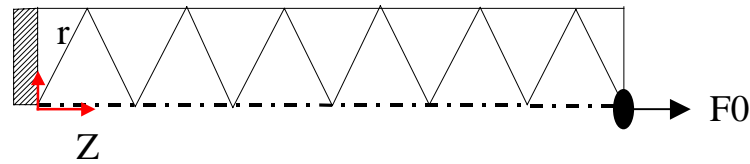


Figure 3.21. Axisymmetric grid

The longitudinal wave is generated by a 1000 N, half-sine force with a frequency of 3.33 kHz, shown in Figure 3.22., acting at the free end of the PERSPEX<sup>TM</sup> segment. The force  $F_0$  is applied at the center of the bar, as shown in Figure 3.21. The time step and element length ensure proper representation of frequency components in the force pulse.

Figure 3.23. shows the velocity profile along the bar after 100, 200 and 300 time steps. After the interface is encountered, part of the stress pulse is transmitted in the titanium bar, while most of it is reflected back in the PERSPEX bar due to the impedance mismatch between the segments of rod. In Figure 3.24., the particle velocity along the bar is shown just as the pulse is beginning to reach the interface between the two materials. Figure 3.25. shows that after a few reflections, two stress-waves, travelling in opposite directions, appear on the PERSPEX<sup>TM</sup> side of the bar. This is explained by the fact that the velocity of sound in titanium is higher than that in PERSPEX<sup>TM</sup>. Also, the attenuation of the stress pulse as it travels along the PERSPEX<sup>TM</sup> bar is clearly seen. Figure 3.26. and Figure 3.27. show the longitudinal displacement corresponding to the time instances of Figure 3.23. and Figure 3.25. Finally, Figure 3.28. shows the displacement record at both free ends of the Hopkinson bar. Figure 3.29. shows the

mechanical energy, which is the sum of the strain and the kinetic energies, in the split bar as a function of time. Note that in Figure 3.28. the displacement time record of the split bar's PERSPEX free end does not follow the usual step change pattern observed previously for a single material bar. It periodically increases and decreases (although slightly growing on the average), as a function of the sign and magnitude of the particle velocity. If the impedance of the boundary were infinite, the displacement at the free end of the bar would have cyclically increased and decreased around a zero average value.

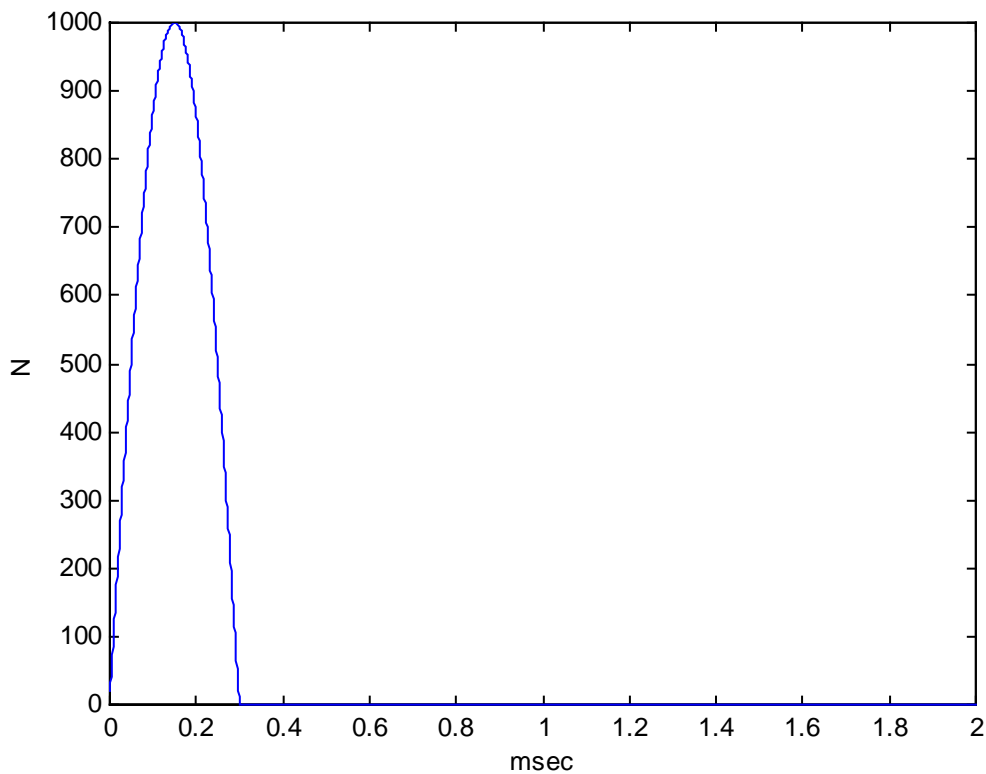


Figure 3.22. Force acting on free end of split Hopkinson bar

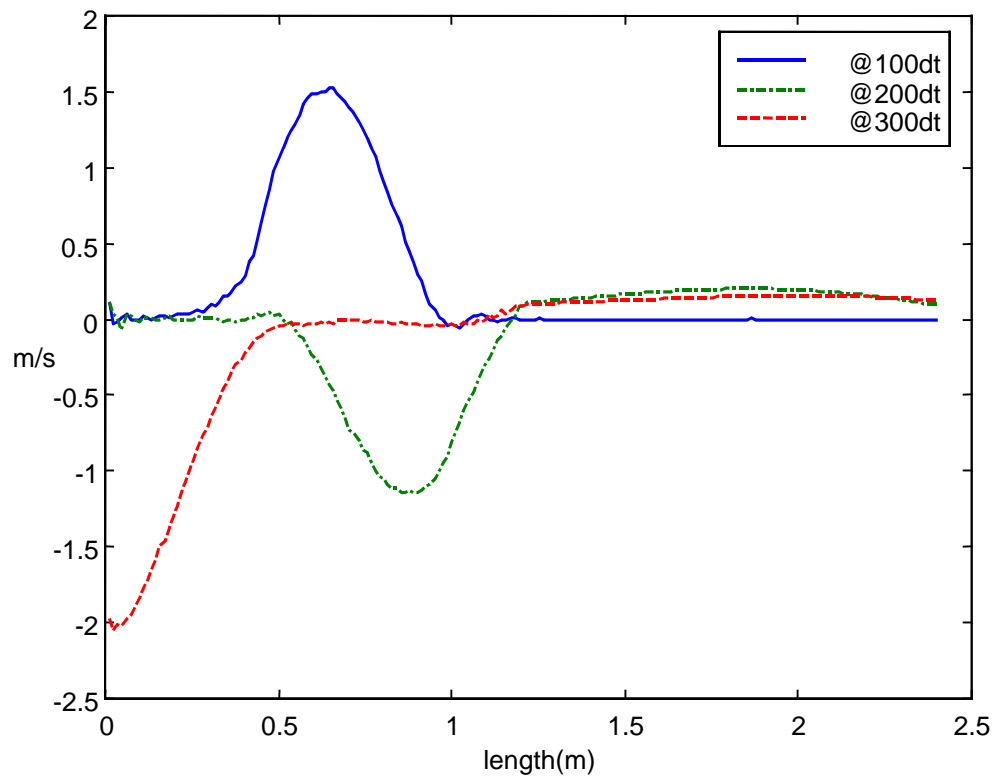


Figure 3.23. Particle velocity at various time instances

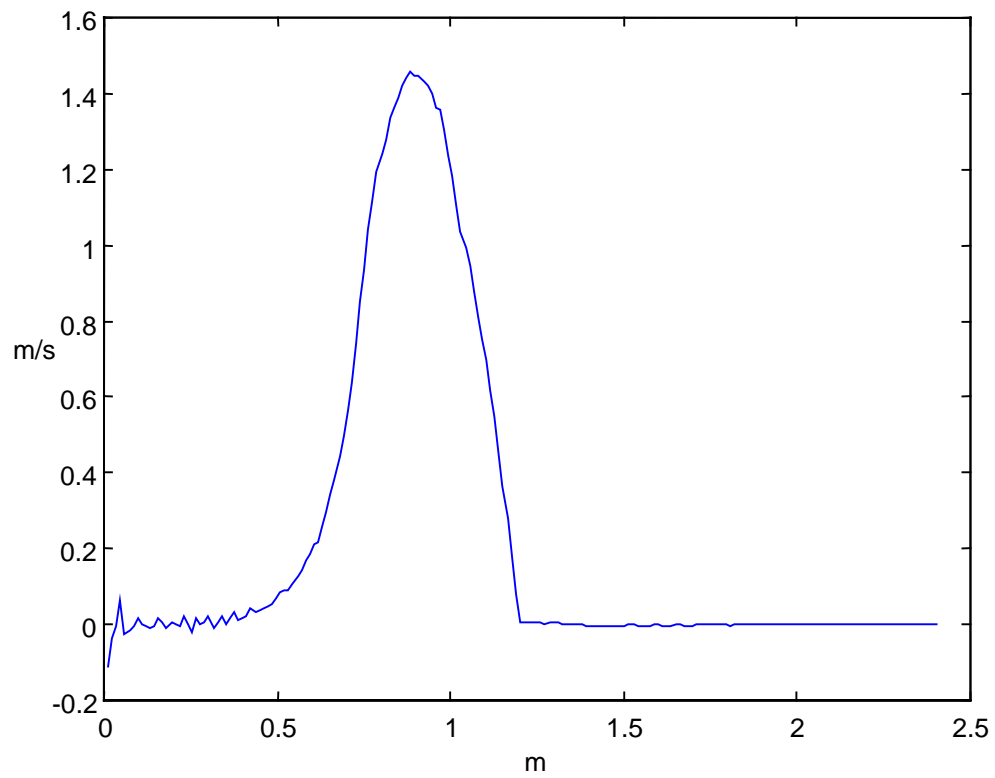


Figure 3.24. Particle velocity as the pulse hits the boundary (0.65 msec. after impact )

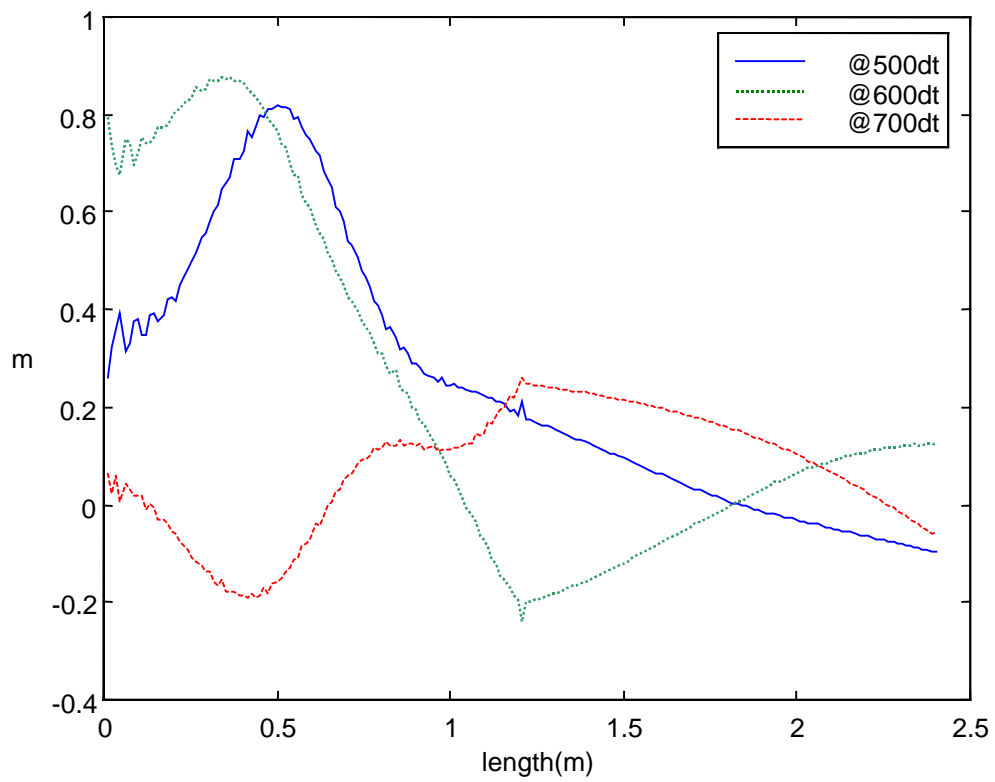


Figure 3.25. Particle velocity along bar at various instances

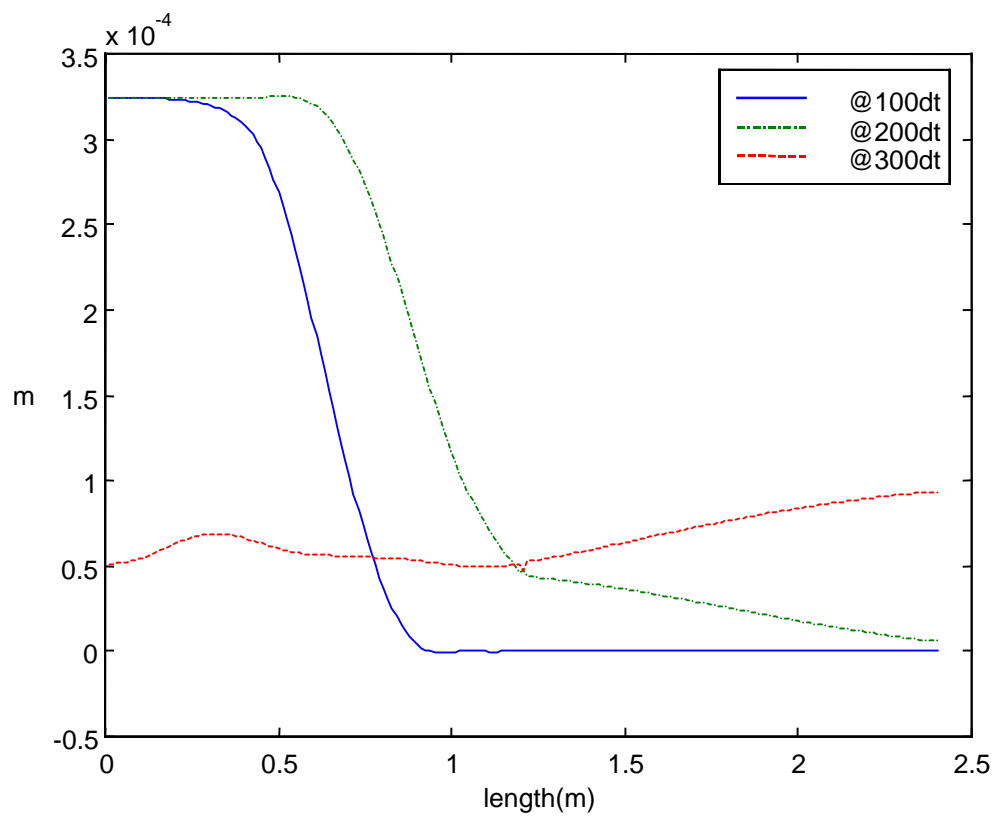


Figure 3.26. Longitudinal displacement along bar at various instances

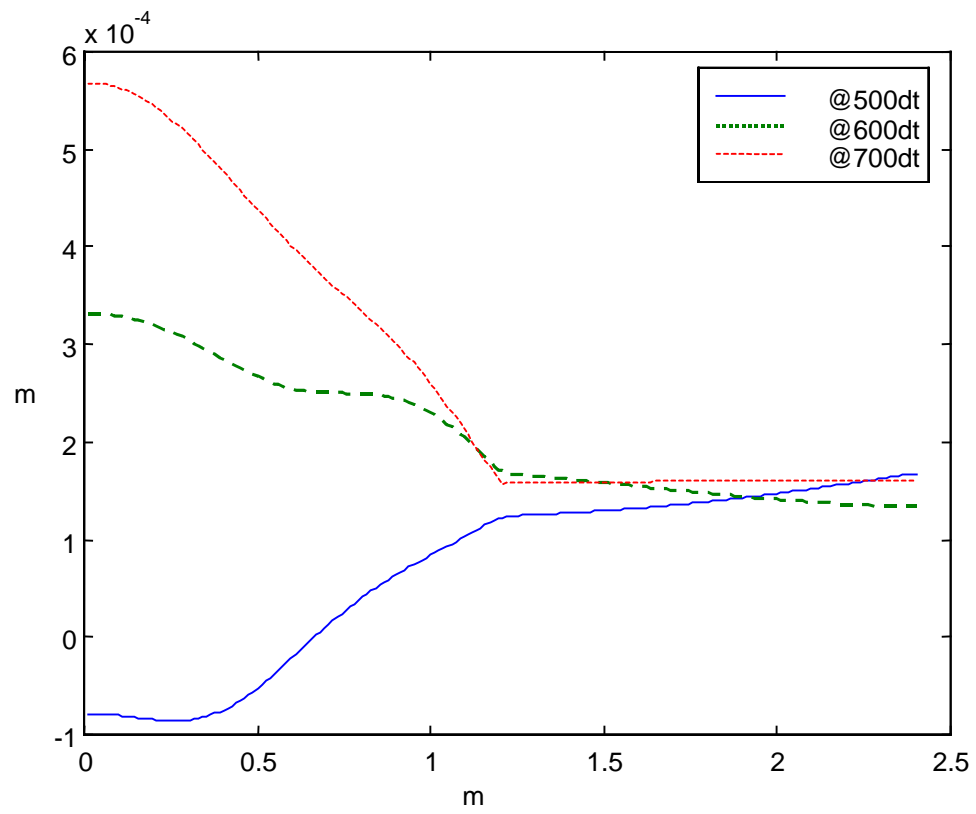


Figure 3.27. Longitudinal displacement along bar at various instances



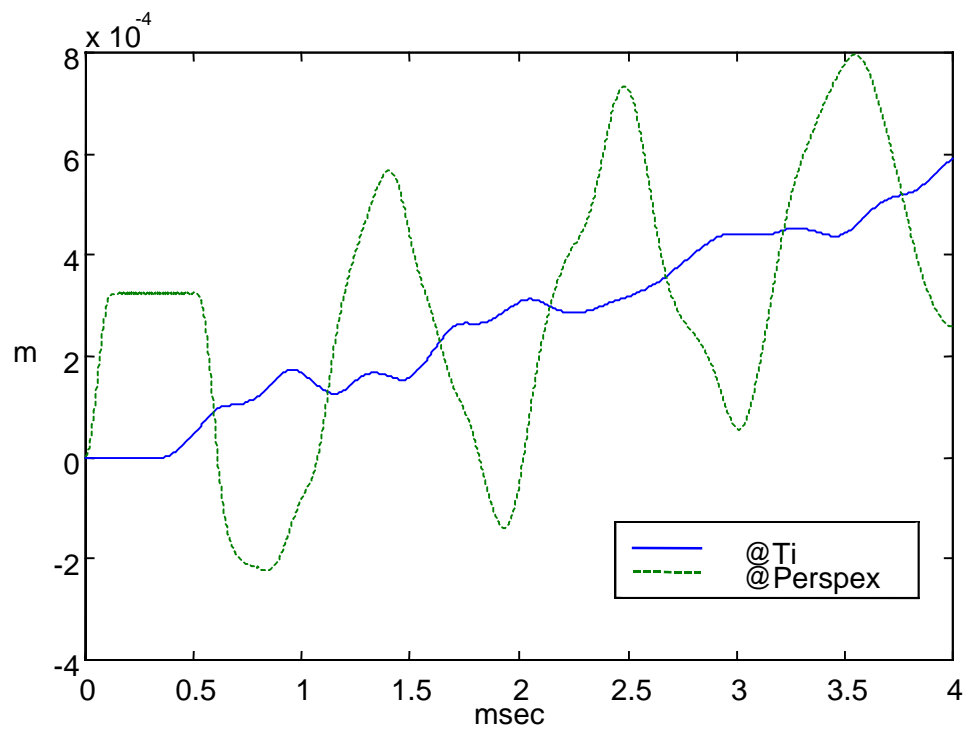


Figure 3.28. Longitudinal displacement time record at bar ends

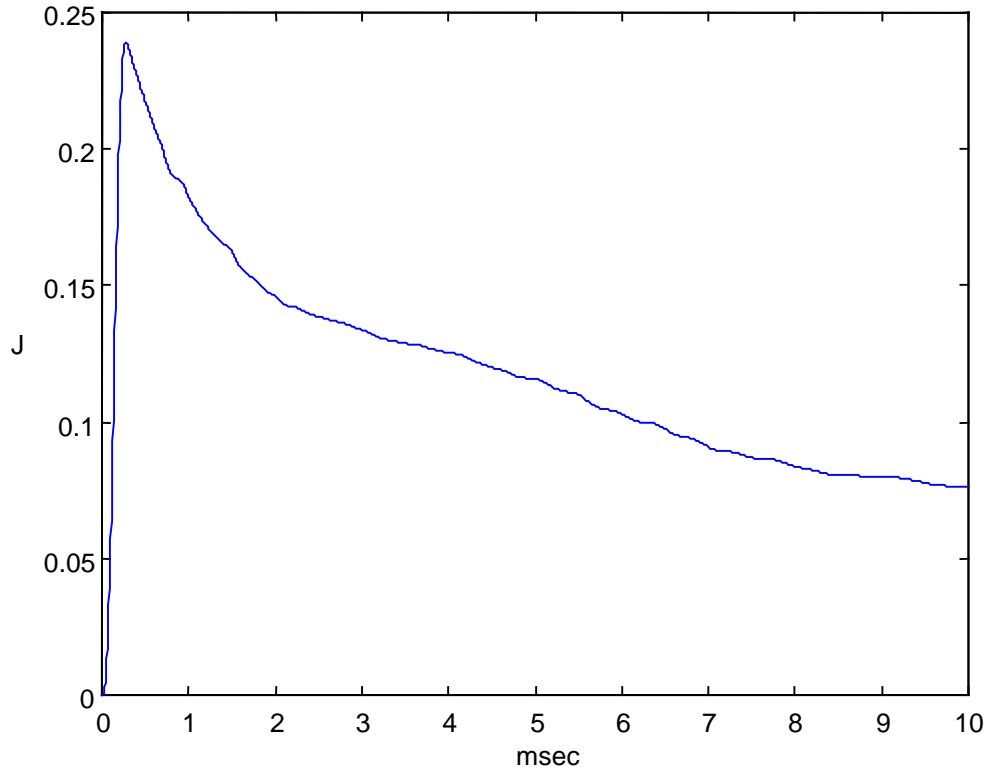


Figure 3.29. Mechanical energy in Hopkinson bar vs. time

### 3.2.5. Modeling of geometrical dispersion in a Perspex™ bar

Another phenomenon encountered in longitudinal wave propagation along bars is geometric dispersion. Geometric dispersion occurs when the diameter of the bar is on the same order of magnitude or longer as the wavelength of frequency components contained in the stress pulse. The stress pulse is dispersed as a result of the effect of lateral inertia. Geometric dispersion causes high frequency pulse components to travel slower than lower frequency pulse components [39]. As a result, high-frequency oscillations follow the displacement step pulse associated with longitudinal wave propagation along bars. These high-frequency oscillations that followed a step displacement pulse, indicative of geometric dispersion, were recorded and published by Kolsky [39].

In the numerical simulations considered, a free-free PERSPEX<sup>TM</sup> bar is hit at one end by a half sine force of 1368 N magnitude and 4.35 kHz central frequency. In one simulation the bar has a 15-cm diameter, and in the other simulation the bar has a 1.5-cm diameter. The bar is 1.8 m long. The FE mesh that models the bar, shown in Figure 3.21., has 200 nodes and the element length is 0.75 cm. A single-ADF, triangular, axisymmetric FE is used. The time step chosen is 2.5 microseconds. This numerical arrangement allows good modeling of frequency components of up to 14.5 kHz in the response. Pulse dispersion is expected in the 15-cm diameter bar, since the wavelength corresponding to a 14.5 kHz frequency is on the same order of magnitude as the larger diameter.

Figure 3.30. compares the predicted bar end displacements for the two simulations. Each end displacement is normalized to its maximum value. The two bars have different masses, but the same force acts upon them: as a result, the magnitudes of the corresponding end displacements are different. Note in Figure 3.30. that a series of high-frequency oscillations follow each sharp rise of the end displacement corresponding to the 15-cm diameter bar, which are the effects of geometrical dispersion. Note that geometrical dispersion effects are not observable in the end displacement of the smaller diameter bar. The effects of viscoelastic attenuation are present in both displacement traces and are represented by slope changes in the displacement time record. Figure 3.31. shows the mechanical energy in the 15-cm bar, which is the sum of the kinetic and strain energies. The strain energy component decays and the mechanical energy reaches asymptotically towards the constant-velocity kinetic energy of the bar.

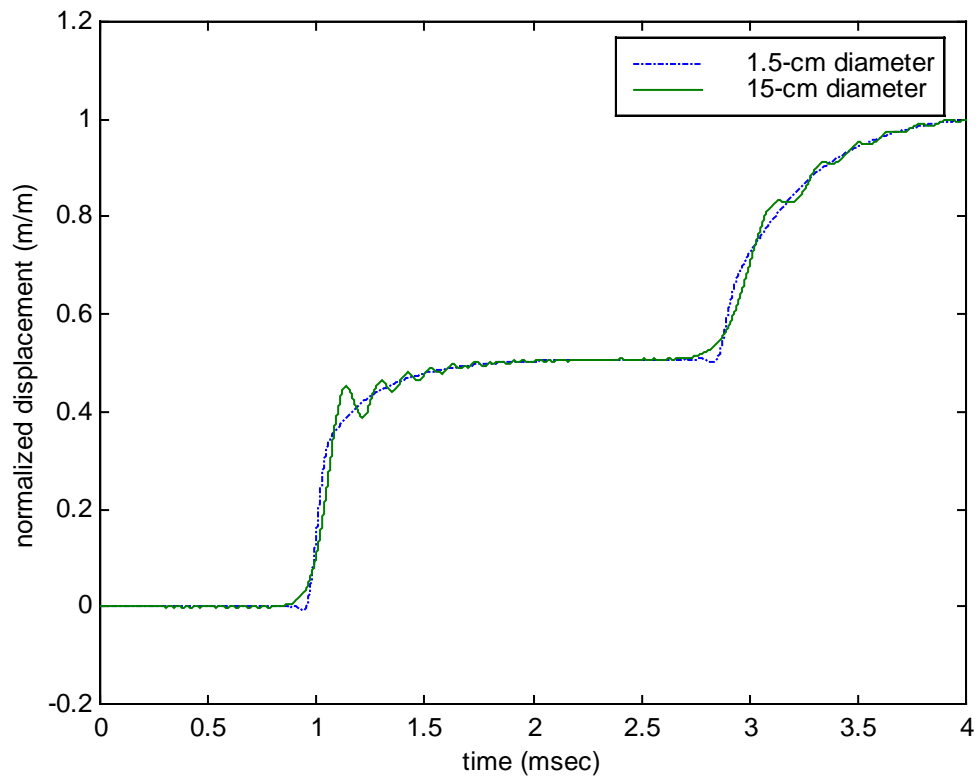


Figure 3.30. Dispersion: comparison of normalized end displacement at end of two PERSPEX<sup>TM</sup> bars

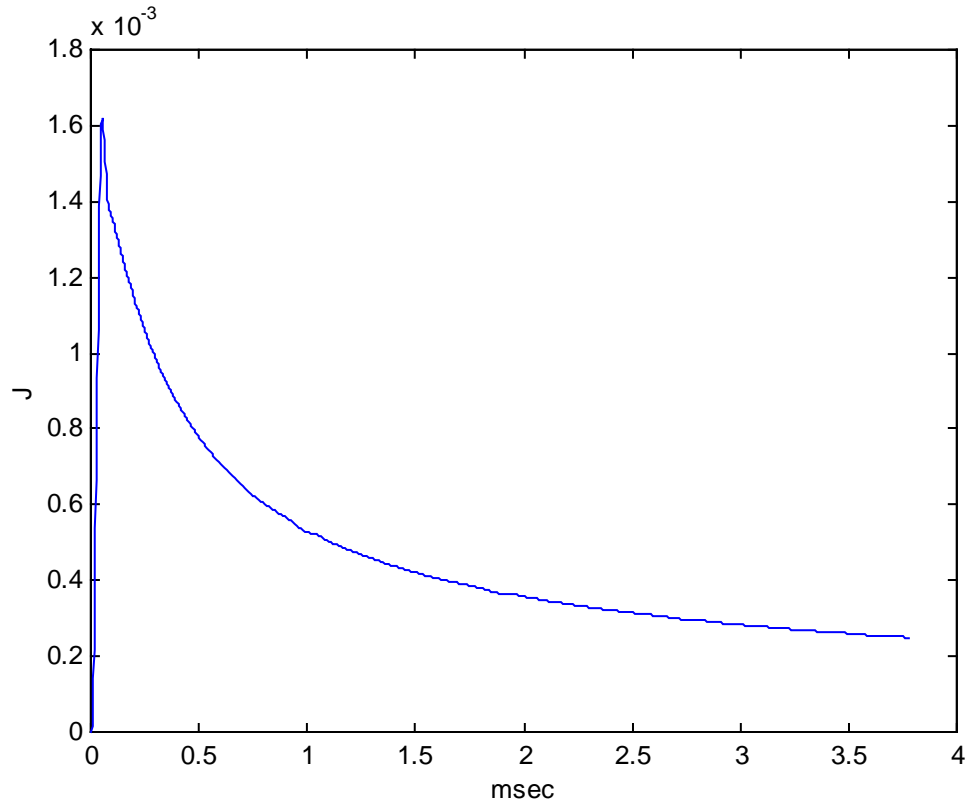


Figure 3.31. Mechanical energy in 15-cm diameter bar vs. time

### 3.2.6. Modeling of longitudinal wave propagation through an elastic bar with mechanical filter and mass at end

The next numerical case investigates the behavior of a shock accelerometer placed on an elastic Hopkinson bar. A mechanical filter, of 6.25-mm thickness, made of a hypothetical viscoelastic material ( $E_f=4.7e10$  Pa), in series with a mass of 29.2 grams models the shock accelerometer. Two analysis cases are considered, corresponding to different mechanical filter loss factors. In the first case, the peak loss factor is 0.98; in the second case, it is 0.46, corresponding to a frequency of 3.33 kHz. The FEM mesh for both filter and bar is represented by the mesh shown in shown in Figure 3.21. and consists of 200 nodes: 100 nodes for the filter and 100 for the bar. The bar is modeled with elastic, triangular, axisymmetric FE and the filter is modeled with single-ADF, triangular, axisymmetric FE. The one-meter-long Hopkinson bar is impacted at one free end by a

half-sine force of 1000 N and 3.33 kHz central frequency. The ADF relaxation magnitude and inverse of relaxation time are obtained through Equation (2.109) and Equation (2.110), respectively, and are presented in Table 3.5. Both the bar and the mechanical filter have a diameter of 0.75 inches. The time step chosen is 2 microseconds.

Figure 3.32. shows the difference in the displacement of the mass and that of the end of the bar. While the displacement steps at the end of the bar are sharp, the displacement steps at the mass location are more rounded. The displacement steps at the mass location decrease slightly in magnitude as time progresses, since the influence of the filter is relatively small on the energy dissipation in the bar. Figure 3.34. shows that while the velocity on the bar changes little in magnitude (decreases by 6% from the start to the end of the record), the velocity of the mass does not return to zero after the shock pulse passes. That is because the incoming pulses keep hitting it before it has time to fully relax. In Figure 3.33., the velocity shift after 3.8 milliseconds is 0.05 m/s, which represents 25% of the peak velocity value at 3.5 milliseconds. Figure 3.35. shows a comparison of the mass displacement predicted for the low- and high-loss filters.

Table 3.5. Material parameters for viscoelastic material

Peak Loss Factor $\eta_p$	Relaxation Strength $\Delta$	Inverse of Relaxation Time $\Omega$ (rad/s)
0.46	1.46	32820
0.96	4.58	49424

If the mass is mounted on the filter with the higher loss factor, the velocity and displacement are smaller.

The attenuation of the displacement is more pronounced when the longitudinal wave passes through the filter with higher loss factor. Figures 3.36. and 3.37. show the velocity time record and the displacement time records of the bar's end. The velocity and

displacement at the end of the bar with the higher loss filter are slightly smaller and this effect accentuates in time. In Figure 3.38., the mechanical energy of the bar/low-loss filter system is decreasing slower than that of the bar/high-loss filter system.

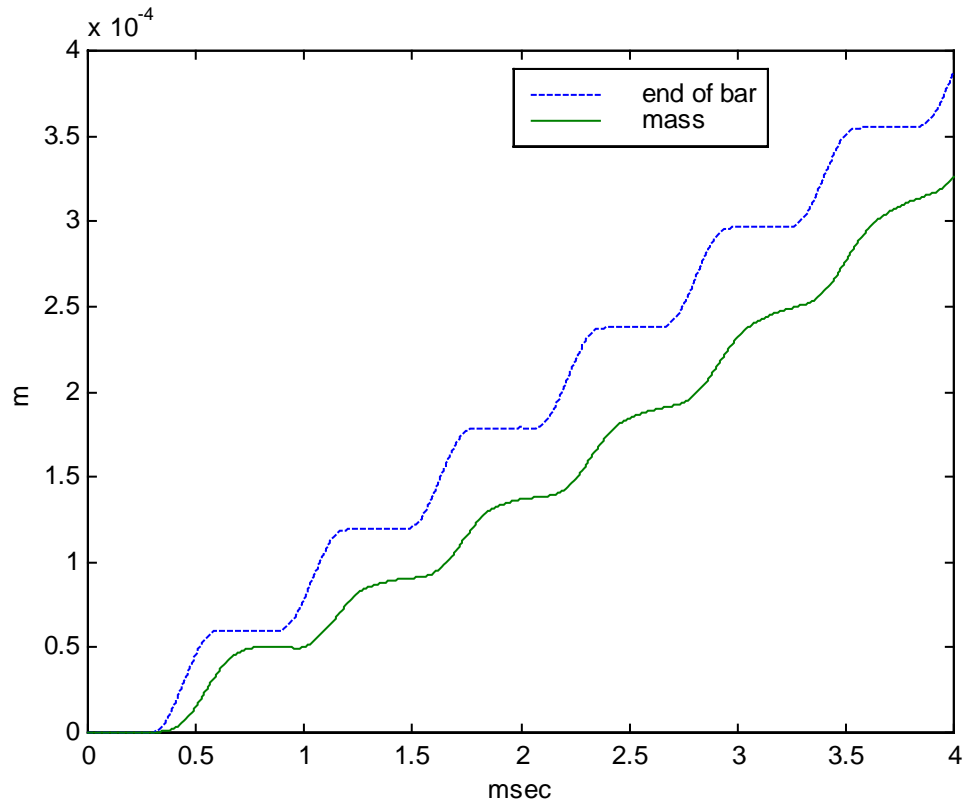


Figure 3.32. Time record of displacement at bar's end and at mass

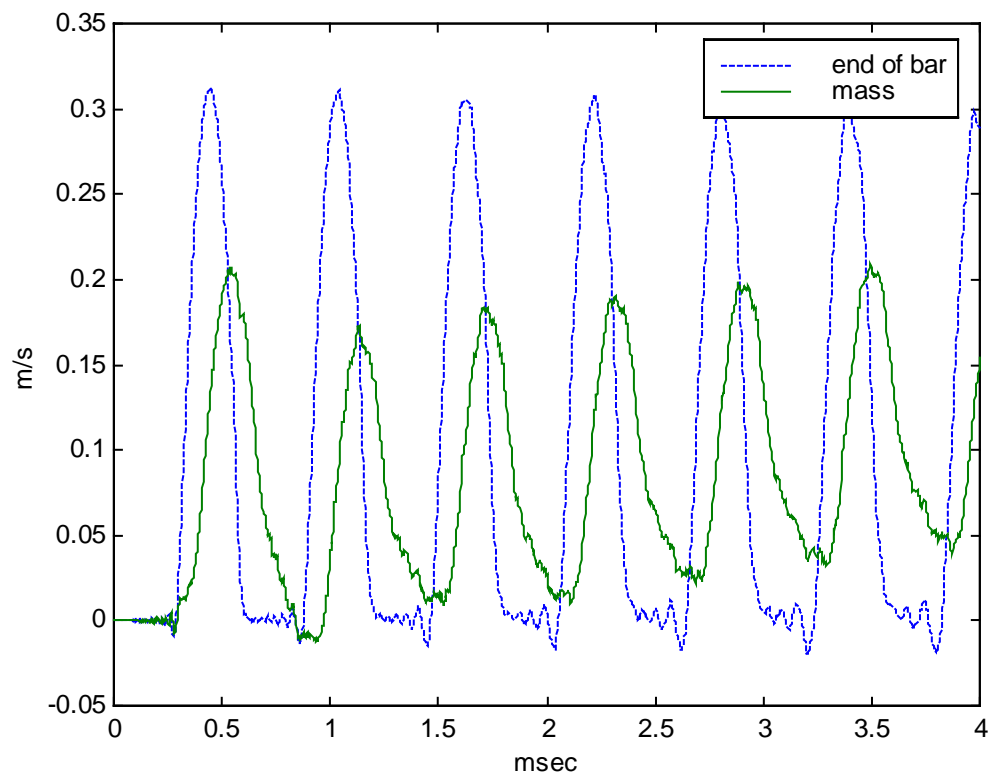


Figure 3.33. Particle velocity of end of bar and of mass



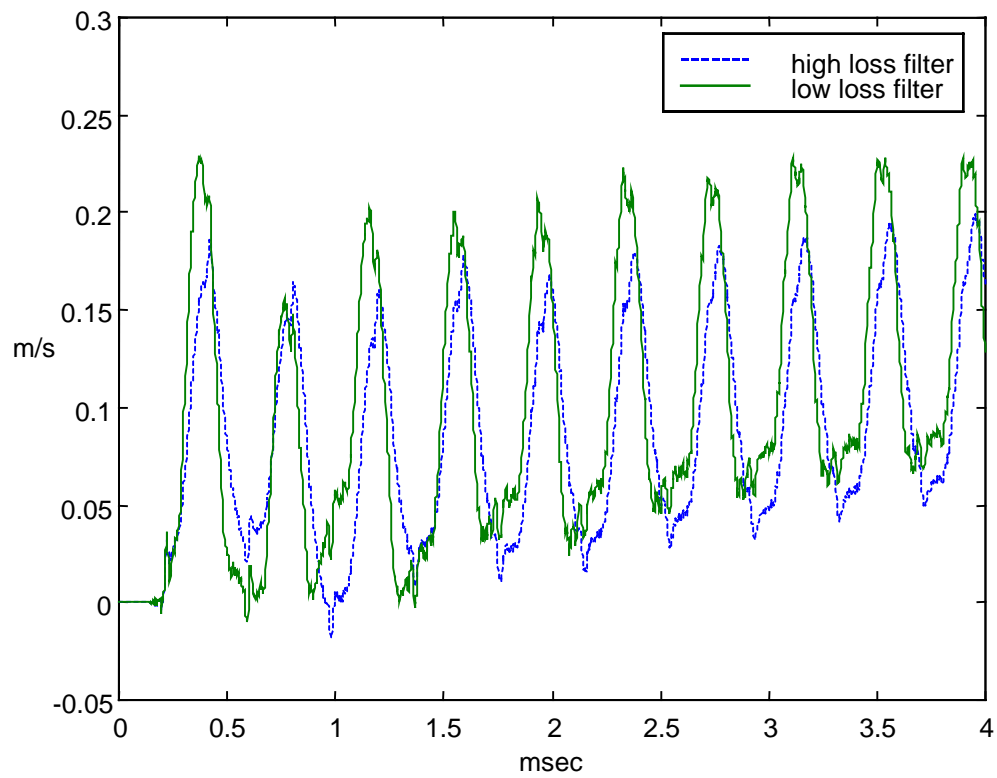


Figure 3.34. Velocity of mass: low loss and high loss filters

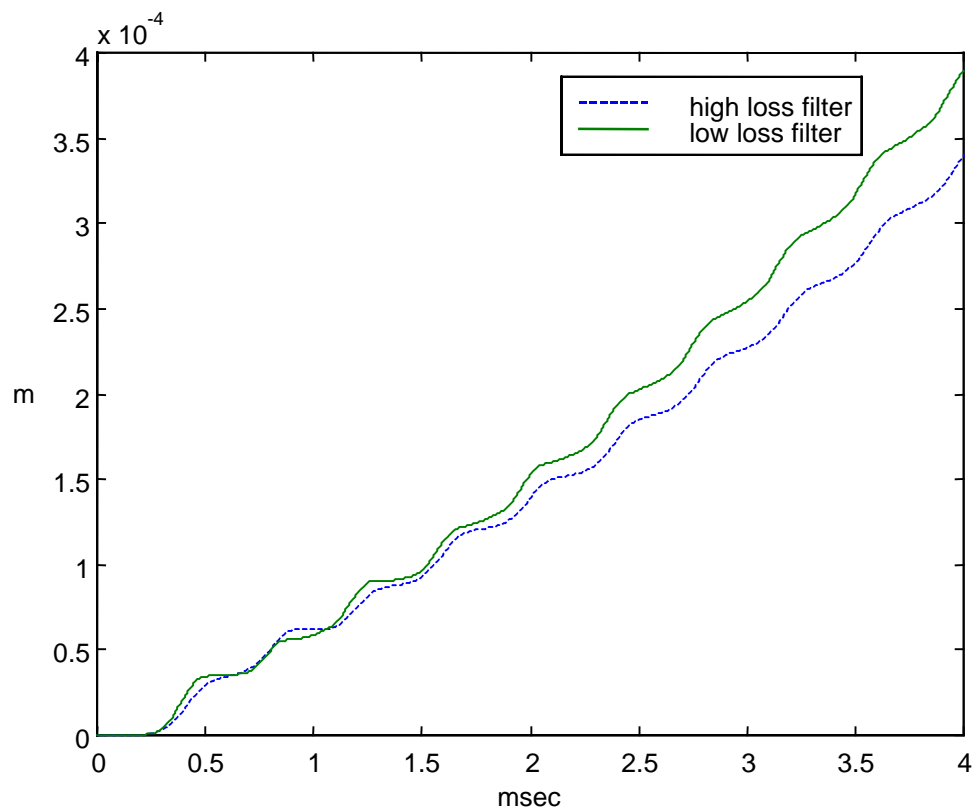


Figure 3.35. Displacement of mass: low loss and high loss filters

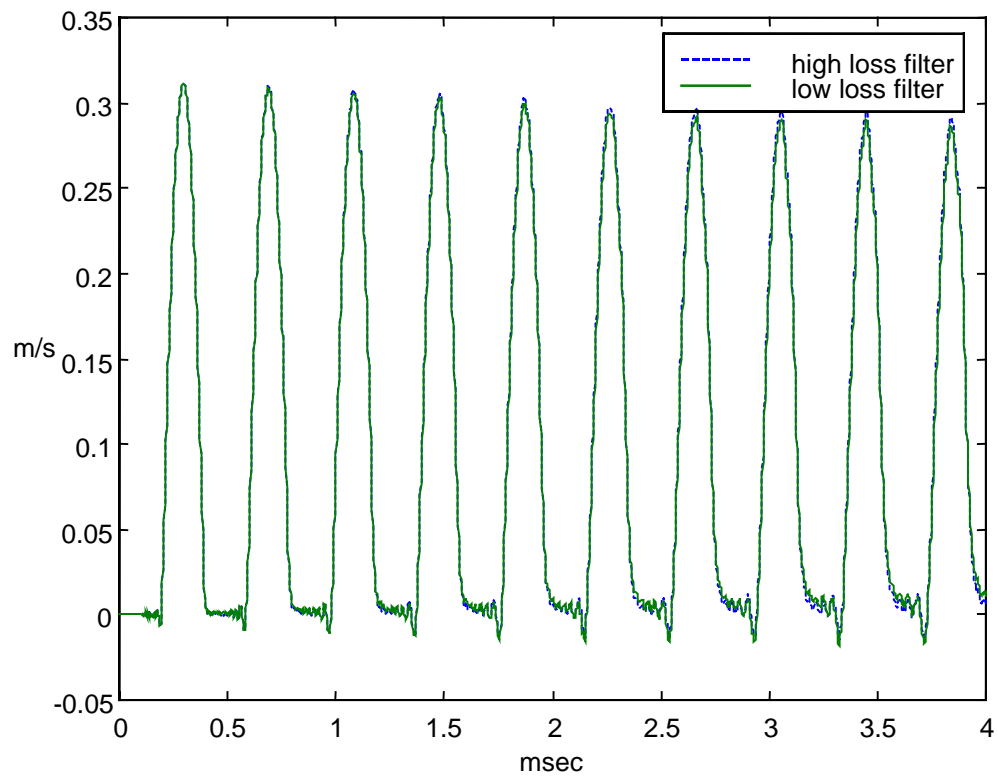


Figure 3.36. Velocity at bar end vs. time: low loss and high loss factor filters

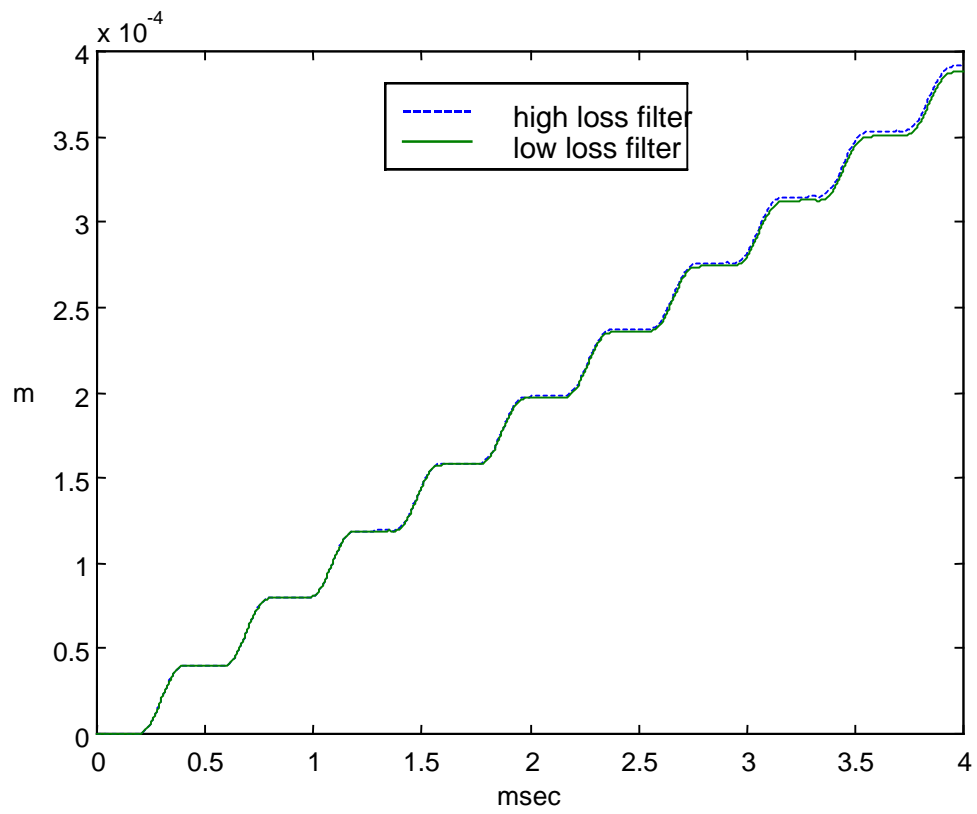


Figure 3.37. Displacement at end of bar: low loss and high loss filters

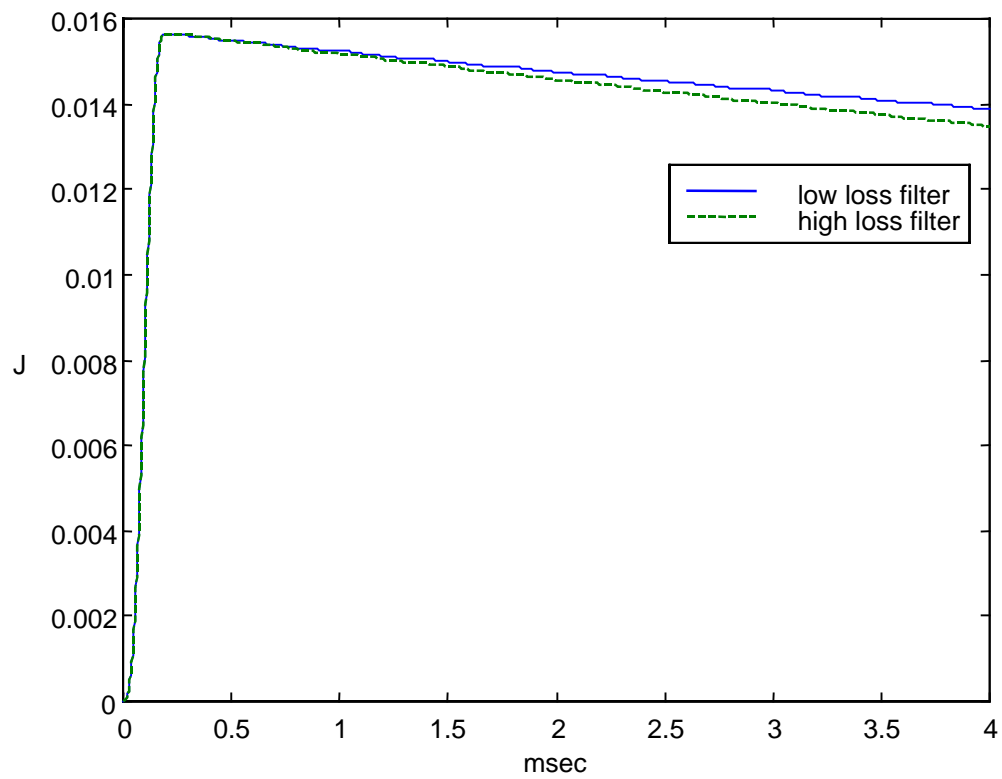


Figure 3.38. Energy in system vs. time

### 3.3. Comparison of finite element results to experimental results

This section compares results obtained with ADF axisymmetric FEM to experimental results. The behavior of various structures under shock loads is investigated. The structures are comprised of materials with either weak or strong frequency dependencies.

#### 3.3.1. ADF modeling of mechanical filters subjected to shock and comparison to experiments

This section investigates the ability of ADF axisymmetric FE to model shock behavior of structures consisting of materials with high-loss factors.

Two similar simple mechanical filters are investigated, each comprising a 3.5-mm-thick and 25.4-mm-diameter tungsten disk glued to a variable thickness and 25.4-mm-diameter Buna N rubber (nitrile rubber) Durometer 60 disk (see Table 3.6. for nitrile rubber material information). The thickness of the filter is in the first case 3.5 mm, and in the second experiment 7.0 mm.

Table 3.6. Material parameters for Buna N rubber Durometer 60

Density(kg/m <sup>3</sup> )	Relaxed shear modulus (Pa)	Young's modulus (Pa)	Poisson's ratio
1280	1.26e6	4.2e6	0.495

An accelerometer (PCB 305A05 accelerometer S/N 9998, 1.8 mV/g sensitivity) is attached to the tungsten disk. The filter is dropped, viscoelastic disk first, on a force gauge (PCB 208B05, 1.05mV/lb sensitivity), as shown in Figure 3.39.

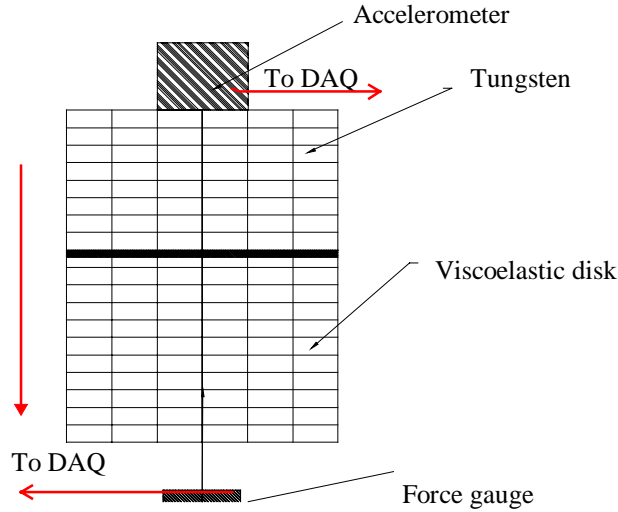


Figure 3.39. Drop test

Both the accelerometer and the force gauge signals are recorded and processed using a LABVIEW<sup>TM</sup> code developed by the author. The force signal is then used as input to a five-ADF axisymmetric finite element code. The experimental acceleration, velocity, and displacement signals are then compared to the predicted acceleration, velocity, and displacement signals. The finite element mesh used is represented schematically in Figure 3.39.: 4 rows with 15 nodes each for the viscoelastic material, and 4 rows with 4 nodes each for the tungsten disk.

The frequency range of interest is chosen to coincide with the frequency band over which the input pulse power spectrum has most of its energy distributed. Note that the properties of Buna N rubber vary widely with the manufacturer. The current moduli vs. frequency data of Buna N rubber is obtained from Nashif and Jones [9], for a temperature of approximately 10<sup>0</sup>C, although the experiments are conducted at room temperature (23<sup>0</sup>C). The ADF parameters are obtained from a least-square curve-fitting subroutine developed at Penn State. The ADF parameters are then adjusted so that predicted quantities match the experiment. The new ADF parameters are then re-verified against the new experimental case, i.e. the mechanical filter with 7.0-mm thickness. Figure 3.40. shows the loss factor and storage moduli of Buna N rubber Durometer 60 versus the

adjusted five-ADF model curve-fit. The ADF parameters used to model the frequency-dependent material properties of Buna N rubber are shown in Table 3.7.; these parameters are used as input in all numerical studies.

Table 3.7. ADF parameters used (5 ADF) for Buna N rubber

Parameter	1	2	3	4	5
$\Omega(\text{rad/s})$	1E2	5E2	1E3	3E3	1E4
$\Delta_G^*$	0.05	0.1	0.2	1	5

\* $\Delta_G = \Delta_K$ ; the relaxation strengths of the shear and bulk modulus, respectively, are equal.

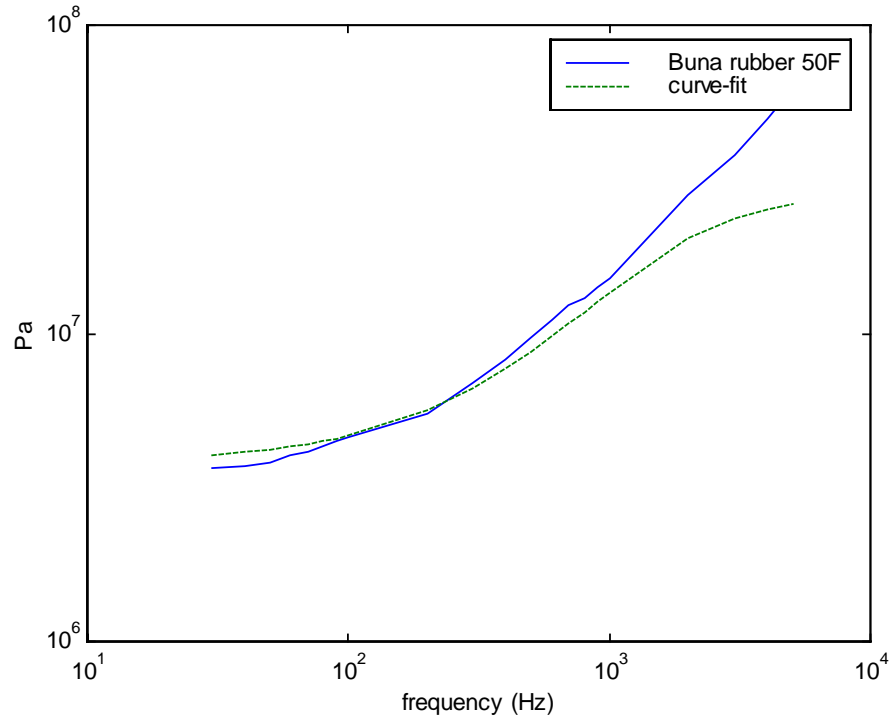


Figure 3.40 (a). ADF curve-fit of storage modulus



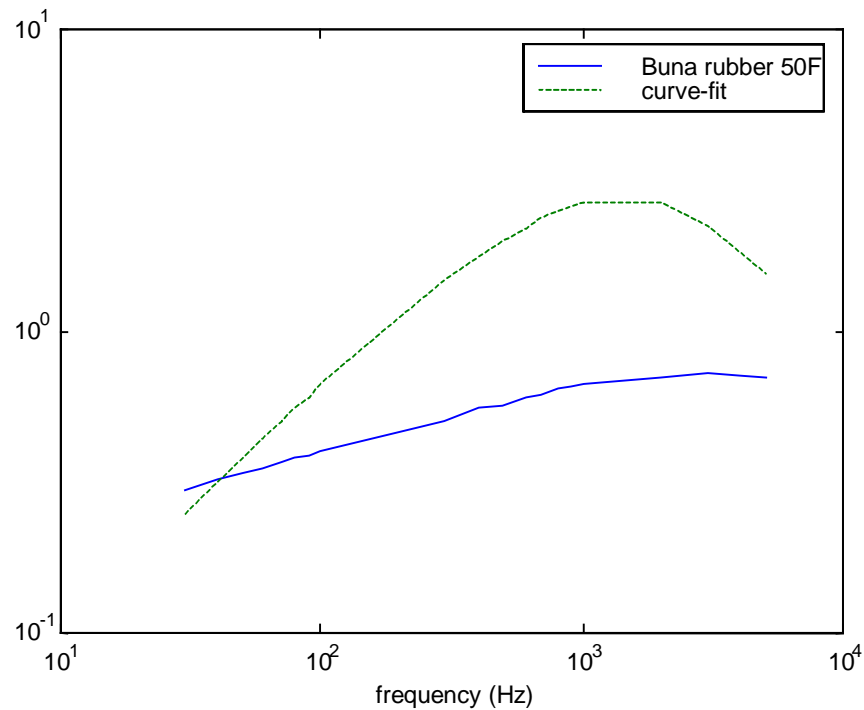


Figure 3.40 (b). ADF curve-fit of loss factor

#### 3.3.1.1. Mechanical filter with 3.5-mm-thick Buna N 60 Durometer rubber layer

The first mechanical filter built has a rubber layer with 3.5-mm thickness. Figure 3.41. shows the input force, which has an almost half sine shape, with the front of the pulse steeper than the tail. The rise time of the force is approximately 0.3 milliseconds. Figure 3.42. shows the input force power spectrum (DC power spectrum value is reference). The highest density of the power spectrum occurs between 0 to 1 kHz (as shown in Figure 3.42.); the ADF model predicts well the material properties in that frequency range. Figure 3.43. shows the predicted displacement on the top of the filter versus the experimental displacement (obtained by integrating twice the acceleration signal). The agreement of the predicted displacement traces to the experiment is within 2% relative error. The shape of the displacement trace closely resembles the theoretical displacement time history associated with a half-sine pulse [53]. Figure 3.44. shows the predicted velocity at the end versus the experimental velocity obtained by integrating the acceleration signal.

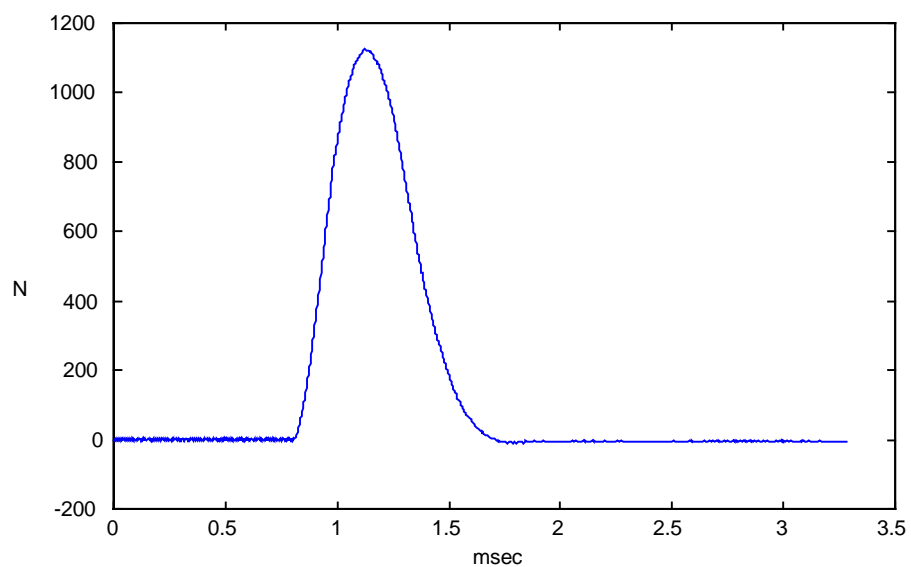


Figure 3.41. Force input for filter with 3.5-mm rubber layer

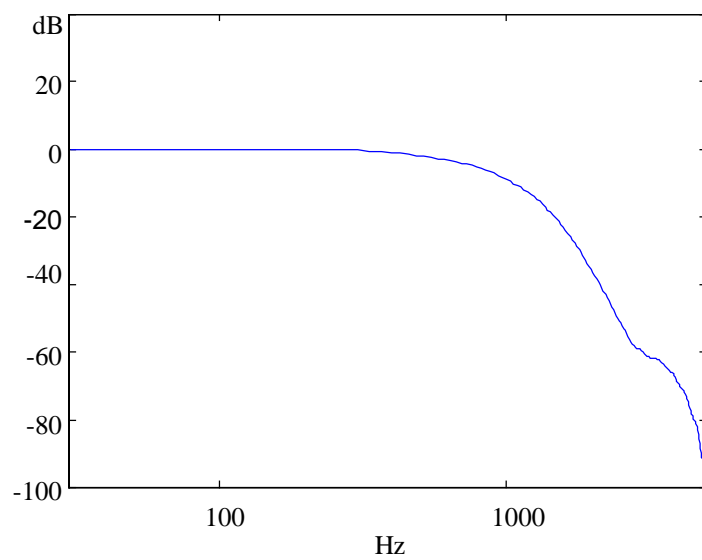


Figure 3.42. Force power spectrum for filter with 3.5-mm rubber layer

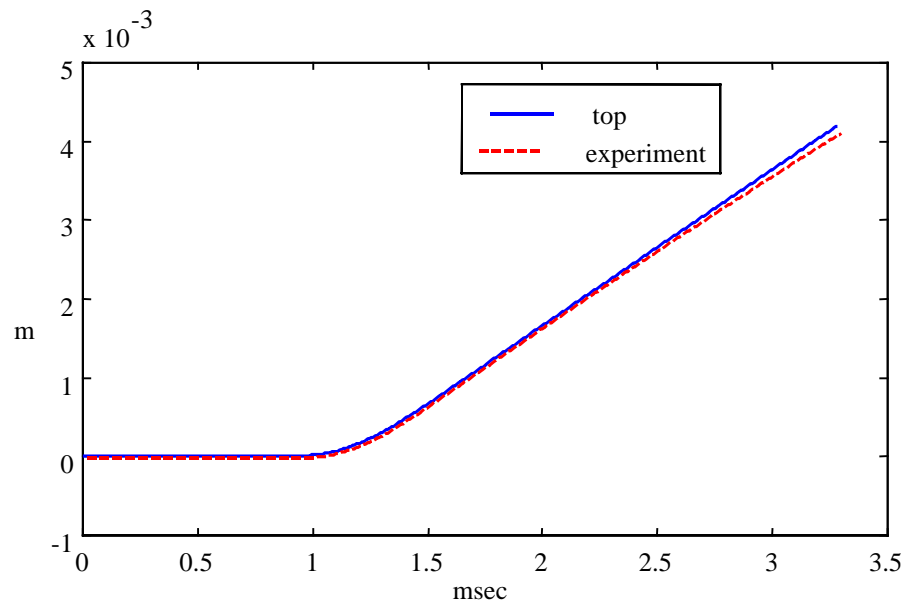


Figure 3.43. Predicted vs. experimental displacement for filter with 3.5-mm rubber layer

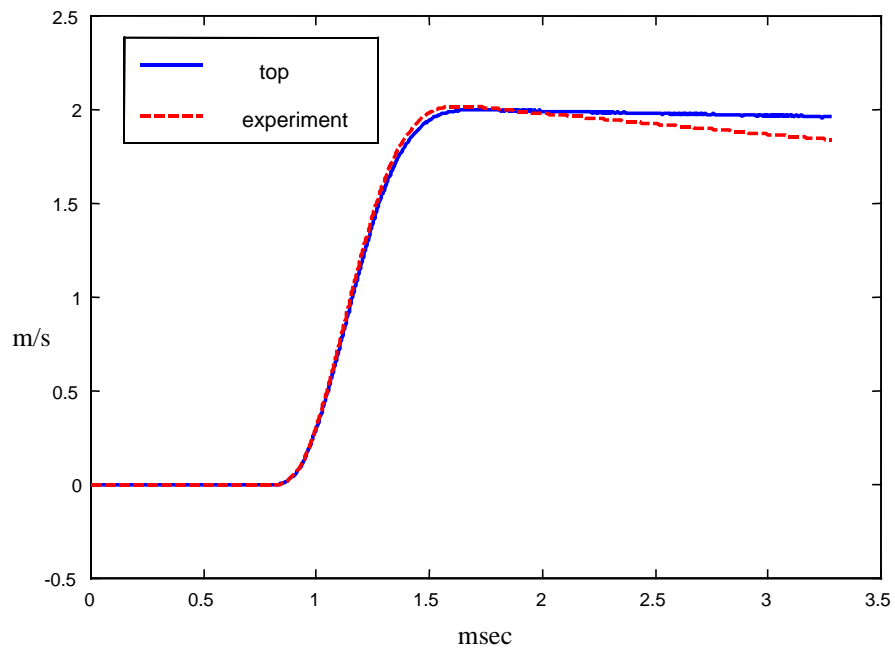


Figure 3.44. Predicted velocity vs. experiment, for filter with 3.5-mm thick rubber layer

The agreement of the predicted traces to the experiment is within 10% relative error (at the end of the record) for the first two milliseconds of the time record, after which, they start to diverge slightly from the experimental velocity. The predicted shape of the velocity trace resembles the shape of the velocity profile associated with a half-sine pulse. Figure 3.45. shows the predicted acceleration on the top of the filter versus the experimental acceleration. The agreement of the predictions to the experimental trace is good, with the exception of the high frequency components present in the ADF model. The high-frequency components appear damped lighter than in reality, because the ADF model only covers a limited frequency range and also due to the finite element grid size. It may be observed that the experimental acceleration exhibits a nonlinear feature called "zero shift": the acceleration does not return to zero after the impact is over, but it remains slightly negative as the rubber continues to recover slowly.

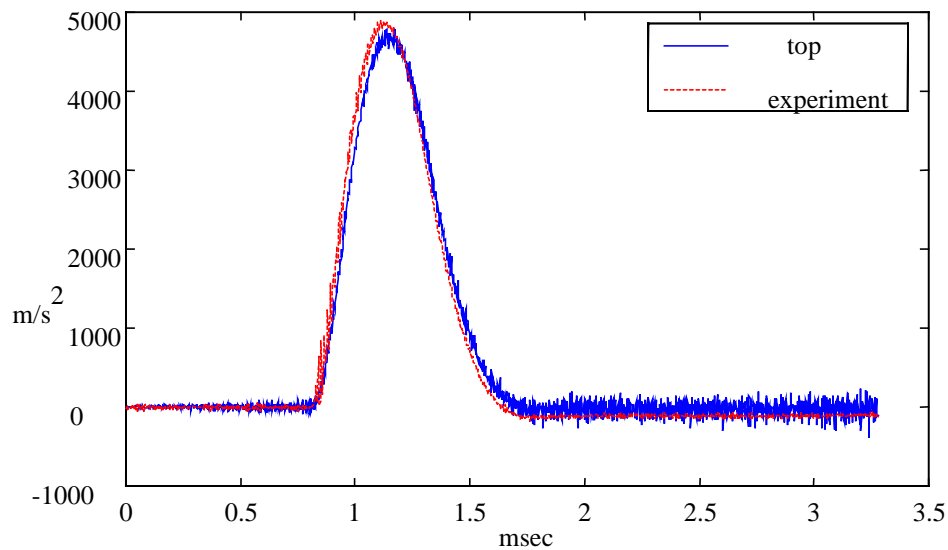


Figure 3.45. Predicted vs. experimental acceleration for filter with 3.5-mm rubber layer

Figure 3.46. shows the power spectrum of the input force versus the acceleration. The acceleration spectrum is well predicted to around 1 kHz, as shown in Figure 3.46.

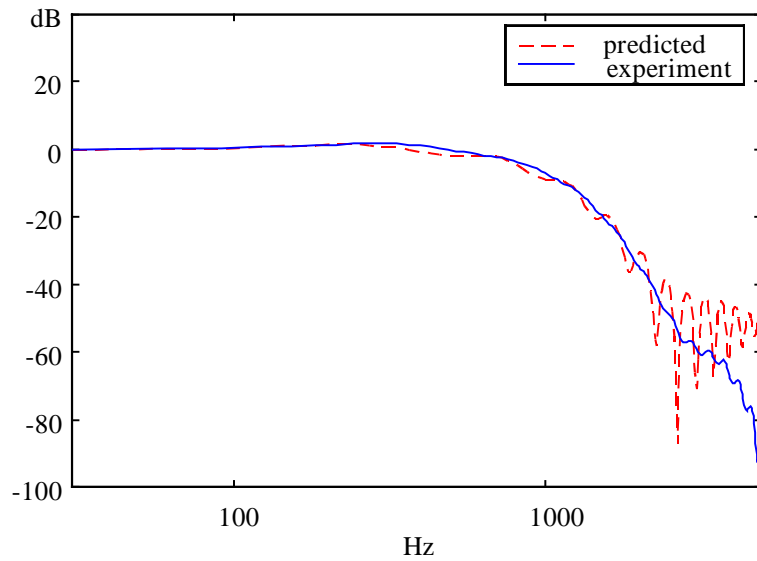


Figure 3.46. Experimental vs. predicted acceleration power spectrum

#### 3.3.1.2. Mechanical filter with 7-mm-thick Buna N 60 Durometer rubber layer

The second mechanical filter built has a rubber layer of 7-mm thickness. Figure 3.47. shows the input force. The input force rise time is approximately 0.4 milliseconds. Figure 3.48. shows the input force power spectrum normalized to its DC value. Figure 3.49. shows the predicted displacement on the top of the filter versus the experimental displacement. The prediction agrees within 5% with the experiment. Figure 3.50. shows the predicted velocity on the top of the filter vs. the experimental velocity. The agreement of the predicted traces to the experiment is within 5% relative error; the experimental velocity is slightly higher in magnitude. Figure 3.51. shows the predicted acceleration on the top of the filter vs. the experimental acceleration. The relative error of the predicted to the experimental trace is less than 10%, with the exception of the high frequency components present in the ADF model (caused by the size of the finite element mesh). A slight "zero shift" phenomenon may also be observed in the experimental trace. Figure 3.52. shows the normalized power spectrum (to its own DC value) of the input force vs. the acceleration. Again, the acceleration spectrum is well predicted to around 1 kHz.

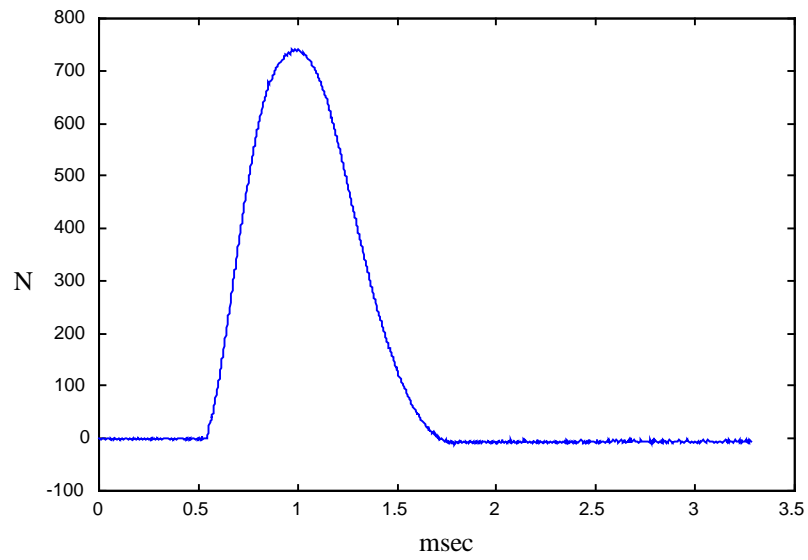


Figure 3.47. Force input for filter with 7-mm rubber layer

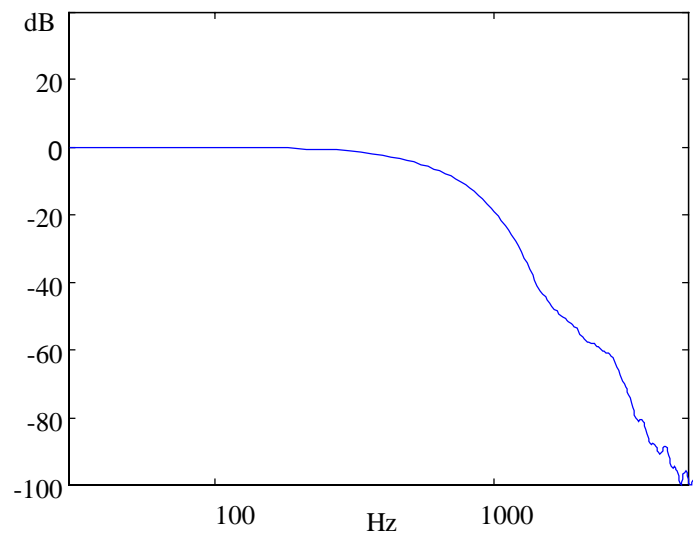


Figure 3.48. Input force power spectrum

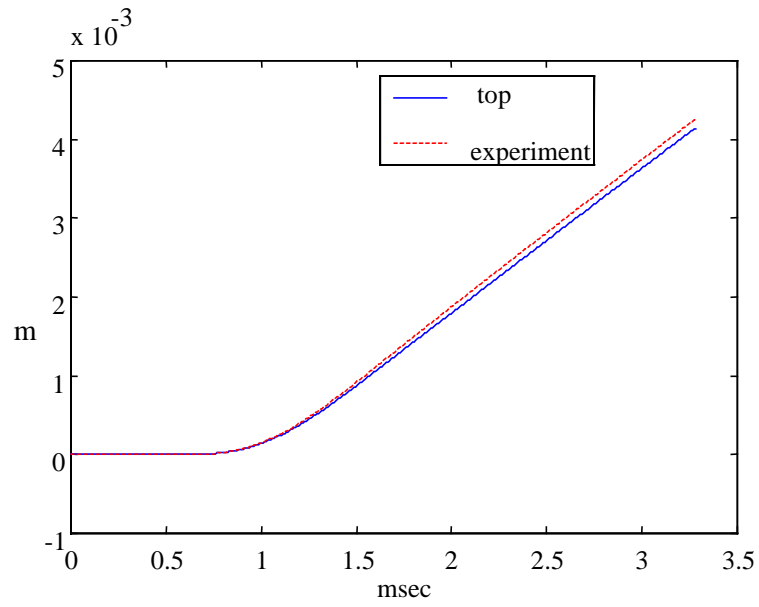


Figure 3.49. Predicted vs. experimental displacement for filter with 7-mm rubber layer

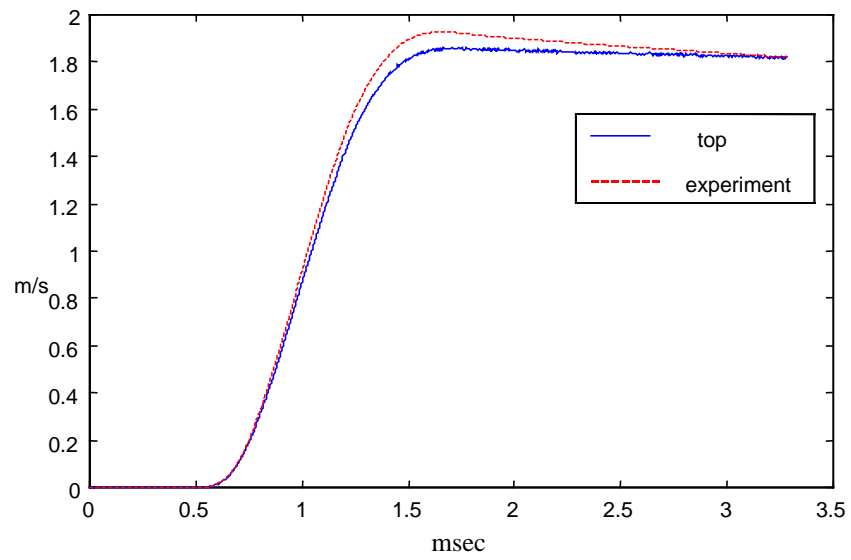


Figure 3.50. Predicted vs. experimental velocity for filter with 7-mm rubber layer

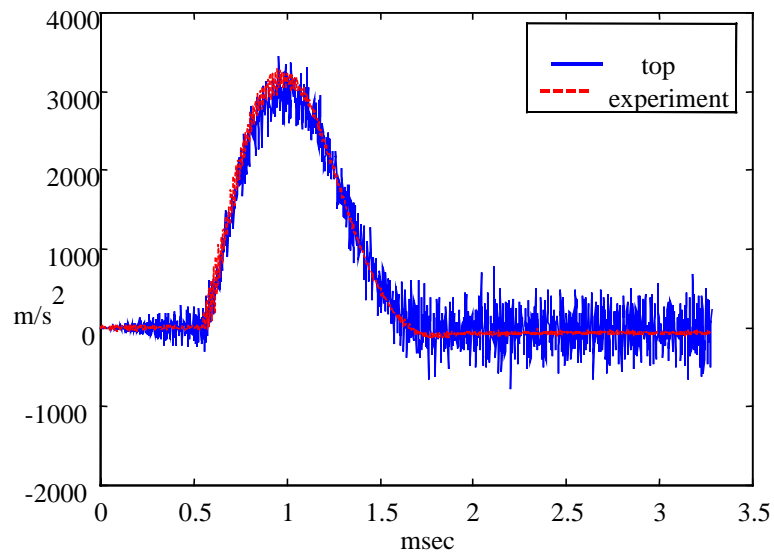


Figure 3.51. Predicted vs. experimental acceleration for filter with 7-mm rubber layer

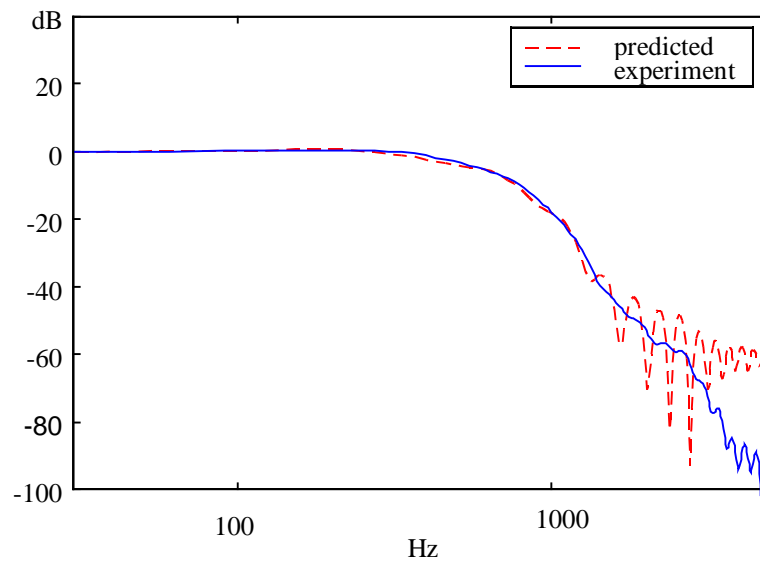


Figure 3.52. Experimental vs. predicted acceleration power spectrum, for filter with 7-mm rubber layer



### 3.3.2. Modeling of wave propagation through metal bars and comparison to experiments

The ability of ADF axisymmetric finite elements to model weakly frequency-dependent damping is researched next. The longitudinal wave propagation along a free-free titanium alloy Ti6Al4V bar is considered. The longitudinal wave is physically generated by the impact of a DELRIN<sup>TM</sup> bullet on one end of the bar. The dimensions of the bar, along with the material properties, were presented in Section 3.1.1. The finite element mesh used was schematically the same as the one presented in Figure 3.3.

A force gauge mounted at one free end is impacted by the DELRIN<sup>TM</sup> and records the impact force data. Two strain gauges measure the strain in the middle of the bar. Two gauges are used to compensate for any bending strains and to accurately indicate only longitudinal strains. Both force and strain gauge data are acquired and processed using a LABVIEW<sup>TM</sup> code developed by the author. The force data is used as input to the five-ADF axisymmetric finite element code. The first pulse through the middle of the bar is captured and analyzed. A Newmark integration scheme was used to find the wave propagation parameters. Figure 3.53. shows the compressive impact force of the DELRIN<sup>TM</sup> bullet. The rise time of the force is approximately 0.7 milliseconds.

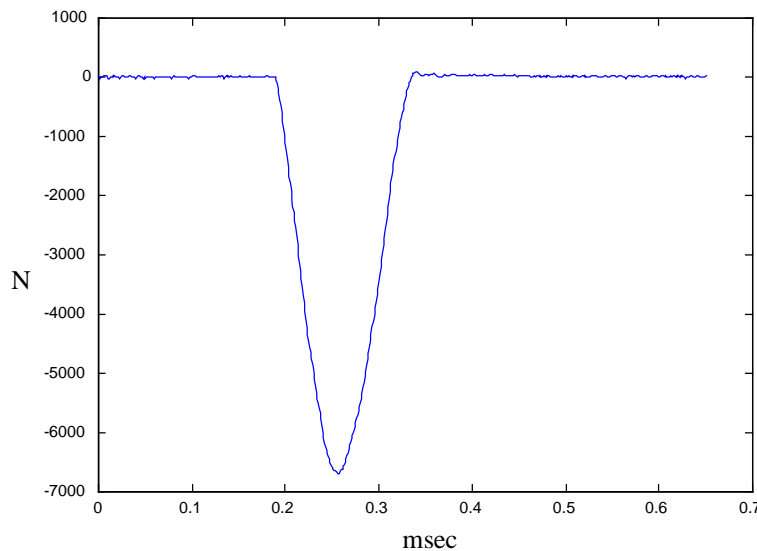


Figure 3.53. Impact force of DELRIN<sup>TM</sup> bullet at end of bar

Figure 3.54. shows the predicted and experimental displacement in the middle of the bar. The strain gauge signal is scaled by multiplying it with the propagation velocity ( $c=5080$  m/s for Ti6Al4V), which varies little with frequency for metals, thus finding the phase velocity of the pulse through the bar. The experimental displacement trace is obtained by integrating the particle velocity time record at that particular location.

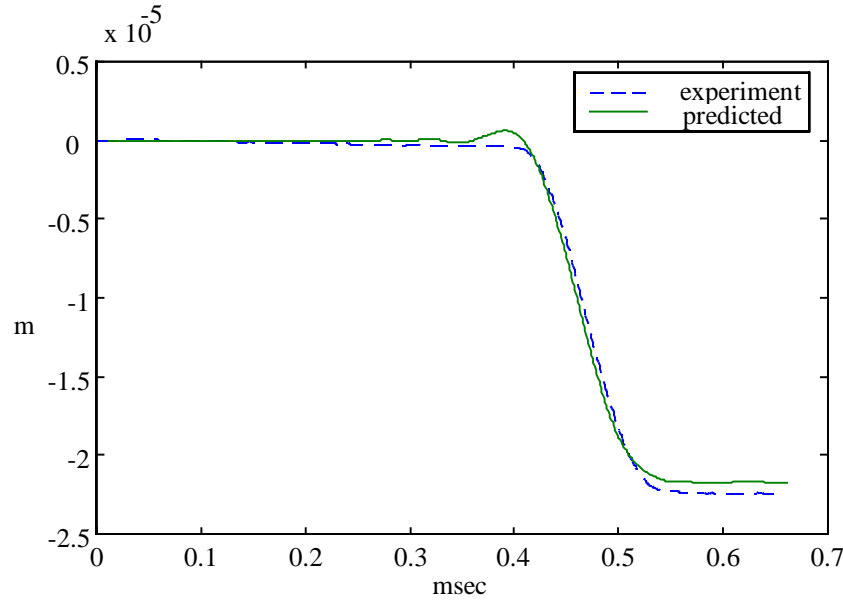


Figure 3.54 Predicted vs. experimental longitudinal displacement on the bar

The predicted displacement record agrees within 5% relative error with the experiment. The model correctly predicts the incremental displacement profile; the magnitude of the predicted displacement step is slightly lower than the measured value. The shape of the predicted trace shows high frequency components introduced by the relatively rough size of the finite element mesh (4 rows by 50 nodes each); a finer mesh would yield better results.

Figure 3.55. shows the predicted and experimental particle velocity in the middle of the bar. The velocity is predicted within 2% relative error by the ADF model. The shape of the predicted pulse is consistent with the experiment, and has approximately the same duration of 0.15 milliseconds, which means that the model accounts for any dispersion.

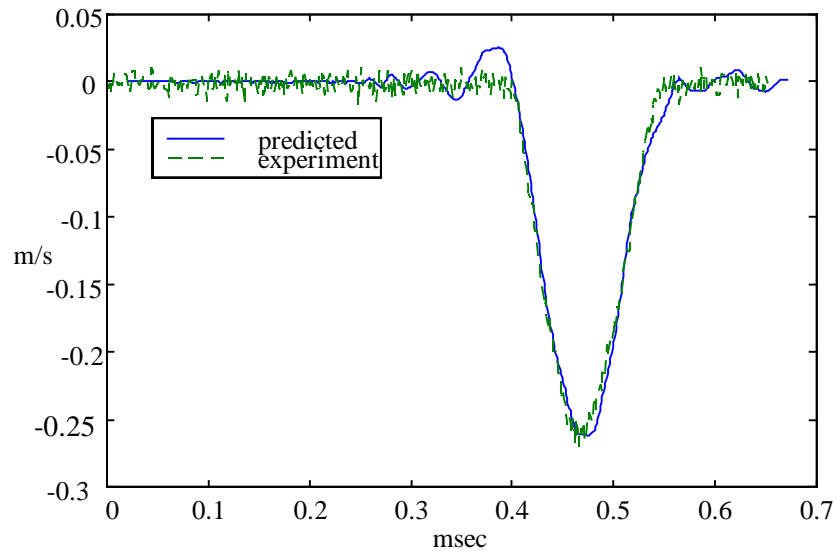


Figure 3.55. Predicted vs. experimental longitudinal velocity on bar

Figure 3.56. shows the predicted and experimental acceleration in the middle of the bar. Again, the magnitude and duration of the acceleration is predicted within 5% relative error by the ADF model. Note the high frequency content of the experimental acceleration trace (obtained by scaling and differentiating the strain gauge signal). Figure 3.57. shows the predicted and experimental power spectrum of the velocity in the middle of the bar, normalized to their respective DC components. The model accurately predicts the first resonance, which is slightly above 10 kHz.

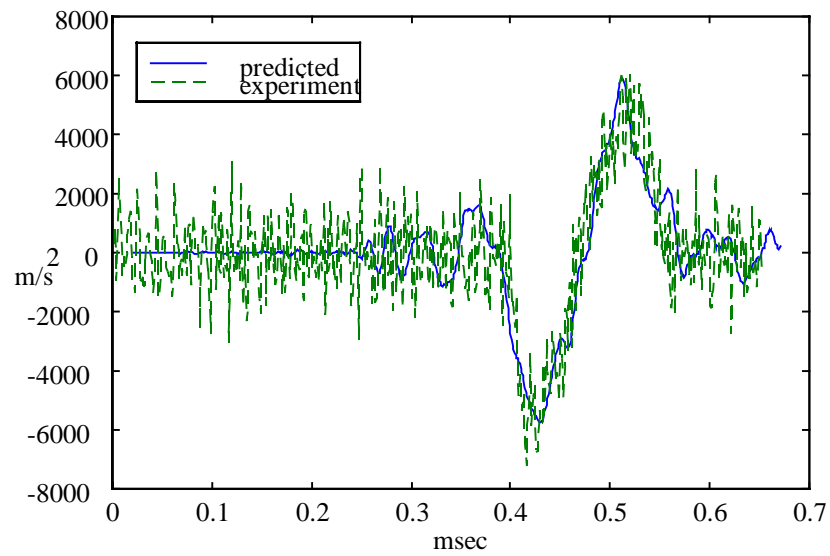


Figure 3.56. Predicted vs. experimental longitudinal acceleration on bar

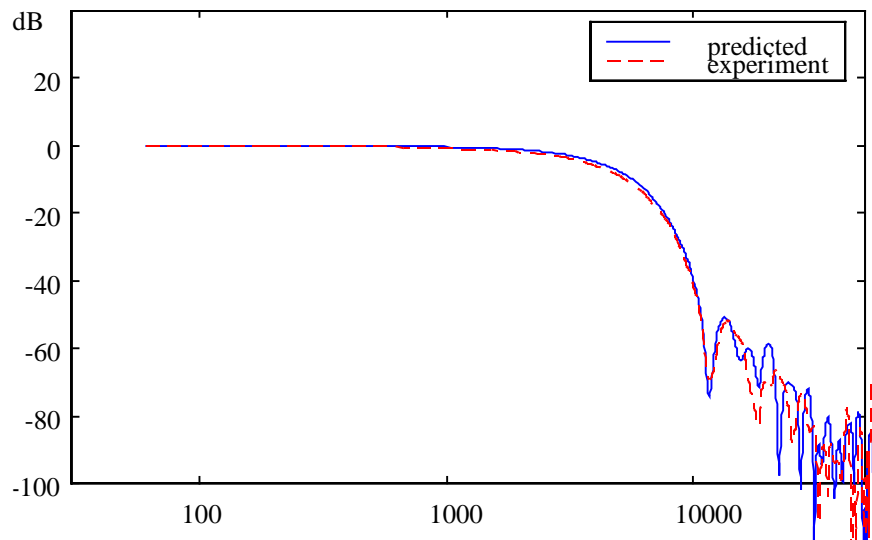


Figure 3.57. Predicted vs. experimental longitudinal velocity power spectrum on bar

### 3.3.3. Modeling of wave propagation through viscoelastic bars and comparison to experiments

ADF axisymmetric finite elements are employed to model damping in structures with material properties characterized by strongly frequency-dependent material properties. Examples of such structures include viscoelastic bars. The longitudinal wave propagation along a free-free PERSPEX<sup>TM</sup> bar is investigated. The longitudinal wave is created by the impact of a DELRIN<sup>TM</sup> bullet on one end of the bar. The bar is 1.73-m long and has a 1.6-cm diameter. The finite element mesh used is presented in Figure 3.3. A force gauge is mounted at the impacted end of the bar to monitor the impact force. Two strain gauges measure the strain in the middle of the bar. The force data is acquired and used as input to the one ADF axisymmetric finite element modeling code. A Newmark integration scheme ( $\alpha=1/4$   $\beta=1/2$ ) along with a 200-node grid (see Figure 3.3.) are used in the modeling. The grid size and time step chosen assure that frequency components of up to 15 kHz are accurately represented in the response. The ADF parameters used are given in Table 3.4. The comparison of predicted versus experimental strain at a longitudinal location 0.92 meters from the impacted end of the bar is shown in Figure 3.58. The model predicts the peak value of the first pulse to within 9% relative error to the experiment, while the second pulse is predicted within 4% relative error. The longitudinal phase velocity is predicted within 2% relative error. The frequency content of the predicted second pulse shows slightly less dispersion than in reality. That is because ADF material parameter approximation is valid over a limited frequency range. Figure 3.59. shows how the mechanical energy of the bar (the sum of the strain and kinetic energies) decays with time in an almost exponential manner, to a value equal to the constant-velocity kinetic energy. Figure 3.60. and 3.61. show the predicted displacement and velocity, respectively, at the longitudinal station mentioned above. Note that the displacement steps become more rounded as time progresses.

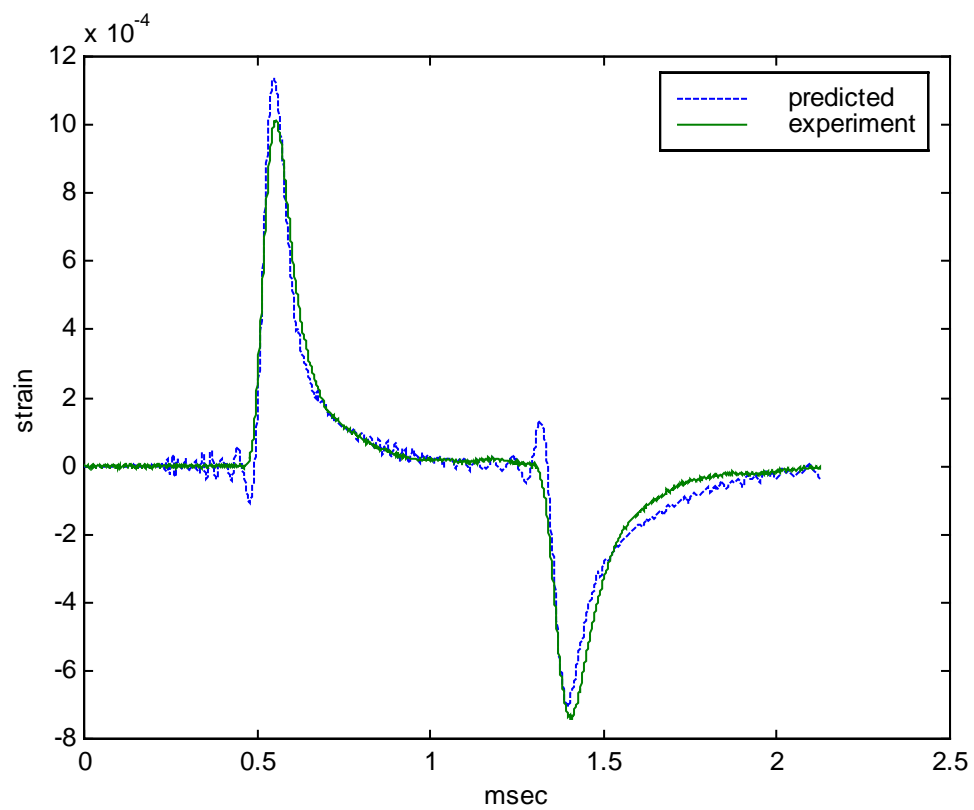


Figure 3.58. Predicted vs. experimental strain time record at middle of PERSPEX<sup>TM</sup> bar

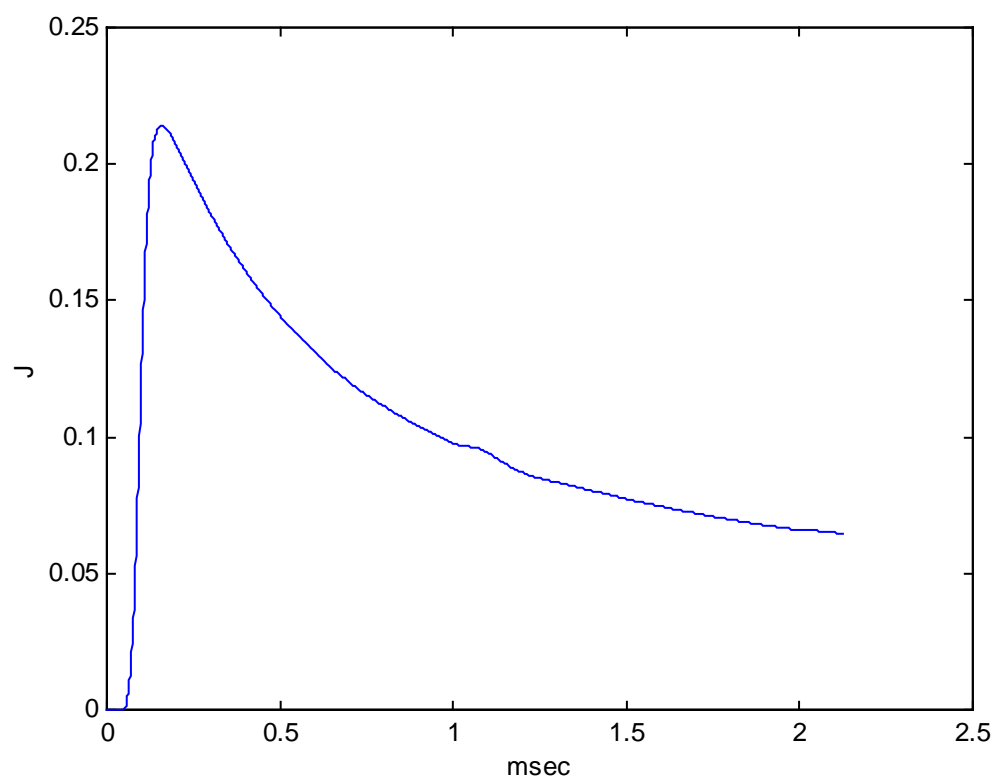


Figure 3.59. Mechanical energy in PERSPEX<sup>TM</sup> bar

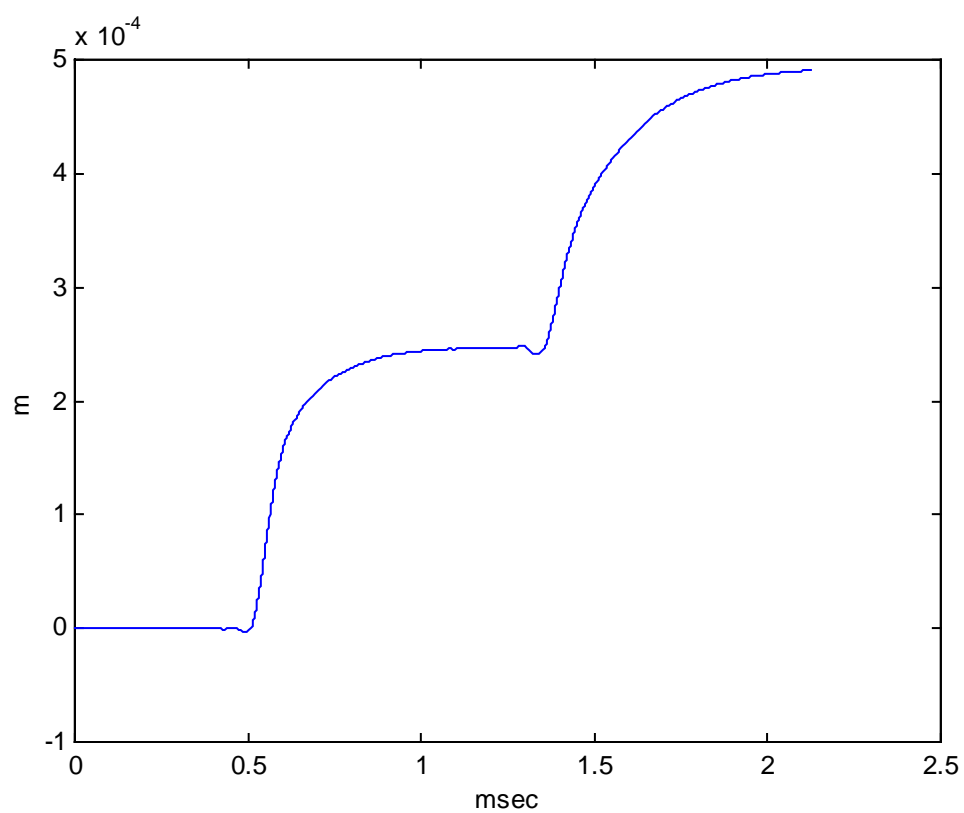


Figure 3.60. Predicted displacement time record at middle of PERSPEX<sup>TM</sup> bar



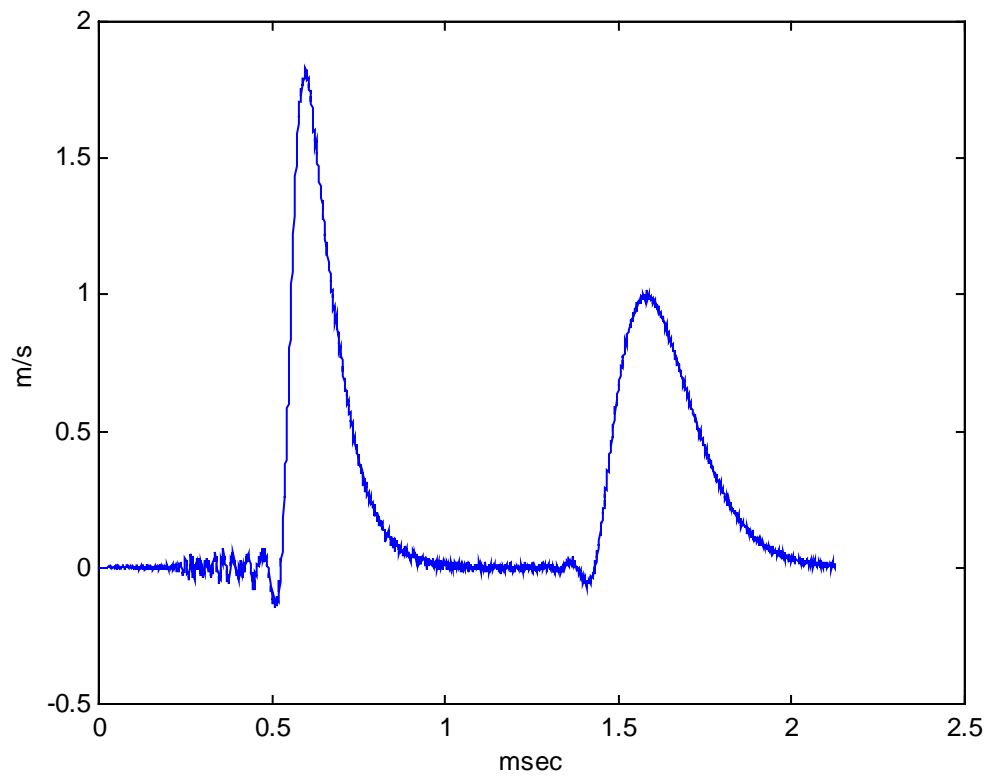


Figure 3.61. Time record of predicted particle velocity at strain gauge location, on PERSPEX<sup>TM</sup> bar

#### 3.3.4. Modeling of mechanical filters in shock conditions

Mechanical filters are often found as components in shock accelerometers, where they protect the sensing element from shock transients. It is of interest to quickly determine the frequency dependence of the filter material properties. One reason is that large parameter variations may exist between different batches of a given material; the second is that such material data may be unpublished or hard to find. The ADF method along with the Hopkinson bar technique may be used to find the frequency dependence of the viscoelastic materials' moduli.

To verify this approach, a mechanical filter made of nitrile rubber is glued at the end of a 2.03 m long Hopkinson bar. The filter is 3-mm thick and has a diameter of 1.9 cm, same as the bar. A 30-gram mass is glued on to the filter; the mass has a shock accelerometer screwed into it. The shock accelerometer (PCB 305A05) does not have itself a mechanical filter. A force gauge (PCB 218 C) is screwed into the opposite end of the bar. A DELRIN<sup>TM</sup> bullet driven by compressed air hits the force gauge. The impact force (shown in Figure 3.62) and acceleration are recorded using a 1 MHz sampling rate Gage<sup>TM</sup> data acquisition board. The force data is used as input into the finite element code; the acceleration record is integrated with respect to time and the resulting velocity record is compared to the prediction. Axisymmetric, single-ADF finite elements are used to model the bar and filter. The bar is represented with a 200-node grid, similar to the one shown in Figure 3.7. To allow proper representation of frequency components, a time integration step of 1 microsecond is chosen.

The ADF model parameters must be estimated next. The initial input relaxation strength and inverse of relaxation time are approximated from available experimental data [9], and from Equations (2.109-2.110). These values offer an initial guess of the ADF parameters that is in the neighborhood of the actual values. In Reference [9], the shear modulus is plotted versus frequency up to a temperature of 10<sup>0</sup>C. The actual experiment occurs at room temperature, 23<sup>0</sup>C. As a result, the peak loss-factor frequency, at room temperature, should be higher than the corresponding frequency at 10<sup>0</sup>C. The ADF

model predictions, such as mass velocity, are then iteratively fit to experimental data, and the corresponding ADF input parameters are presented in Table 3.8.

Table 3.8. ADF parameters used (1 ADF) for nitrile rubber

Parameter	Initial <sup>**</sup>	Final
Peak loss factor $\eta_P$	0.72	-
Frequency at peak loss factor (Hz)	2000	-
$\Omega$ (rad/s)	2.5e4	2.1e5
$\Delta_G^*$	2.8	6

\*  $\Delta_G = \Delta_K$ ; the relaxation strengths corresponding to the shear and bulk modulus, respectively, are equal

\*\* at 10<sup>0</sup>C

Figures 3.63. shows a comparison of the single-ADF curve-fit of the shear modulus and loss factor. The predicted longitudinal particle velocity and experimental velocity of the mass versus time are compared in Figure 3.64. The magnitude of the first velocity peak is predicted within 5% relative error to the experimental value. Figure 3.65. shows the predicted longitudinal displacement of the mass versus time. Note how the filter resonances are superimposed on the displacement steps. Figure 3.66. shows the mechanical energy in the bar versus time. The filter absorbs the energy as the pulse passes through it and causes the steps observed in the energy time record.

In conclusion, these experiments and simulations show that the ADF axisymmetric finite element model can approximate well damping behavior of viscoelastic materials. An approximation of material moduli frequency dependence of a viscoelastic structure may be achieved by iteratively matching ADF model predicted quantities (i.e., velocity) to corresponding experimental results, obtained with the Hopkinson bar method.

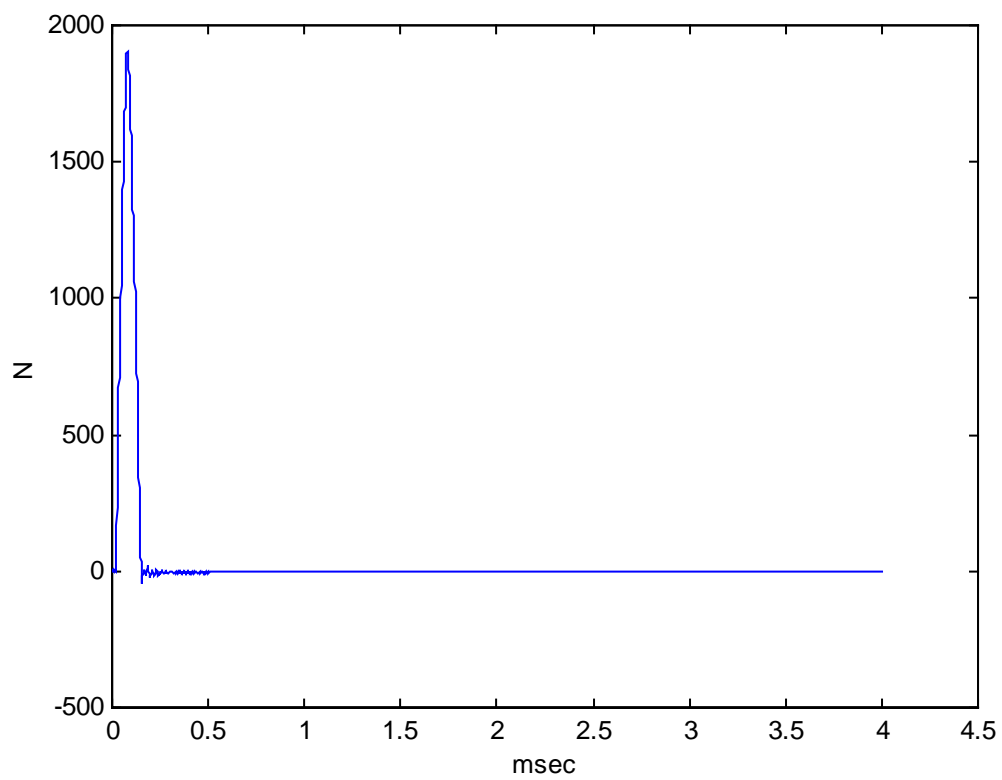


Figure 3.62. Impact force

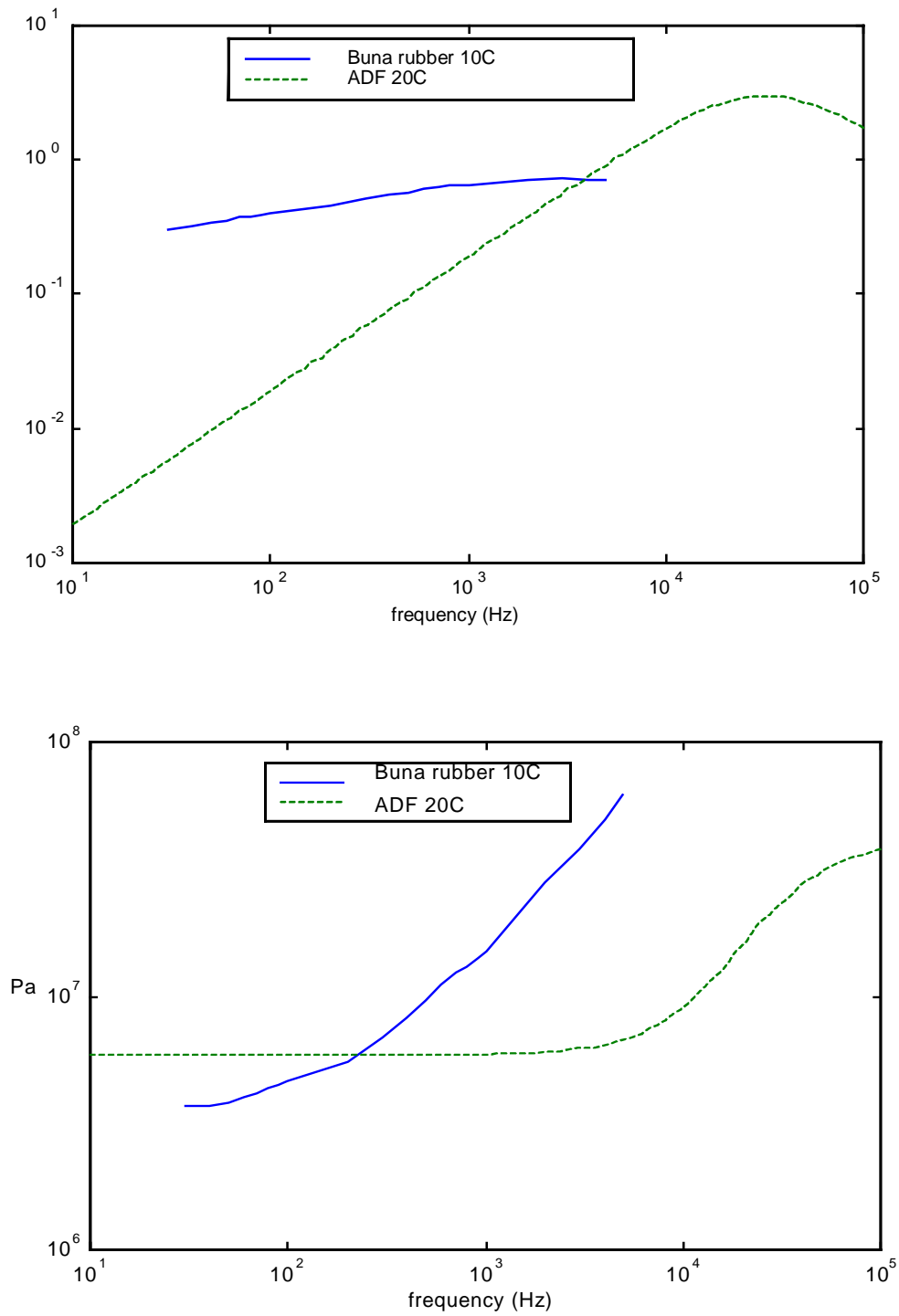


Figure 3.63. Comparison of single-ADF generated loss factor (a) and shear modulus (b), at  $20^0$  C, to corresponding experimental quantities at  $10^0$ C

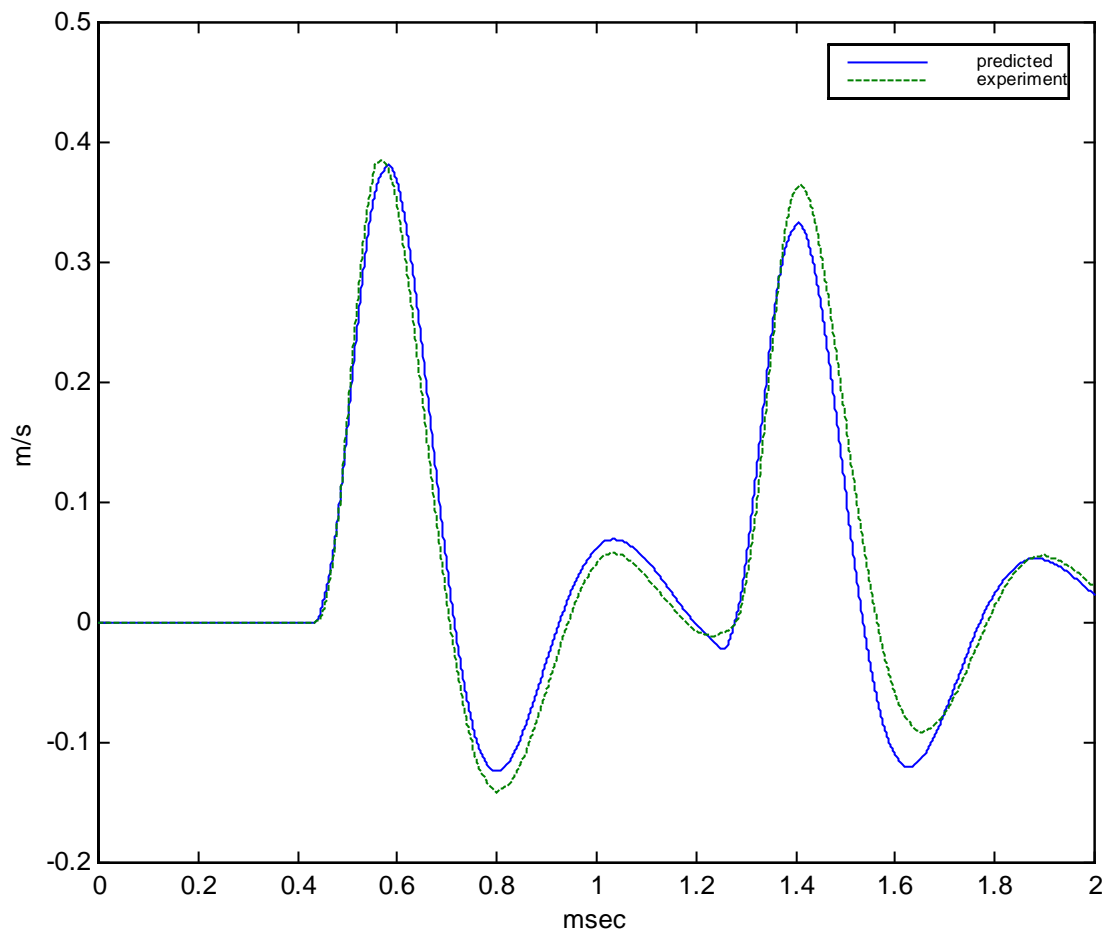


Figure 3.64. Particle velocity of mass

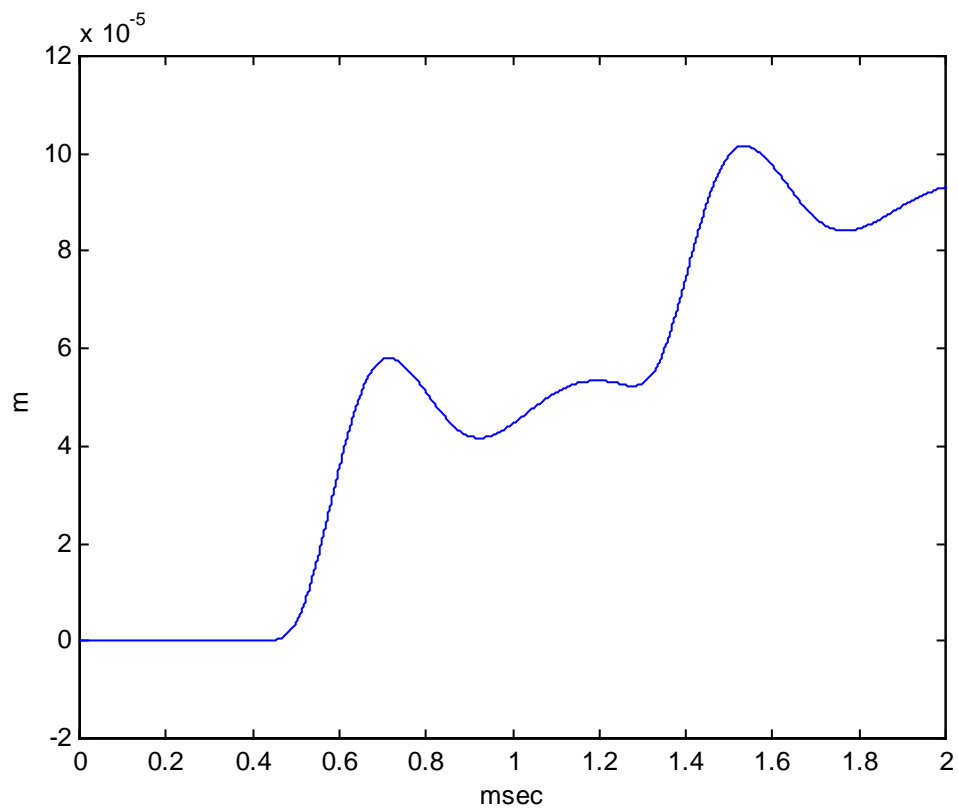


Figure 3.65. Longitudinal displacement of mass vs. time, 3-mm thick filter

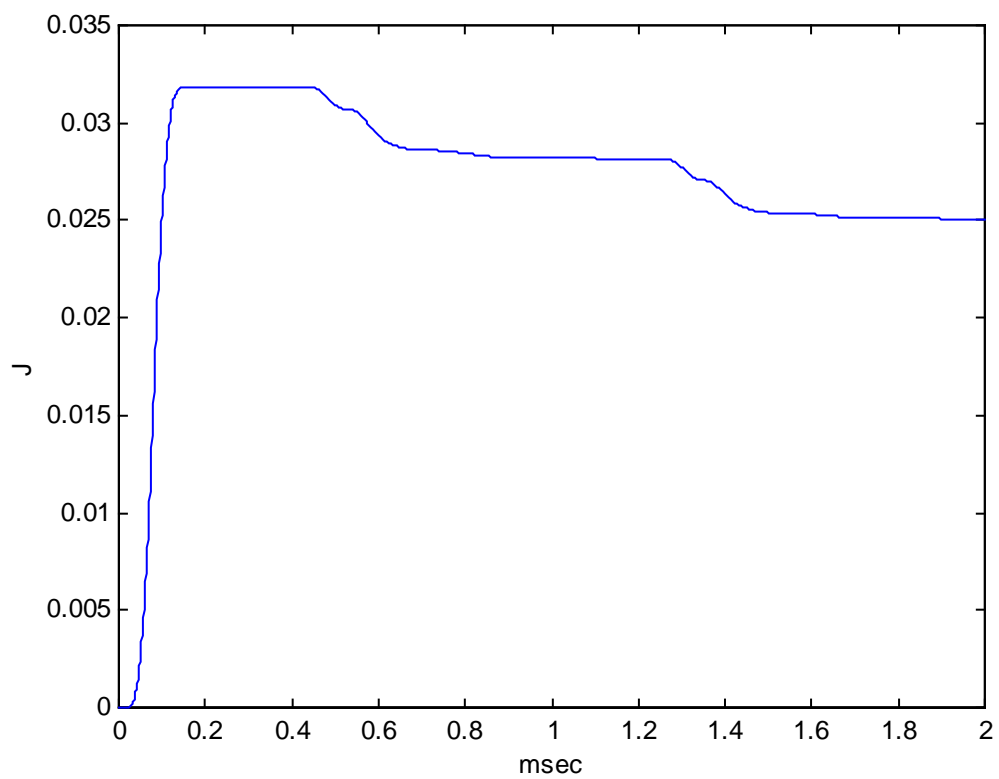


Figure 3.66. Mechanical energy in bar vs. time, 3-mm thick filter



## CHAPTER 4. CONCLUSIONS AND FUTURE WORK

### 4.1. Conclusions

The objectives of the current research, as stated in Section 1.7, have been achieved. These objectives were

- 5) to model mechanical filters subjected to shock loading;
- 6) to study longitudinal wave propagation through viscoelastic bars;
- 7) to develop single and multiple ADF axisymmetric and plane stress finite elements;  
and
- 8) to determine material moduli frequency dependence using Hopkinson bar experiments and ADF model curve-fitting

The following paragraphs provide a summary of the presented research.

1) Plane stress and axisymmetric single and multiple ADF axisymmetric and plane stress finite elements were developed to model three-dimensional and two-dimensional viscoelastic structures. These finite elements are based upon the Anelastic Displacement Fields (ADF) theory. Theoretical simulations and experimental data of longitudinal wave propagation through elastic and viscoelastic bars were used to check results predicted by models employing ADF plane stress and axisymmetric finite elements. Good correspondence between finite element and theoretical data was observed. An ADF axisymmetric model was also employed to study wave propagation along a split Hopkinson bar, made of titanium alloy and PERSPEX<sup>TM</sup>. Plane-stress, ADF finite elements allow the study of longitudinal wave propagation through viscoelastic rods of rectangular cross section.

2) Longitudinal wave propagation through bars, with strong- or weak-frequency dependent material properties, was studied with the newly developed finite elements. The ADF models demonstrated their capability to capture well both geometric dispersion (when compared to theory), and viscoelastic attenuation phenomena. The strain pulses travelling through a PERSPEX<sup>TM</sup> bar (high loss factor) and a titanium alloy bar (low loss factor) were well predicted by axisymmetric ADF models.

3) Mechanical filters are often used in engineering applications to alleviate or eliminate shock transients that may damage sensitive components. Experiments involving mechanical filters subjected to shock were conducted. In these experiments, axisymmetric filters made of a rubber disk and an identical diameter steel disk were dropped onto a force gauge. The recorded force served as input to the axisymmetric finite element model. Displacement, velocity and acceleration data compared reasonably well to ADF model predictions. ADF input parameters (inverse of relaxation time and relaxation strengths) were determined by curve fitting to experimental modulus data. These tests also provided a method of checking the validity of the input ADF parameters. Mechanical filters were then used to isolate a mass placed at one end of a Hopkinson bar from high g levels generated by a projectile impact at the other end. The velocity of the mass was well predicted with a mixed elastic/one-ADF finite element model (i.e., elastic finite elements for the bar and ADF finite elements for the mechanical filter). Model predictions compared well to acquired data. ADF 3D finite element models may thus be successfully employed to design mechanical filters for various shock-isolation applications. Another result is that the Hopkinson bar method may be used along with ADF finite element codes to determine material moduli frequency dependence. In this mixed experimental-analytical approach, predicted quantities, such as particle velocity, are curve-fitted to experimental values. The ADF parameters that lead to the best fit are then used to generate material moduli vs. frequency nomograms.

#### 4.2. Future work

Suggestions for future research include

1. The development of a more comprehensive database for viscoelastic materials. Current databases often lack data that relates material moduli to frequency; even manufacturer databases are not complete from this point of view. Few books offer such information and even they offer a listing of no more than thirty materials [9-10]. Such databases would considerably ease the design of structures incorporating damping materials, since the design engineer would not have to replicate expensive material characterization tests.
2. Development of 3D ADF finite elements which accurately model temperature, strain, and frequency dependence of material properties, and the development of 3D ADF nonlinear finite elements. The ADF finite elements presented in this work do not model large-displacement viscoelastic material behavior, nor do they incorporate thermal effects. A suggested reference is Govindswamy [36], who developed single degree-of-freedom, nonlinear, ADF finite elements, which incorporate both thermal, strain and frequency effects.
3. Development of other types of 3D ADF finite elements, such as bricks and tetrahedrons. Such elements could model frequency behavior in 3D structures loaded by arbitrary forces. Suggested references include Lesieutre and Bianchini [32-33], who developed linear ADF plate elements.
4. Reduction of variables in an ADF model. Analysis of shock behavior of viscoelastic structures requires proper modeling of material moduli frequency dependence over a broad frequency range, leading to an increased number of ADF degrees of freedom. This increases both memory and CPU requirements. As a result, degrees of freedom reduction methods are needed to keep solver matrices dimensions reasonable. Suggested bibliography includes Inman and Park [54], Yae and Inman [55], who concentrated on the reduction of degrees of freedom in the GHM model.

5. Incorporation of the new plane stress and axisymmetric ADF finite element in a commercial code. Finite element software packages, such as ANSYS<sup>TM</sup> or ABAQUS<sup>TM</sup> allow the user to design its own finite elements. It would obviously be advantageous to use powerful meshing subroutines.

## REFERENCES

- [1] Ferry, J.D., “Viscoelastic Properties of Polymers”, John Wiley & Sons, New York, 1980
- [2] Christensen, R.M., “Theory of Viscoelasticity, An Introduction”, Academic Press, New York, 1982
- [3] Shames, I.H. and Cozzarelli, F.A., “Elastic and Inelastic Stress Analysis”, Prentice Hall, Englewood Cliffs, New Jersey, 1992
- [4] Lockett, F.J., “Nonlinear Viscoelastic Solids”, Academic Press, New York, 1972
- [5] Vinogradov, G.V. and Malkin, A.Y., “Rheology of Polymers”, Springer-Verlag, New York, 1980
- [6] Bert, C.W., “Material Damping: An Introductory Review of Mathematical Models, Measures and Experimental Techniques”, Journal of Sound and Vibration, Vol. 29, No. 2, pp.129-153, 1973
- [7] Hall, C., “Polymer Materials”, John Wiley & Sons, New York, 1991
- [8] Jones, D.I.G., “A Reduced Temperature Nomogram for Characterization of Damping Material Behavior”, Shock and Vibration Bulletin 48, Part 2, pp. 13-22, 1978
- [9] Nashif, A., Jones, D., and Henderson, J., 1985. Vibration Damping, John Wiley & Sons, New York.
- [10] Read, B.E. and Dean, G.D., “Determination of Dynamic Properties of Polymers and Composites”, John Wiley & Sons, New York 1978
- [11] Inman, D.J., “Engineering Vibration”, Prentice Hall, Englewood Cliffs, New Jersey, 1994
- [12] Kohnke, P., “ANSYS User’s Manual for Revision 5.1- Volume IV , Theory”, Swanson Analysis Systems, 1994
- [13] Rogers, L.C. et al., “The Modal Strain Energy Finite Element Method and its Applications to Damped Laminated Beams”, Shock and Vibration Bulletin, Vol.51, 1981

- [14] Johnson, C.D. and Kienholz, D.A., "Finite Element Prediction of Damping in Structures with Constrained Viscoelastic Layers", *AIAA Journal*, Vol. 20, No.9, 1981
- [15] Segalman, D.J., "Calculation of Damping Matrices for Linearly Viscoelastic Structures", *Journal of Applied Mechanics*, Vol. 54, pp.585-588, September 1987
- [16] Bagley, R.L. and Torvik, P.J., "A theoretical Basis for the Application of Fractional Calculus to Viscoelasticity", *Journal of Rheology*, Vol. 27, No.3, pp.201-210,1983
- [17] Bagley, R. L. and Torvic, P.J., 1985, "Fractional Calculus in the Transient Analysis of Viscoelastically Damped Structures," *AIAA Journal*, Vol. 23, No 6, 918-925.
- [18] Padovan, J., "Computational Algorithms for FE Formulations Involving Fractional Operators", *Computational Mechanics*, Vol.2, pp.271-287, 1987
- [19] Grunwald, A.K., "Über Begrenzte Deviationene und Deren Anwendung", *Z. Agnew, Math Phys.*, Vol.12, 441, 1967.
- [20] Zienkiewicz, O.C., "The Finite Element Method", McGraw-Hill, New York 1977
- [21] Enelund, M. and Lesieutre, G.A., "Time Domain Modeling of Damping using Anelastic Displacement Fields and Fractional Calculus", *International Journal of Solids and Structures*, v.36, pg. 4447-4472, 1999
- [22] Chern, J., "Finite Element Modeling of Viscoelastic Materials on the Theory of Fractional Calculus", Ph.D. Thesis, The Pennsylvania State University, University Park, 1993
- [23] Golla D.F. and Hughes, P.C., "Dynamics of Viscoelastic Structures-A Time Domain Finite Element Formulation", *Journal of Applied Mechanics*, Vol. 52, pp.897-906, December 1985
- [24] McTavish, D. J., and Hughes, P. C., 1985. "Dynamics of Viscoelastic Structures - A Time-Domain, Finite Element Formulation," *Journal of Applied Mechanics*, 52, 897-906.
- [25] McTavish, D. J., and Hughes, P. C., 1993. "Modeling of Linear Viscoelastic Space Structures," *Journal of Vibration and Acoustics*, 115, 103-110.

- [26] Yiu, Y.C., "Finite Element Analysis of Structures with Classical Viscoelastic Materials", Proceedings of the 34<sup>th</sup> AIAA/ASME/ASCE/AHS/ASC Structures, Structural Dynamics and Materials Conference, La Jolla, CA, April 1993.
- [27] Yiu, Y.C., "Substructure and Finite Element Formulation for Linear Viscoelastic Materials", Proceedings of the 35<sup>th</sup> AIAA/ASME/ASCE/AHS/ASC Structures, Structural Dynamics and Materials Conference, Hilton Head, SC, April 1994.
- [28] Lesieutre, G. A., "Finite Element Modeling of Frequency-Dependent Material Damping using Augmenting Thermodynamic Fields", Ph.D. Dissertation, Aerospace Engineering, University of California, Los Angeles, CA, May 1989
- [29] Shames, I.H., Dym, C.L., "Energy and Finite Element Methods in Structural Mechanics", Hemisphere Publishing Corporation, 1985
- [30] Lesieutre, G.A. and Mingori, D.L., "Finite Element Modeling of Frequency Dependent Material Damping Using Augmenting Thermodynamic Fields", Journal of Guidance, Control and Dynamics, Vol. 13, No.6, pp. 1040-1050, November- December 1990
- [31] Lesieutre, G. A., "Finite Elements for Dynamic Modeling of Uniaxial Rods With Frequency Dependent Material Properties", International Journal of Solids and Structures, Vol. 29, pp. 1567-1579.
- [32] Bianchini, E. and Lesieutre, G.A., "ATF-based Viscoelastic Plate Finite Elements", Pennsylvania State University, Department of Aerospace Engineering Report No. CIRA 376, Vol.1, September 1992.
- [33] Bianchini, E. and Lesieutre, G.A., "ATF-based Viscoelastic Plate Finite Elements", Pennsylvania State University, Department of Aerospace Engineering Report No. CIRA 376, Vol.2, January 1993.
- [34] Lesieutre, G.A. and Bianchini, E., "Time Domain Modeling of Linear Viscoelasticity Using Anelastic Displacement Fields", *Journal of Vibration and Acoustics*, pg. 424-430, Vol. 117, October 1995
- [35] Lesieutre, G.A. and Bianchini, E., "Finite Element Modeling of One-Dimensional Viscoelastic Structures Using Anelastic Displacement Fields", Journal of Guidance, Control, and Dynamics, Vol. 19, No. 3, May-June 1996

- [36] Govindswamy, K., "Modeling of Strain-, Temperature-, and Frequency-Dependent Properties of Elastomeric Damper and Bearing Materials", Ph.D. Thesis, Department of Aerospace Engineering, The Pennsylvania State University, December 1995
- [37] Banks, H.T. and Lybeck, N., "Modeling Methodology for Elastomer Dynamics", Systems and Control in the Twenty-First Century, edited by Byrnes, C.I. et al., Birkhauser, 1997
- [38] Kolsky, H., "Stress Waves in Solids", Dover Publications, New York, 1963
- [39] Graff, K.F., "Wave Motion in Elastic Solids", Dover Publications, New York, 1975
- [40] Kolsky, H., "The Measurement of the Material Damping of High Polymers over Ten Decades of Frequency and its Interpretation", M<sup>3</sup>D: Mechanics and Mechanisms of Material Damping, ASTM STP 1169, V.K. Kinra and A. Wolfenden, Editors, American Society for Testing and Materials, Philadelphia, 1992, pp. 4-27
- [41] Kolsky, H., "The Propagation of Stress Pulses in Viscoelastic Rods", Philosophical Magazine 1956, Vol.1, pp.693-711
- [42] Brown, G., "Accelerometer Calibration with the Hopkinson Pressure Bar", Instrument Society of America, Reprint No. 49.3.63, 18<sup>th</sup> Annual ISA Conference and Exhibit, September 1963, Chicago, IL.
- [43] Bateman, V. et al, "Calibration of a Hopkinson Bar with a Transfer Standard", Shock and Vibration, Vol.1 No. 2, pp. 145-152, 1993
- [44] Dosch, J. and Jing, L., "Hopkinson Bar Acceptance Testing for Shock Accelerometers", Sound and Vibration, Instrumentation Reference Issue, February 1999
- [45] Oyadiji, S.O., Feroz, K.T., Tomlinson, G.R., "Design of Polymer-Based Mechanical Filters for Shock Measurement Accelerometers", SPIE Vol. 2720, pp.305-316
- [46] Tomlinson, G.R. et al., "Finite Element Modeling of Viscoelastic Elements Subjected to Large Static and Dynamic Deformations", Proceedings of the 69<sup>th</sup> Shock and Vibration Symposium, Albuquerque, NM 1998



- [47] Bateman, V. et al., "High Shock, High Frequency Characteristics of a Mechanical Isolator for a Piezoresistive Accelerometer", Proceedings of the 68<sup>th</sup> Shock and Vibration Symposium, , Albuquerque, New Mexico 1997
- [48] Chu, A.S., "Built-in Mechanical Filter in a Shock Accelerometer", Proceedings of the 59<sup>th</sup> Shock and Vibration Symposium, vol.1 pp. 251-269, Albuquerque, New Mexico, October 1988
- [49] Bathe, K.J., "Finite Element Procedures", Prentice Hall, Upper Saddle River, NJ 1996
- [50] Hughes, T.J.R., "The Finite Element Method", Prentice Hall, Englewood Cliffs, New Jersey 1987
- [51] Rao, S.S., "Mechanical Vibrations", Second Edition, Addison-Wesley Publishing Company, New York 1990
- [52] Soovere, J. and Drake, M.L., "Aerospace Structures Technology Damping Design Guide, Vol. III – Damping Material Data", AFWAL-TR-84-3089
- [53] Harris, C.M. Editor, "Shock and Vibration Handbook", Fourth Edition, McGraw-Hill 1995
- [54] Inman, D. J. and Park, C. H., "Damping: An Introduction to Viscoelastic Models", Proceedings from NATO Advanced Study Institute: Modal Testing and Analysis, May, 1998, pp. 459-473
- [55] Yae, K.H. and Inman, D.J., "Model Reduction in a Subset of the Original States", Journal of Sound and Vibration, v155(1), 1992, pp.165-176

## VITA

Razvan Rusovici

Razvan Rusovici was born on January 12, 1968, in Bucharest, Romania. He obtained his five-year Master of Engineering degree, Aircraft Structures Design specialty, from the Department of Aerospace Engineering, Polytechnical Institute of Bucharest, Romania, in July 1992. In December 1995 he graduated with a Master of Science degree in Aerospace Engineering from the Pennsylvania State University. He finally obtained his Doctoral degree in Mechanical Engineering from the Virginia Polytechnic Institute and State University in December 1999. He has a few publications, in the *Journal of Intelligent Material and Structures* and other conference proceedings. He loves flying and skiing, the sea and the mountains. He currently works as a Research Scientist for PCB Piezotronics Inc. in Depew, New York.